Further developments of optical fibre techniques for astronomical spectroscopy

Carrasco, Bertha Esperanza

FURTHER DEVELOPMENTS OF OPTICAL FIBRE TECHNIQUES FOR ASTRONOMICAL SPECTROSCOPY

by

Bertha Esperanza Carrasco, B.Sc., M.Sc.

October 1992

An account of work done at the Department of Physics, submitted to the University of Durham in accordance with the regulations for admission to the degree of Doctor of Philosophy.

ABSTRACT

This thesis describes instrumental techniques pursued to optimise the quality of the spectroscopic data which will be obtained via the new generation of multifibre systems. The technical aspects discussed include the instrumental sources of systematic errors on sky subtraction and new methods to evaluate the fibre performance in terms of throughput and preservation of the input focal ratio.

The limiting factor in faint multifibre spectroscopy is the accuracy and reliability of sky subtraction. Instrumentally the precision to which sky subtraction can be done is limited by systematic errors. The conditions that have to be satisfied to subtract the sky properly at faint levels, the sources of errors and possible ways of eliminating them are analysed. A comprehensive discussion of the effect of deficient wavelength sampling and of poor fibre flatfield calibration on sky subtraction is provided via computer simulations of fibre data.

Several laboratory fibre evaluation techniques and data processing software packages have been developed. These techniques have been used to measure the throughput of silica fibres at optical wavelengths. Also presented in this thesis are preliminary results obtained from a series of experiments implemented at infrared wavelengths.

As a result of these developments a new method for determining the focal ratio degradation (FRD), based on a known theoretical model for microbending induced beam-spreading is proposed. This theory characterises the FRD by a single parameter which can be determined by a very simple experiment. The model successfully predicts real experimental results. This new technique will allows us to accurately model the complete performance of any fibre. Such modelling can include complicated phenomena such as tilted input beams and central obstructions without the need to setup experiments for specific cases. Furthermore, it can be used to evaluate the performance of infrared fibres.

Finally, the results of an exhaustive laboratory evaluation of the Autofib-1.5 fibre bundle are presented. The evaluation was carried out after a multiway fibre connector prototype was incorporated into the Autofib-1.5 fibre bundle, with the emphasis being placed on the performance of the connector.

PREFACE

The work presented in this thesis was carried out between 1989 and 1992 while the author was a research student under the supervision of Dr. I.R. Parry and Dr. J.M. Breare in the Physics Department at the University of Durham. This work has not been submitted for any degree, diploma or other qualification at any other University.

Some of the work was carried out in collaboration with Dr. I.R. Parry. The major part of the research presented is, however, the author's own work. Certain results have appeared in the following papers:

Parry, I.R. & Carrasco, B.E., 1990. *Proc. SPIE*, **1235**, 702.

Carrasco, B.E. & Parry, I.R., 1992. in *Fibre Optics in Astronomy II*, Ed. Gray, P.M. *in press*.

For Alberto and Rafael

LIST OF CONTENTS

1 INTRODUCTION

Spectroscopy has developed as the leading technique by which astronomers measure the dynamics and chemical composition of stars, galaxies and other astronomical objects. Being basically an observational rather than an experimental science, astronomy is forced to rely very heavily on statistics drawn from measurements of many objects. For this reason in many programs it may be necessary to record the spectra of hundreds or thousands of objects before a pattern is clear. The possibility of recording spectra from several objects at once is therefore very attractive to the astronomer who is trying to gather data using limited telescope time. With today's 4m class telescopes, fibre optics allow us to collect light from many objects, anywhere in the telescope focal plane, without requiring an equivalent field for the spectrograph. As a consequence, fibres are also capable of being used at high dispersion. The flexibility of fibres combined with efficient light transmission has allowed the construction of very powerful instruments for simultaneous spectroscopy of many objects. The main limitations on the total number of simultaneous spectra are the size of the detectors and the field of the telescope.

This thesis is concerned with instrumental techniques that are aimed at optimising the quality of the spectroscopic data which will be obtained with the next generation of large multiplex gain multifibre systems.

1.1 Astronomical Applications

Multifibre spectroscopy systems are now fairly common on 1–4m telescopes and have transformed a number of branches of astronomy where statistical information of many sources is required. For the studies of faint objects the multiplex advantage encourages long observations that would be deemed uneconomic or too risky for a single object. Carter (1988) summarises the projects that have been done with fibre systems which would not have been possible otherwise. Amongst them are the following: studies of galactic dynamics based on large samples of stellar radial velocities; studies of stellar content and dynamics of galactic globular clusters; analysis of the internal kinematics, age and chemical composition of galaxies in nearby clusters; and detailed studies of the dynamics of rich clusters of galaxies, permitting analysis of the mass distribution and searches for dark matter. Surveys of galaxy and quasar redshifts for cosmological purposes have also been undertaken.

In fact, more than 50% of the spectroscopic time on the AAT is now multiobject in nature. In Table 1.1 some astronomical examples where fibre spectroscopy has been specially successful are highlighted.

On the other hand, there are many other projects where the surface density of candidates is sufficiently low as to demand several square degrees before a sufficient multiplex advantage can be achieved. The requirement for larger fields than are available at present —typically $\sim$ 40 arcmin diameter, has come from workers in both observational cosmology and in galactic structure studies who need greatly improved statistics to further their goals (see *RAS report on The Scientific Priorities for UK Astronomical Research for the Period* 1990–2000, April 1986). The need for an increased field size and a corresponding larger multiplex gain is scientifically driven by the large angular scales required to probe QSOs

Table 1.1 Titles of UK Observing Programmes Using Fibres on the AAT (1990–92)

The distribution of galaxies at the south galactic pole
The first near-infrared selected galaxy redshift survey
The first determination of the cluster correlation function from an objective sample
The evolution and distribution of galaxies to moderate redshifts
Optical spectroscopy and imaging in deep ROSAT survey fields
Evolution of the galaxy correlation function
Globular clusters as dynamical probes of the dark matter distribution in M104
The rotation velocities of blue horizontal branch stars in globular clusters
Evolution of the optical galaxy luminosity function
Abundance gradients in barred spiral galaxies
The origin of globular clusters
High resolution spectroscopy of stars in the galactic bulge
Kinematics of the outer parts of the small Magellanic Clouds
The F_e/H abundance distribution function in ω Centauri

Note: These titles were obtained from SERC PATT Newsletters and do not include a similar number of Australian fibre programmes.

and galaxy clustering at various epochs and for complete studies of the kinematics and chemical abundance of the stellar population in our own Galaxy.

The availability of a wide field (> 2 deg diameter) will fundamentally change the way in which a 4m class telescope operates. Many of the wide field fibre facilities will operate at prime focus where the field of view is most appropriate for surveys. This new generation of survey spectroscopy facilities will increase by at least an order of magnitude the ability to do optical survey spectroscopy over wide areas of sky with many hundreds of fibres at any one time.

The scientific impact of survey astronomy has been on problems such as the formation of large scale structure, cluster dynamics and the kinematics of the Galaxy. Studies of large-scale structure are fundamental to our understanding of the Universe because large structures observed today are cosmic fossils of conditions that existed in the early Universe. These fossils record the history of the formation and evolution of galaxies and structure. Some of the many scientific applications of multifibre spectroscopy are discussed below.

1.1.1 Galaxies and Cosmology

The classic method of investigating structure in the Universe is to observe the spatial distribution of galaxies. Extensive surveys of thousands of galaxy redshifts are needed in order to cover large enough volumes and scales. Astronomers would like to map a region large enough that it will qualify as a fair sample of the Universe, and to track the approach to uniformity as larger and larger regions are examined. For example, the CfA catalog surveys includes only one or two supercluster structures. Improved surveys of present day structure will require a large number of redshifts (50000-100000) over a relatively large area of the sky (*e.g.* White 1987).

Redshift surveys provide large samples of galaxies with (approximately) known distances and well defined selection effects. These can be used to help define the properties of the galaxy population. For example, luminosity functions as a function of colour and morphological type, fraction of galaxies with emission lines or active nuclei and the fraction of interacting galaxies, can all be studied. If the survey is carried out to a faint enough limiting magnitude it can also be used to study the evolution of these properties (see *e.g* White 1987).

Rich clusters of galaxies play a key role in determinations of the mean density of the universe because they sample the distribution of luminous mass and dark matter over a range of scales. Previous work on the internal dynamics of clusters has often been characterised by inadequate sampling or poor statistics. To place it on a sound statistical basis will require extensive redshift sampling programs (*e.g.* Taylor 1989).

1.1.2 QSO studies

There will be several programs on QSO research in the years to come. Taylor (1989) has summarised the major projects in this area which include the following: the luminosity function of high redshifts QSOs, the luminosity function of low luminosity QSOs, the clustering of QSOs and QSO absorption clouds.

An accurate determination of the QSO luminosity function at high redshifts ($z > 2$) is highly desirable to increase our understanding of the physical evolution of QSOs. Also, it will enable us to study the epoch of QSO formation and by association the epoch of galaxy formation.

The understanding of the physical evolution of QSOs will improve if the luminosity function of very faint ($21 < B < 23$) QSOs can be constructed in detail. In this magnitude

range the surface density of QSOs is expected to be $\sim$ 100 deg^{-2}. At such faintness high quality sky subtraction is a strict requirement.

The development of multiobject spectroscopy has allowed the study of QSO clustering to be performed in detail. However these surveys provide relatively little information on the evolution with redshift of QSO clustering. To do this spectroscopy of about 5000 QSOs might be required.

The study of relatively bright, high redshift QSOs at high dispersion has revealed the existence of many intervening absorption clouds, whose redshifts are intermediate between the QSO and the observer. The study of their spatial and spectral distribution represent another valuable probe of the structure of the distant universe. The surface density of QSOs with $B < 18.5$, bright enough to allow such high dispersion studies, permits several tens of objects per 2 deg field.

1.1.3 Galactic Structure

For studies of galactic structure, detailed abundance and velocity distributions in the Galactic spheroid and outer parts of the Galaxy are required because they provide a fossil record of the formation of our Galaxy. The rate of star formation in the protogalaxy can be calibrated and therefore such data provide an insight into how our spiral galaxy formed. In addition, kinematic information provides a test for the origin of angular momentum in our Galaxy as well as mass estimates for the Galaxy.

In summary, the survey facilities will push forward the frontiers of observational cosmology allowing us to accurately explore the large scale structures in the Universe, as traced through the QSO and galaxy distributions and to enable us to understand how

these structures evolve with time. In addition, much more work on the structure and kinematics of our own galaxy will be tackled.

1.2 Positioning systems

The first generation of fibre-optics couplers used manual plug-plate systems to locate the fibre entrance apertures in the telescope focal plane. Examples of such systems are MEDUSA at the Steward Observatory 2.3m telescope (Hill *et al.* 1980), FOCAP at the Anglo-Australian Observatory 3.8m telescope (AAT) (Gray 1983), the ESO 3.6m OPTOPUS system (Lund & Enard 1984) and NESSIE built for the Kitt Peak 4m telescope (Barden & Massey 1988). A different type of system (FLAIR) has been built for the 1.2m UK Schmidt Telescope (Watson 1986, 1988, Watson *et al.* 1990). FLAIR uses fibres glued directly to a glass positive copy of the target field.

In the manual method, an aperture plate is prepared from the astronomer's target list using a milling machine. Fibres are inserted in the plate by hand and a record must be kept of the fibre-hole configuration. The plate is mounted in a holder and fixed to the telescope before observations start. Such a system is cheap to start off and easy to construct but has several disadvantages. The astronomer has to specify well in advance the targets to be studied. If the observational conditions are unsuitable for the main programme, backup aperture plates are needed which are costly and yet might not be used. In general the labour-intensive nature of plug plate systems makes the regular use of large (> 100) numbers of fibres impractical. Handling of the fibres can produce considerable damage to their ends. The slow changeover time of about 15–20 minutes to change plates between exposures makes aperture plates best suited to programmes requiring long integration times. Maintaining the observing records requires considerable

effort and patience. The high demand for multifibre spectroscopy makes the system very expensive to operate since every hole that is drilled and every fibre that is plugged costs time and money. Nevertheless, in spite of their limitations these systems have been used to successfully carry out many important astronomical programmes.

A natural step forward from the aperture plate approach is to build a robotic system to position the fibres remotely under computer control. Automating the positioning of fibres removes many of the disadvantages of manual couplers. The main aim is to achieve a very high multiplex gain of at least 100 fibres. Remote positioning allows the computer to handle all of the fibres without physically removing the fibre bundle from the instrument thus avoiding the complication of moving the fibres from one aperture plate to the next. Less frequent man-handling increases the stability of the fibre ends and fibre positioners can achieve faster pattern changeover between integrations. In addition, the control computer keeps an accurate log of the observations and more consistent and accurate positioning is achieved, possibly leading to better sky subtraction (see Ellis & Parry 1988).

Currently, there are two basic types of positioners in operation at various observatories. The MX type (Hill 1986, Hill & Lesser 1988) uses independent robots to position fibres across the field of view. The MX system, developed at the Steward Observatory, provides the most active capability, since each fibre has its own precision actuator and therefore it has a very rapid configuration time of a few seconds. However it is extremely costly and cannot easily be extended to a large number of fibres due to space constraints around the edge which put an upper limit to the total number of fibres, typically less than 50.

A radically different approach is the Autofib type, in which individual fibre-probes are handled by a single high speed precision robot (Parry 1986, Parry & Gray 1986,

Parry & Sharples 1988). Autofib-1, developed for the Cassegrain focus of the AAT, has 64 independent fibres to position across a 40 arcmin field. Such a system has a slower field configuration time than an MX-type instrument, being typically of a few minutes. However, this approach can potentially handle large number of fibres since the fibres themselves can be made very small and compact and the cost of robotic components is not directly proportional to the number of fibres. The Autofib concept is very popular and many observatories have developed similar instruments, such as the HYDRA system constructed at Kitt Peak National Observatory (Barden *et al.* 1992a).

The success of these systems and the increase in the demand for statistical information of hundreds and sometimes thousands of objects has led to further developments in the technology of multifibre spectroscopy. The next generation of multifibre systems, now under construction, will have hundreds of fibres. An example of such a system is Autofib-2. This instrument is the common user fibre positioning system for the William Herschel Telescope (WHT) which will operate at the prime focus to exploit the WHT's largest field of view. The system will offer a choice between two feeds of 150 fibres, each having a different fibre diameter. The full prime-focus 1 deg field will be accessible and the fibres will feed the WYFFOS spectrograph which is being purpose built for use with Autofib-2.

Another example is the AAO's 2 deg field (2dF) project which is the most ambitious multifibre spectroscopic facility being planned, for a 4m telescope, both in terms of the field area (3.14 deg^2) and the number of fibres (400). A complete telescope top-end dedicated to fibre spectroscopy will be built, incorporating a new prime focus corrector, a robotic positioner of the Autofib type, a double fibre-feed for rapid field changeovers and optimised fibre spectrographs.

The spectrograph survey telescope (SST) will be the first telescope specifically built for fibre spectroscopy. The 2.5m telescope being built at Apache Point, New Mexico, will have a wide, well corrected field (3 deg), equipped with a large focal plane CCD array for photometry and with a pair of fibre fed spectrographs will allow the measurement of 660 spectra per field. The baseline approach adopted for this project is a system of interchangeable plug-plate modules plugged off the telescope to save operating time (see *A Digital Sky Survey of the Northern Galactic Cap*, 1992). However, it is possible that a robotic system will be chosen rather than a plug-plate approach (see *Sky & Telescope*, October 1992) given all the drawbacks of the plug-plate systems discussed above.

In addition to the new systems described above, multifibre spectroscopy techniques will be transferred to the 8m class telescopes. For example the design of the Gemini project is driven to a great extent by the desire to provide a large field ($\sim$ 45 arcmin) for fibre work. Indeed, the multiplex gain will be dramatically improved considering that the field of an 8m can be physically very large. For instance, the 45 arcmin Gemini field will be more than twice as big in diameter as the AAT's 40 arcmin Cassegrain field. If the fibre probes are similar in size to existing 4m designs it will be possible to utilize far more fibres than ever before (*e.g.* Parry 1992).

1.3 Sky subtraction

For all the projects mentioned above sky subtraction is crucial. The standard method for sky subtraction with fibres is to dedicate about 5-10 fibres to blank sky for generating a simultaneous sky spectrum and to periodically offset the telescope to monitor changes in the fibre to fibre response. Successful sky subtraction requires the accurate estimation of the background sky spectrum associated with each object spectrum. Nevertheless it is

very difficult to make this estimation with sufficient accuracy because of several systematic effects. These include the different responses of sky fibres and the object fibre (which often has a wavelength dependence), the different sampling of the derived sky spectrum and the object+sky spectrum, scattered light and detector response. Also the sky background itself can vary from one fibre to the next and with time.

Experience at the AAT has shown that the systematic errors associated with fibre observations make sky-subtraction impossible at the faintest level which can be achieved with multislit spectroscopy. With the Low Dispersion Survey Spectrograph (LDSS) observations of objects to a magnitude limit of B=23 have been achieved. In comparison FOCAP or Autofib only permits the observations of objects to a limit of B=21.5 (Taylor 1988).

An alternative technique for correcting the variation in fibre throughput is beam-switching between pairs of adjacent fibres. The temporal variability of the sky is monitored by dedicating a few fibres to observe only the sky during both beam positions. This technique has the disadvantage of reducing the multiplex gain by a factor of two but it has given good results during tests at Kitt Peak Observatory. Barden *et al.* (1992b) present a fibre spectrum of a galaxy with $R = 20.6$ and $B = 23.1$.

Traditionally this sky subtraction problem has been the objection to fibres for very faint work (Parry & Carrasco 1990, Wyse & Gilmore 1992). There is, however, a clear requirement for faint object spectroscopy in statistical programs that require a large field and/or medium to high spectral resolution, since this cannot be done with multislit spectrographs. Very faint work is the major reason why the 8m telescopes are being built, therefore improved sky subtraction techniques will be vital for this next generation of telescopes. For applications of infrared fibres where the sky background is much higher the sky subtraction problem will also be of critical importance.

The development of multifibre systems has mainly concentrated on the technology of fibre positioners and to a much lesser extent on the basic optical properties of fibre couplers and the specialised analysis techniques which directly affect the quality of spectroscopic data obtained with fibre systems. There is no fundamental reason why shot-noise limited sky subtraction cannot be achieved and fibres should not be able to go as deep as slits once all systematic errors have been calibrated out. Fibres will always have a slightly lower throughput than slits, however, their large multiplex gain and their ability to provide large fields and high spectral resolution make it worth the effort to develop techniques that allow us to achieve accurate sky subtraction.

1.4 The opto-mechanical properties of fibres

The quantity of spectroscopic data depends on the choice of positioner system used but the quality of each individual spectrum depends on the properties of the fibre themselves which in turn strongly influence the design of the spectrograph. The transmission of the fibres, in particular in the ultraviolet, determines the length of the fibre feed and therefore the location of the spectrographs. Another important parameter is the fact that all fibres tend to change the incident f-ratio to a smaller number. This property is called focal ratio degradation (FRD). The diameter and FRD performance of the fibre is fundamental to design strategy for fibre spectrographs.

The degradation of the focal ratio can be a result of various processes including microbends in the fibre, stresses on the ends of the fibre and facial imperfections. FRD has a more pronounced overall effect on slow f-ratios than for fast f-ratios. Several new generation instruments such as Autofib-2, the 2dF and AMOS (Brodie *et al.* 1990) have been designed for use at the prime focus where the input f-ratios are fast enough to

minimise the focal degradation. Although the main reason for working at prime is to use the largest field of view the fast f-ratio is another important consideration.

Considerable effort has been directed to optimise the performance of spectrographs for multifibre work to operate in combination with the new generation of positioning systems. These spectrographs will have fast collimators or microlenses to account for focal ratio degradation and wide fields to image hundreds of spectra onto the detector. To provide data of the highest possible quality it is essential that the fibres meet the specifications of such spectrographs.

A major problem with fibres has been that FRD measurements reported by various workers depend on the experimental techniques used for the measurements themselves and sometimes, for the same type of fibre, the results vary significantly. This inconsistency is due in part to the absence of a standard evaluation method. Indeed, the results depend on many parameters involved in the complex evaluation techniques. Moreover, the preparation of the fibre bundle and in particular the fibre ends depend on several parameters.

The importance of the fibre evaluation methods should not be underestimated. A reliable and efficient evaluation method is vital in order to understand and eliminate the mechanisms that degrade the fibres. For an instrument with a single fibre we can justify spending a day to prepare each end of the fibre. However, this level of effort is not practical for an instrument with hundreds of fibres, so efficient polishing and testing methods are required. When choosing the optimal fibre, one has to consider properties such as core diameter, core/cladding ratio, buffer material, doping type and polishing techniques amongst others. Determining the effects of these characteristics on the quality of spectroscopic data requires detailed laboratory testing of FRD properties, attenuation and mechanical robustness.

Evaluation techniques are also fundamental to study different properties of fibres relevant to the design of new instruments. For example, if the optical axis of the fibre is misaligned to that of the incident beam, the f-ratio of the output beam is decreased. This broadening of the output beam adds to the FRD effect within the fibre to produce a decrease in system efficiency. The extent of such losses are very important for wide field system where the angle the principal ray makes with the focal plane can be large ($2° - 4°$) at the field edge.

Furthermore, these techniques are also crucial for infrared applications. The possibility of extending multifibre techniques to the infrared is now being investigated. At these wavelengths the requirement of reliable techniques is even more severe. This is a completely new area that promises the same sort of advances as seen in the optical region during the last few years.

1.5 Contents of Thesis

Research on many areas of the applications of fibre technology to astronomy is still required. In this thesis further developments of optical fibre techniques are presented. The main instrumental problems associated with sky subtraction, in particular those related to fibre performance are analysed. The properties of fibres related to astronomical applications are reviewed and a new technique for fibre evaluation is presented. Fibre testing methods used to evaluate a multifibre system are described. Preliminary results from measurements in the IR for a silica fibre are also presented.

The consequences of deficient wavelength sampling and of poor fibre flatfield calibrations on sky subtraction are discussed. Computer simulations of fibre data have been

developed in order to characterise the contribution of the systematic errors to the signal to noise ratio (S/N). These simulations show that these systematic errors in some cases might be so large that even on a 4m telescope they will dominate over the Poisson noise in a typical long integration time and therefore the collection of more photons in an effort to give a better S/N will not work.

Autofib-1.5 was built (Parry & Lewis 1990) as a laboratory test-bed for new ideas in the run up to Autofib-2 and in this respect it has been very successful. One of the new features has been the incorporation of a multiway fibre connector into Autofib-1.5. Highly efficient multiway connectors suitable for astronomical applications are not commercially available. However, they are essential to make instrument changes much simpler, allowing a fibre bundle to be easily re-routed to different spectrographs.

An exhaustive laboratory evaluation of Autofib-1.5 was carried out to measure the performance of the fibre bundle with the purpose of determining the contribution made by the connector. The throughput of the complete set of fibres (55) at two different output f-ratios was measured. The positions of all fibres in each face of the connector was measured and a simple model to estimate the losses due to misalignments at the connector interface was developed. The results provided very useful information on the relative fibre performance of the system in terms of FRD. The Autofib-1.5 fibres throughput is limited mainly by Fresnel losses due to poor polishing techniques and FRD stress induced by the fibre end ferrules.

Based on the experience gained from the series of experiments for evaluating the Autofib-1.5 fibre bundle, a different technique was designed. The measurements are obtained by analysing the output beam from a fibre using a CCD-TV camera with a PC-based framegrabber. The reduction software required to analyse the data was developed and this technique was used to measure the throughput of different fibres and cross-check

the results with other techniques. This new method has greatly improved the efficiency compared with the methods previously developed in our laboratory. However it was still time consuming and therefore inconvenient for evaluating large numbers of fibres.

Another approach to the problem was developed to streamline the evaluation process even further. A key element of this new approach is a computer model of a fibres's FRD performance based on a known theoretical model for microbending induced beam-spreading. This theory characterises the FRD by a single parameter which can be determined by a very simple experiment, in which laser light is launched into the fibre and the far-field rings are observed and analysed. The model predicts the far-field output of a fibre for both collimated and uncollimated input beams. Such modelling can also include complicated phenomena such as tilted input beams and central obstructions without the need to setup experiments for specific cases. There is a good agreement between the predictions by the model and real experimental results.

This new technique allows us to use a simple parameter to characterise FRD performance. Therefore this will allow the study of which fibres and mounting techniques provide the minimum in FRD without the need for extensive instrumental setups. Furthermore different workers in the field will be able to compare results of various fibres in a well defined way. The method is very convenient for the evaluation of an instrument with hundreds of fibres. This technique has been tested at optical wavelengths but it is also suitable at infrared wavelengths where the problem of viewing and alignment is even more complicated.

Finally, a series of experiments in the infrared were carried out to measure the FRD of a silica fibre optimised to transmit up to 2μm. The throughput at both optical and IR wavelengths, for different input f-ratios was measured. Preliminary results show that the poor throughput obtained at the slow f/35 input, characteristic of IR chopping

secondaries, could be significantly improved by using microlenses to convert the input and output beam to a faster f-ratio, suitable for fibre work.

In this thesis the topics just described have been divided up in the following way. In chapter 2 the instrumental contributions to sky subtraction at faint levels are discussed and the results of the sky subtraction computer simulations are presented. Chapter 3 describes the main optical fibre properties and light propagation mechanisms within a fibre and the theoretical model developed to parameterise the fibre performance. Chapter 4 presents the optical fibre evaluation techniques developed in the laboratory. A comparison between the prediction from the model and the experimental results is carried out. Chapter 5 details the evaluation undertaken to measure the overall performance of the Autofib-1.5 fibre bundle with its connector. Finally, chapter 6 describes preliminary FRD results obtained in the infrared with a silica fibre.

2 SKY SUBTRACTION WITH FIBRES

2.1 Introduction

Multiple object spectroscopy with fibres offers two important advantages over multislit techniques: fibres can access the full telescope field and are capable of being used at high dispersion. However, the precision to which sky subtraction can be done is limited by systematic errors due to fibre to fibre response, focal ratio degradation, spatial fluctuations in the sky background amongst other factors and therefore fibres cannot currently match the limiting magnitudes reached with multislits (Ellis & Parry 1988). Although some very faint work has been reported by Barden *et al.* (1992b), who present a fibre spectrum of a galaxy with $R = 20.6$ and $B = 23.1$ obtained using a beam switching technique, this sort of result has not been routinely achieved.

In general, the sky and object signals recorded have both astronomical and instrumental contributions. This chapter is dedicated to the instrumental contributions that limit the precision of sky subtraction with fibres. A review of the main sky subtraction techniques with fibres is presented. The conditions that have to be satisfied to subtract the sky properly at faint levels, the sources of error and possible ways of eliminating them are analysed. The parameters involved in an accurate determination of the relative fibre

response (the so-called vignetting function) are presented via examples of vignetting functions obtained from an Autofib-1 observing run at the AAT. The consequences of deficient wavelength sampling and of poor fibre flatfield calibration on sky subtraction are discussed via results obtained from computer simulations of fibre data. The computer simulations allow us to model errors in deriving the relative fibre response and errors in resampling the data when attempting to arrange that the spectra from different fibres end up on the same wavelength scale.

In section 2.2 a summary of the sources of the night sky is given. Section 2.3 describes the basis of sky subtraction with multislits. Fibre spectroscopy and the instrumental limitations to sky subtraction with fibres are discussed in sections 2.4 and 2.5 respectively. Sky subtraction using the beam switching technique is described in section 2.6. The main sky observing techniques are discussed in section 2.7. In section 2.8 some examples of vignetting functions obtained during an Autofib-1 observing run at the AAT are given. In section 2.9 the results obtained from computer simulations of fibre data are presented. Finally, the conclusions are discussed in section 2.10.

2.2 The Sky

For faint object spectroscopy the limiting faintness for sky subtraction depends critically on the structure of the sky spectrum in the passband used. From approximately 4000$\AA$ to 6000$\AA$ the sky spectrum is relatively smooth while longward of 6500$\AA$ the sky spectrum is highly structured due to OH sky emission lines in that passband. Figure 2.1 shows the night sky spectrum in the wavelength range 5000$\AA$ to 10000$\AA$ taken very early, on a moonless night (after Parry 1986). This wavelength region is dominated by OH emission lines. The spectrum was obtained with the Faint Object Spectrograph (FOS) on the Issac

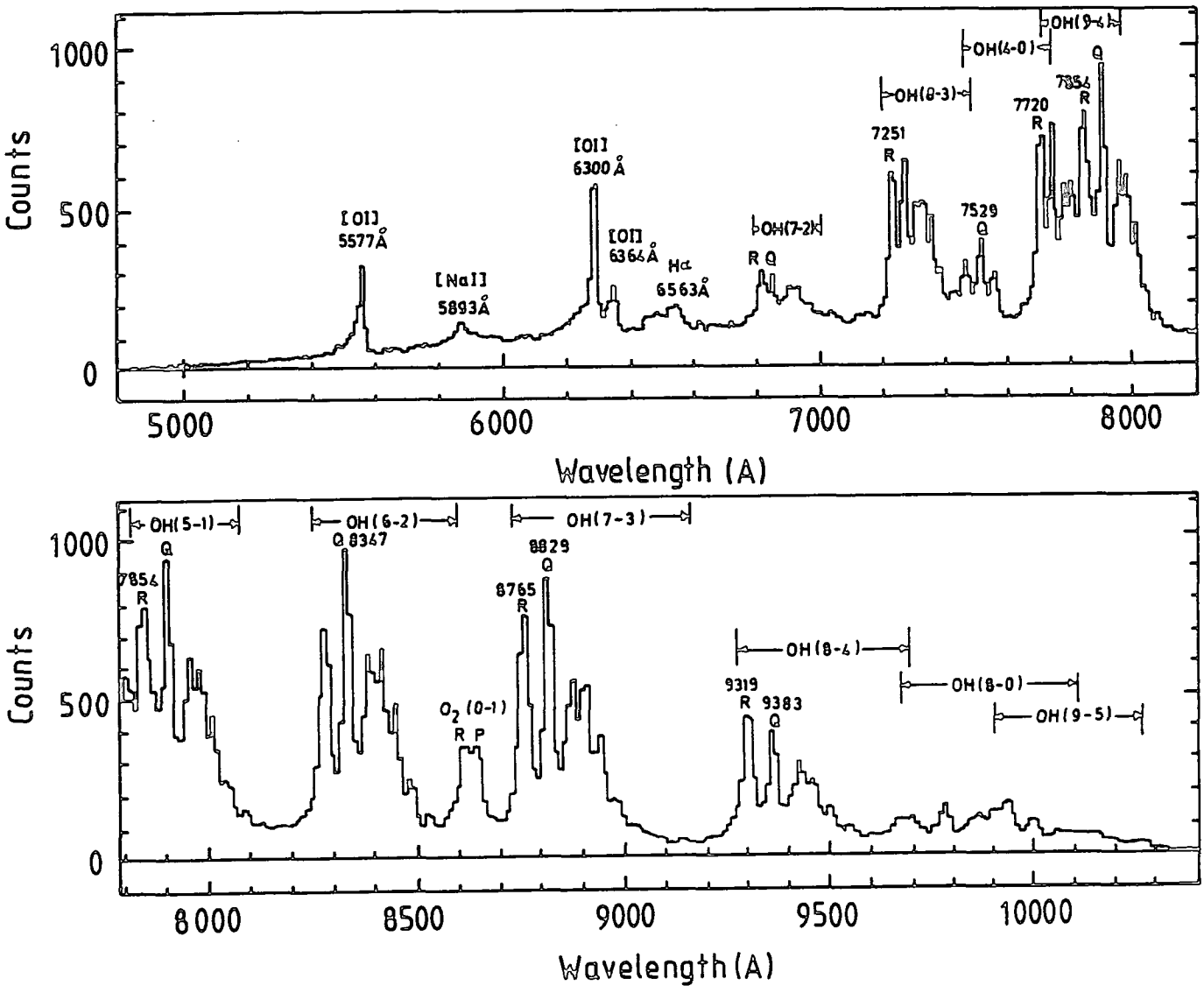

Figure 2.1. Night sky spectrum. Intensities are counts detected with the Faint Object Spectrograph (FOS) on the INT in 1000 seconds per pixel. The spectrum was taken soon after evening twilight. After Parry (1986).

Newton Telescope (INT) in La Palma. Because the sky spectrum is not highly structured in the blue and visual regions the fundamental limitation on sky subtraction is likely to be the non uniformity of the sky due to the distribution of faint discrete sources.

For sky subtraction purposes the most important parameters are the spatial and temporal scales of change of the night sky because these determine the extent to which sky monitoring must take place spatially adjacent to and simultaneously with recording of the object + sky spectrum. A comprehensive review of the spatial, wavelength and temporal variations of the sources of sky light is given by Chamberlain (1961).

A portion of the light of the night sky arises from direct starlight plus the diffuse Galactic light and the zodiacal light. These astronomical components will have spectra roughly similar to that of the Sun (Chamberlain 1961). The other major contributors to the night sky are the aurora and the atmospheric airglow which have primarily emission spectra.

Wyse and Gilmore (1992) have discussed the temporal and spatial variations of the night sky. Briefly, the zodiacal light is due to the scattering of sunlight by interplanetary dust. It varies smoothly but strongly with time of night, particularly near twilight, and with position on scales of the order of a degree. The auroral emission spectrum is complex, dominated by N, O, H, and N_2 lines and bands. Amongst the strongest features are [OI]5577$\AA$ and [OI]6300$\AA$. Fluctuations in the auroral spectrum are of orders of magnitude in intensity on time scales much less than seconds, but structure on angular scales much less than a degree averages out on timescales of minutes and longer.

The airglow consists of the nonthermal radiation emitted by the Earth's atmosphere. The main sources of emission are the atoms and radicals OI, NaI, O_2, OH and H as shown in figure 2.1. The radical OH emits in many lines in the near infrared and it has significant spatial fluctuations on scales of a minute of arc and above. The intensities

of these lines can vary with time during the night, with the season of the year and with airmass.

Amongst the complex resolved backgrounds are regions with significant diffuse Galactic light. The background originates in reflection and emission nebulosity and unresolved stars and clusters. While most obvious at low Galactic latitudes and in nearby galaxies it can also be present at high latitudes. There are fluctuations on small scales due to the distribution of very faint stars and galaxies which is intrinsically variable on scales smaller than a seeing disk. Thus, the variation in the contribution from these sources provides an irreducible minimum in one's ability to determine the sky flux underlying an object spectrum (Wyse & Gilmore 1992).

The variation of intensity of several emission lines during a relatively short, moonless, May night, measured by Parry (1986), is shown in figure 2.2. FOS data from La Palma were used to derived the results. The data show clearly that the intensity of the emission lines changes on times short compared to a typical integration time on a faint source. The results show that the OH emission fades as the night grows older and the different OH bands are strongly coupled. The author quotes early FOS data (1984) which indicate that the OH emission continues to fade further on the longer winter nights and the emission appeared to start off with an intensity similar to that seen in May. No obvious trend appears in the variation of the strong [OI] line at 5777$\AA$ but the [OI] lines at 6300$\AA$ decrease very significantly just shortly after evening twilight. It can be appreciated that the variations of the night sky are very erratic.

The temporal variability of the sky therefore, requires that we make simultaneous observation of the sky and the object. In general, for sky subtraction to be successful a sufficient number of carefully chosen sky areas must be observed so that the sky component of each sky + object spectrum can be accurately predicted. If there is an intrinsic variation

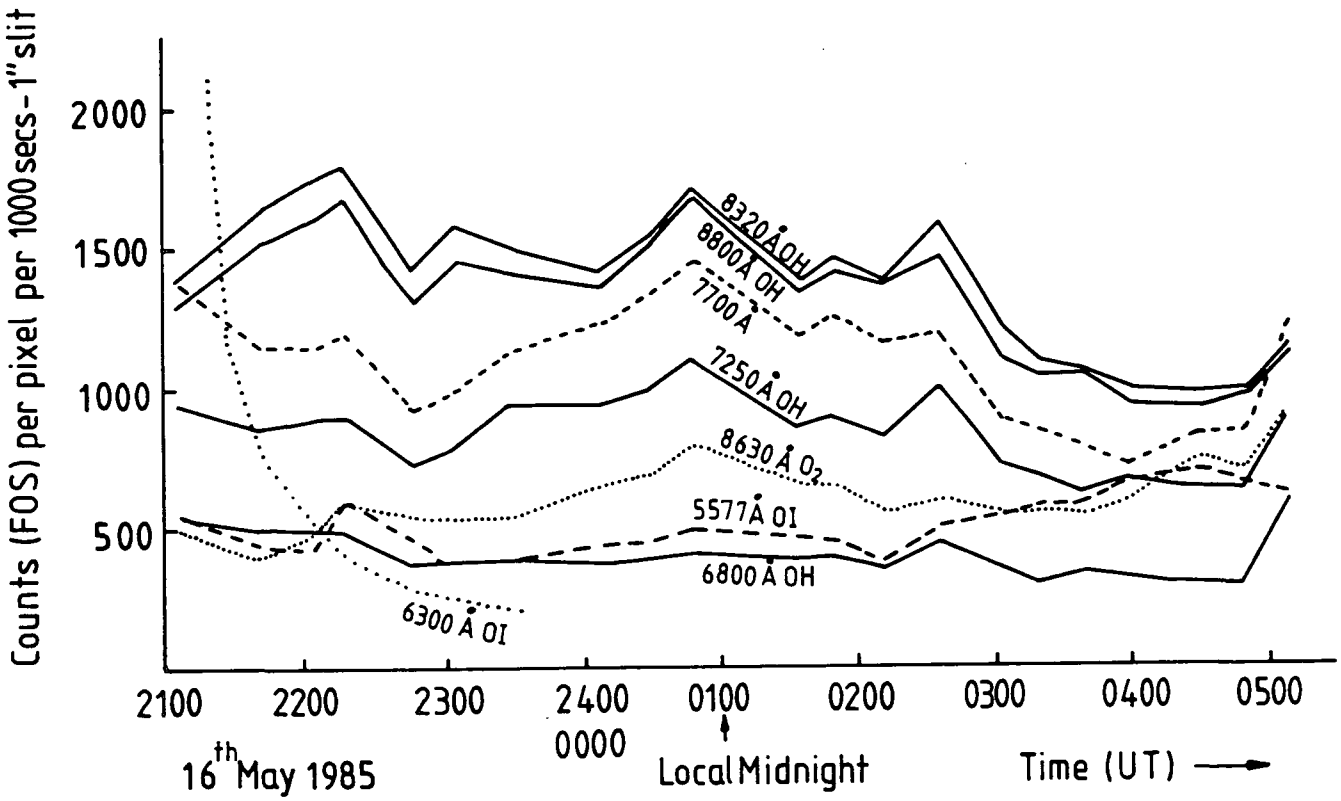

Figure 2.2. The variation of intensity of several emission lines during a relatively short, moonless, May night, measured by Parry (1986). FOS data from La Palma were used to derived the results which were normalised to account for variations in the slit width and exposure times used.

in sky emission across the field the sky observation should be planned so that sky spectra are measured at positions close to the objects.

2.3 Multislit and longslit spectroscopy

In these techniques each object is sky-subtracted using sky observations made with the same slit: sky from other slits is not normally used. Often, if there are regions of sky above and below the object, the sky spectrum is determined by interpolation.

Because the sky observations are local to the object, both in the telescope field and at the detector, systematic variations between the sky and sky + object observations are kept to a minimum. When interpolation is used the accuracy of the sky determination is further improved because sky brightness, sampling and optical throughput vary smoothly along the slit. Detector response and possibly slitwidth might not vary smoothly along the slit but these variations tend to be small and can be simply flatfielded out. Also background light from scattering in the spectrograph varies smoothly and can be accurately subtracted off.

Thus for multislit work the adjacency of the sky and object keep systematic errors down to a minimum and interpolation reduces them still further, making them small in comparison to the Poisson noise contribution. For these reasons slit spectroscopy can reliably give useful spectra at very faint limits $B \lesssim 24$ when very long integration times are used.

2.4 Fibre spectroscopy

For very faint objects we wish to subtract a sky spectrum from a sky + object spectrum to derive the object spectrum on its own. Because the object signal is small in comparison to the sky background we are concerned with the subtraction of two similar quantities from each other to give a much smaller quantity. Small errors in the observed quantities can therefore give rise to large errors in the result. The sky and object measurements are obtained simultaneously but with different instrumentation which will have different responses. Furthermore each measurement includes a contribution from scattered light *i.e.* light from other fibres. We can write the actual object measurement and its error at a given wavelength as

$$M_0 = Q + S + B_0 \pm \sqrt{Q + S + B_0} \tag{2.1}$$

where Q is the signal from the object, S is the signal from the sky and B_0 is the contribution from scattered light. Similarly for a sky measurement obtained with a single fibre we have

$$M_s = gS + B_s \pm \sqrt{gS + B_s} \tag{2.2}$$

where g is the relative efficiency of the sky channel with respect to the object channel and B_s is the contribution from scattered light for this sky fibre. In the above we are assuming that any bias measurement has already been trivially removed and any readout noise is negligible.

Unfortunately we do not know g, B_0 or B_s exactly but we can estimate these quantities from other calibration data such as offset sky exposures, dome flats, single

illuminated fibres, etc. Let us denote our estimates of g, B_0 and B_s by γ, β_0 and β_s respectively. Firstly we can correct our measurements M_0 and M_s for background light

$$M_0^* = M_0 - \beta_0 = Q + S + B_0 - \beta_0 \pm \sqrt{Q + S + B_0 + \epsilon_0^2} \tag{2.3}$$

$$M_s^* = M_s - \beta_s = gS + B_s - \beta_s \pm \sqrt{gS + B_s + \epsilon_s^2} \tag{2.4}$$

where ϵ_0 and ϵ_s are the statistical uncertainties in β_0 and β_s. Finally to do the sky subtraction and obtain an estimation of Q we multiply equation 2.4 by $1/\gamma$ and subtract it from equation 2.3 to obtain

$$\textit{derived object signal} = Q + E_1 + E_2 + E_3 \pm E_4 \tag{2.5}$$

where:

$$E_1 = (1 - g/\gamma)S$$

$$E_2 = B_0 - \beta_0$$

$$E_3 = (\beta_s - B_s)/\gamma$$

$$E_4 = \sqrt{Q + (1 + g/\gamma^2)S + B_0 + B_s/\gamma^2 + \epsilon_0^2 + \epsilon_s^2/\gamma^2}$$

E_1 to E_3 are systematic errors introduced by errors in determining γ, β_0 and β_s. Ideally if we have no such errors then $\gamma = g$, $\beta_0 = B_0$ and $\beta_s = B_s$ and then $E_1 = E_2 = E_3 = 0$. The term E_4 denotes the random Poissonian error and is reduced in size relative to Q by increasing the exposure time, decreasing the sky brightness and decreasing the background scattered light contribution.

For sky subtraction to be successful the systematic error should be small in comparison to the Poissonian noise which in turn must be small in comparison to the signal. Note that the signal and the systematic errors are proportional to the exposure time t whereas the Poissonian noise is proportional to $\sqrt{t}$. This means that the signal-to-noise (S/N) ratio increases with $\sqrt{t}$ when the systematic errors are low but remains constant no matter how long the exposure, or how big the telescope, once the Poissonian errors have fallen below the systematic errors. In some cases the systematic errors may be so large that even on a 4m telescope they will dominate over the Poissonian noise in a typical long integration time and therefore the collection of more photons in an effort to give a better S/N ratio will not work —one would just get increasingly larger amounts of bad data.

Instrumentally, three conditions have to be satisfied in order that systematic errors associated with sky subtraction are smaller than the Poissonian errors:

1) For each wavelength channel, the sky spectrum must be sampled in exactly the same way as in the sky + object spectrum from which it is subtracted.

2) The instrumental response of the sky + object pixels relative to the pixels used for sky spectrum determination, γ, must be accurately known for each wavelength channel.

3) The scattered light contribution β_0 and β_s must be known accurately.

A typical fibre observation might consist of 50 objects and 10 sky spectra. A calibration arc source illuminating every fibre is used to independently wavelength calibrate each fibre spectrum so that they can all be resampled to the same wavelength calibration. The resampling in the wavelength direction (scrunching) will not work unless the spectrum is sufficiently well sampled in the wavelength direction. Often this is not the case and so condition 1) above is not fulfilled. If the sky spectrum is smooth, sampling

errors are not too troublesome if one is only attempting to identify spectral features e.g. for redshift determination. However, in the near IR the OH spectrum is both strong and highly structured —as shown figure 2.1 — and therefore it is essential to fulfil condition 1) at faint levels.

The relative responses of the fibres γ are obtained using offset sky exposures where the telescope is deliberately offset so that the fibres observe sky. In practice the offsets are kept as small as possible to minimise differences in fibre throughput between the object and calibration exposures. The sky is assumed to be constant across the field and that variations in the integrated counts for each fibre spectrum are due to instrumental effects. Throughout a long exposure several offset exposures in different directions on the sky are taken to monitor fibre variations throughout the run and also to ensure that objects accidentally observed during offset sky exposures can be eliminated using median filtering techniques. The relative responses are calculated for the entire wavelength range. Variations in relative response with wavelength are assumed negligible although often the results show that this assumption is clearly wrong.

Once all the spectra have been flat fielded, wavelength calibrated and rebinned the sky spectra are averaged to derive a sky spectrum with reduced Poisson noise. This is then subtracted from each sky + object spectrum. The reasons why this simple recipe fails to produce good sky-subtraction are discussed in the next section.

2.5 Instrumental limitations

The wavelength sampling of a sky + object spectrum and the average sky spectrum may not be the same for several reasons:

a) The fibre slit may not consist of a precise straight line of fibres due to inaccurate construction.

b) The fibre slit may be rotated with respect to the detector's pixel grid

c) There may be distortions due to the spectrograph optics (barrel or pincushion distortion) or the detector (S-distortion).

Although in principle these errors can be corrected by wavelength resampling (scrunching), in practice this is unlikely to be accurate enough particularly for effect c) which can alter the line widths as well as the line positions.

The relative efficiency of the fibres depends on several factors. Firstly, there are variations introduced by the fibres themselves due to:

a) *The quality of the fibre end preparation.* In order to minimise FRD it is important to ensure good flatness, surface smoothness and squareness when polishing all the fibre ends. Anti-reflection coatings and cleanliness are also important in minimising the fibre losses.

b) *Absorption losses.* These will depend on the fibre type and the length of the fibres.

c) *Connector losses.*

Secondly, there are variations in instrumental response due to the operational conditions *i.e.* the throughput of a spectrographic fibre at the telescope depends on:

a) *The alignment of the fibre with the incoming telescope beam.* If the axis of the fibre is not aligned with the principal ray, the f-number at the fibre output will be smaller than at the input (focal ratio degradation) and the spectrograph will be unable to accept all the light. The size of these misalignments depends on the design and performance of the fibre positioning system and they are non-trivial to eliminate entirely, particularly for wide-field systems where the angle the principle ray makes with the focal plane increases with field angle and can be large (2°–4°) at the field edge.

b) *The alignment of the fibre with the spectrograph optics.* The fibre slit should be made to satisfy the pupil imaging requirements of the spectrograph, either by fanning out the fibres or using a field lens. If this is not done off-axis fibres may be severely vignetted.

c) *Stress related FRD.* This will be determined by the fibre type, the bundle construction and the routing used. Stressful flexure of the fibre could increase the FRD and, as a consequence, overfill the collimator.

Resampling in the wavelength direction and obtaining of the fibre's relative response (vignetting function) are attempts to correct for the combination of all these effects. However, the results obtained so far with this technique are not as good as those obtained with multislits at very faint levels. It is therefore very important to analyse the deficiencies of the method.

The relative responses are calculated from the total amount of light in each fibre. This ignores the possibility of a variation in sensitivity with wavelength from fibre to fibre. Although the fibres themselves are intrinsically "grey" the relative fibre sensitivities will often have a wavelength dependence because of the vignetting of the spectrograph. Consider a vignetting function obtained for a wavelength at the centre of the detector.

There the fibres at the centre of the slit will be more efficient that those near the edge, due to the vignetting in the spectrograph. If another vignetting function is obtained for a wavelength at the edge of the detector the relative efficiency of the fibres at the centre of the slit to those at the edge will be less than that in the former case *i.e.* the shape of the vignetting function will be flatter. This is simply because the spectrograph optics have radial symmetry about the field centre and the wavelengths near the edge will be more uniformly vignetted than those at the centre. The extent of this wavelength dependence has not been properly studied and could be significant for faint object spectroscopy.

The spectrograph properties are also relevant for sky subtraction. Multifibre systems have been used, in general, with spectrographs designed for single object or longslit spectroscopy and as a consequence the fibres located at the ends of the slit might have a different point spread function than those at the centre of the slit. For example, Barden (1992b) reports that one of the main sky subtraction problems associated with the plugboard system NESSIE has been due to the presence of coma in the off-axis images of the spectrograph. Spectra from fibres in one region of the slit will have a different width to the profiles of spectra from another region. This difference will introduce errors when subtracting sky emission spectra obtained from different locations along the slit.

The effect of spectrograph scattered light on the accuracy of sky subtraction has been discussed recently by Wyse and Gilmore (1992). Results obtained during an Autofib-1 observing run at the AAT, using the RGO spectrograph show that light appears as both a quasiuniform background and as a local scattering adjacent to bright sources. Analysis of the observations of bright stars show that $\sim 2\%$ of light from a fibre illuminated by a bright source is scattered into the adjacent 5 or 6 extracted fibres each side, so that a total of $\sim 4\%$ of the flux in any spectrum is scattered into nearby spectra. The uniform scattered light which exists within the spectrograph has a local intensity simply proportional to the total incident light and depends on the spectrograph configuration. For one specific

grating angle, $\sim$ 13% of the total intensity in a frame is scattered uniformly across all the extracted spectra.

The authors remark that special exposures are required to calibrate the local scattered light properties of the spectrograph/detector in use and to calibrate the relationship between the total number of counts in a data frame and the uniform scattered light level recorded on the detector. Calibration of the correction for local scattered light requires the observation of a bright source at several locations along the slit. The local and uniform scattered light must be subtracted from the contaminated fibres prior to the determination of the relative sensitivities of the fibres.

The following results obtained by Wyse and Gilmore (1992), with the plugboard system FOCAP at the AAT, illustrate the importance of considering the properties of the scattered light for a particular spectrograph/detector combination. The residual counts in "unexposed" areas of the detector provide the means of checking that the scattered light has been properly handled, by simply processing the dead fibres in the same ways as the object fibres. For example, the mean count of the 7 sky spectra before subtraction, was 32.8 photons per angstrom. Data obtained with a sky subtraction technique that ignores any contribution from local and uniform scattered light show that the mean count in the dead fibres is about 15.1 counts, or 46% of the mean sky count before subtraction. Obviously, the scattered light has not been properly subtracted. In comparison, the results obtained for the same data frame corrected to allow for scattered light show that the mean count in the dead fibres is 1.8 counts, or 5.6% of the mean sky count before subtraction.

The residual counts in sky-subtracted sky spectra provide an estimator of the precision of continuum sky subtraction. In the former case the mean of the 7 sky-subtracted sky spectra was 0.13 photons, so the mean residual was 0.4%. However it is not reliable as evidenced by the large positive residuals left in the dead fibres. In the second case the

mean of the sky-subtracted spectra is 0.03 photons, so the mean residual is only 0.1% and the sky subtraction is reliable.

In summary, sky subtraction with fibres does not use adjacency at the slit or in the field and so systematic errors between the sky and the sky + object observations tend to be large and interpolation cannot be used to derive γ. Variations in individual fibre properties further increase the systematic errors. For these reasons sky subtraction with fibres is limited by systematic errors and much care is needed when observing and reducing the data if fibres are to provide useful results at the faint magnitudes currently reached with multislits. Nevertheless, there is nothing fundamentally impossible about doing good sky subtraction with fibres so improved techniques that allow us to accurately determine γ, β_0 and β_s, should eventually allow fibres to go as deep as slits.

2.6 Beam switching

It is widely believed that a way of improving sky subtraction is to use the beam switching technique. Although it can be useful for certain type of observations it also has its deficiencies. The principles of the technique are described in detail by Parry (1986). In this method of sky subtraction two separate apertures are used, one for the object and the other for the sky. The object is switched between the two apertures so that it spends exactly half the total exposure time in each aperture. It is assumed that the sky is intrinsically the same in both apertures. The sky that is subtracted from the object + sky spectrum is not strictly obtained simultaneously.

In the particular case of fibres, the sky and sky + object measurements are switched between two different fibres (fibre A and fibre B) by offsetting the telescope position. For

one half of the exposure time, let the sky + object measurement in fibre A and its associated error for each wavelength channel be

$$object\ measurement = C_{1A} = Q_1 + S_1 \pm \sqrt{Q_1 + S_1} \tag{2.6}$$

and similarly for the sky measurement in fibre B we have

$$sky\ measurement = C_{1B} = gS_1 \pm \sqrt{gS_1} \tag{2.7}$$

where Q_1 is the signal from the object, S_1 is the signal from the sky and g is the relative efficiency of channel B with respect to channel A. For the other half of the exposure time the sky measurement in fibre A will be given by

$$sky\ measurement = C_{2A} = S_2 \pm \sqrt{S_2} \tag{2.8}$$

and similarly for the object measurement in fibre B,

$$object\ measurement = C_{2B} = g(Q_2 + S_2) \pm \sqrt{g(Q_2 + S_2)} \tag{2.9}$$

Again, we do not know g exactly but we derive the quantity γ which is an estimate of g. To do the sky subtraction we multiply equation 2.7 and equation 2.9 by $1/\gamma$ and the derived object signal will be given by

$$R = (C_{1A} - C_{1B}/\gamma) + (C_{2B}/\gamma - C_{2A}) \tag{2.10}$$

$$R = Q_1 + Q_2\left(\frac{g}{\gamma}\right) + (S_2 - S_1)\left(\frac{g}{\gamma} - 1\right) \pm \sqrt{Q_1 + (g/\gamma^2)Q_2 + (S_1 + S_2)(1 + g/\gamma^2)} \quad (2.11)$$

The first and second terms represent the signal itself, the third term is the systematic error and fourth term is the Poisson noise.

If the relative fibre response is estimated perfectly then $g/\gamma = 1$, the total signal is equal to $Q_1 + Q_2$ (which is the desired result) and the error associated to the measurement is only due to the Poissonian noise. Furthermore, if $S_1 = S_2$, then the total signal detected is $Q_1 + Q_2(g/\gamma)$ which is independent of the sky spectrum even if $g/\gamma \neq 1$.

It should be noted that for $S_1 = S_2$ the observed conditions must be either photometric, which is not always the case, or else the object must be switched often and accurately between the apertures to average out temporal variations. However, the latter option requires a detector with negligible readout noise.

In a typical observation, the faint objects are switched between two different fibres by offsetting the telescope position. The temporal variability of the sky is monitored by dedicating a few fibres to observe only the sky for both beam positions. The residual sky $(S_2 - S_1)(g/\gamma - 1)$ is removed after the beam switched skies are subtracted from their respective object spectra (Barden 1992b) by using the dedicated sky fibres.

The advantage of this technique is that the total data acquired for the sky and the object + sky channels are obtained using the same instrumentation in every last detail, so many of the instrumental errors discussed in the previous section are avoided. For example, the wavelength sampling of fibre A and fibre B may be very different in terms of resolution and zero point. But the total object + sky spectrum and the total sky spectrum that is subtracted off it are identical convolutions of the wavelength sampling of fibres A

and B and therefore condition 1) in section 2.4 holds. Nevertheless, the correction for the temporal variability of the sky introduces the need to determine the fibre to fibre relative transmissions.

The main disadvantage of the method is that there is a very large waste of observing efficiency, as more than half of the available fibres are committed to sky measurement at all times. The loss in multiplex gain is a factor of two over an observing approach which could utilise just the dedicated sky fibres. Also, despite the large number of sky fibres each object is sky-subtracted using only one fibre and the Poisson noise is therefore 2 times higher than for a technique that correctly uses many (> 10) sky fibres.

2.7 Sky observing techniques

There are basically two approaches to monitoring the sky: either simultaneously with the object + sky measurement or separated in time. Within the former there are two options. The first and more common one is to dedicate a subset of fibres ($\sim$ 15%) for measurements of sky exclusively. The locations of these fibres are ideally determined from deep prime focus photographs. The telescope is offset periodically to monitor the variation in the fibre to fibre response as the telescope tracks the field. The sky spectra are flat fielded, wavelength calibrated and rebinned. Then, they are compared to each other to remove any spectrum contaminated by a faint source. The remaining spectra are averaged together and the resultant sky spectrum is then subtracted from all the object spectra. The main advantages of this technique are its flexibility and that it maximises the number of observed objects.

In the second method for making simultaneous sky measurements, the sky is measured adjacent to the sky + object by using pairs or arrays of fibres. An example of such a system is MX (Hill & Lesser 1989) for which in addition to the object fibre, each probe contains a two arcsec fibre 40 arcsec farther back on the probe tip. This approach has the advantage that the sky is measured close to the object and is analogous to the multislit method.

As in the previous case, the sky fibre spectra are processed in exactly the same fashion as the object spectra. The relative transmission of the two fibres must be known to a higher precision than the precision of the sky subtraction itself. For some programs where the sky is flat to a few percent across the field the use of the median of the best 15 or 20 sky fibres provides a sky spectrum with good signal to noise (Hill & Lesser 1989). This approach has a substantially reduced multiplex advantage and the multiplex gain is reduced by a factor of two because half of the fibres are dedicated to sky measurements. Another disadvantage is the potential contamination of the sky fibre by a faint source in which case the observation of that object is lost.

The simplest case of sky and object + sky measurements separated in time, involves integration of the object + sky for half the time in the fibre, offsetting the telescope to remove the object from the fibre and integrating on the sky. This observing method has the advantage of removing any dependence on relative fibre sensitivities. However the sky does vary in intensity as a function of time and although the intensity of the emission lines can be scaled, the fact that there is not an independent measurement of the sky continuum intensity implies that this approach cannot provide optimum sky subtraction (Wyse & Gilmore 1992). A variation of this method is the beam switching technique described in the previous section in which the sky and the object + sky are switched between two fibres and a few dedicated sky fibres monitor the sky in both positions.

2.8 Determination of the relative fibre response

The determination of the fibre sensitivities is non-trivial since the overall transmission varies substantially between fibres. A reasonable approximation to the relative fibre transmission is obtained from short offset-sky exposures, or lamp flat fields, or twilight exposures. However, the results obtained with the three methods might be different and therefore lead to poor sky subtraction. The main problem with artificial sources is to achieve very uniform illumination over the full field of the focal plane.

During an Autofib-1 observing run at the AAT in 1990 several exposures of the night sky, the twilight and dome flats were obtained to study the variation in the vignetting function. Autofib-1 was used in combination with the RGO spectrograph and the IPCS. The data were reduced in the standard way *i.e.* for each frame the spectra were extracted, wavelength calibrated and rebinned onto a uniform wavelength scale. It is then assumed that the fibres all have indistinguishable spectral transmission properties so only the total number of counts per spectrum is required. After normalization to some convenient value these data represent the relative fibre sensitivities.

Ideally the exposures to correct for the relative fibre transmission must be obtained with the fibres configured for the observing field. In a typical observing run a twilight exposure is obtained at the beginning of the night and another at the end of the night. The vignetting function obtained from the twilight exposure closer in time to the observing field is used to correct for the relative fibre response. However, if more than two fields are observed during the night the corrections for some of the fields have to be done from exposures obtained with the fibres in a different configuration and this will introduce errors in sky subtraction. Figure 2.3 (a) shows two vignetting functions obtained from twilight exposures. The solid line is the vignetting function obtained at the beginning of the night and the curve in dotted lines is that obtained at the end of the night with a different

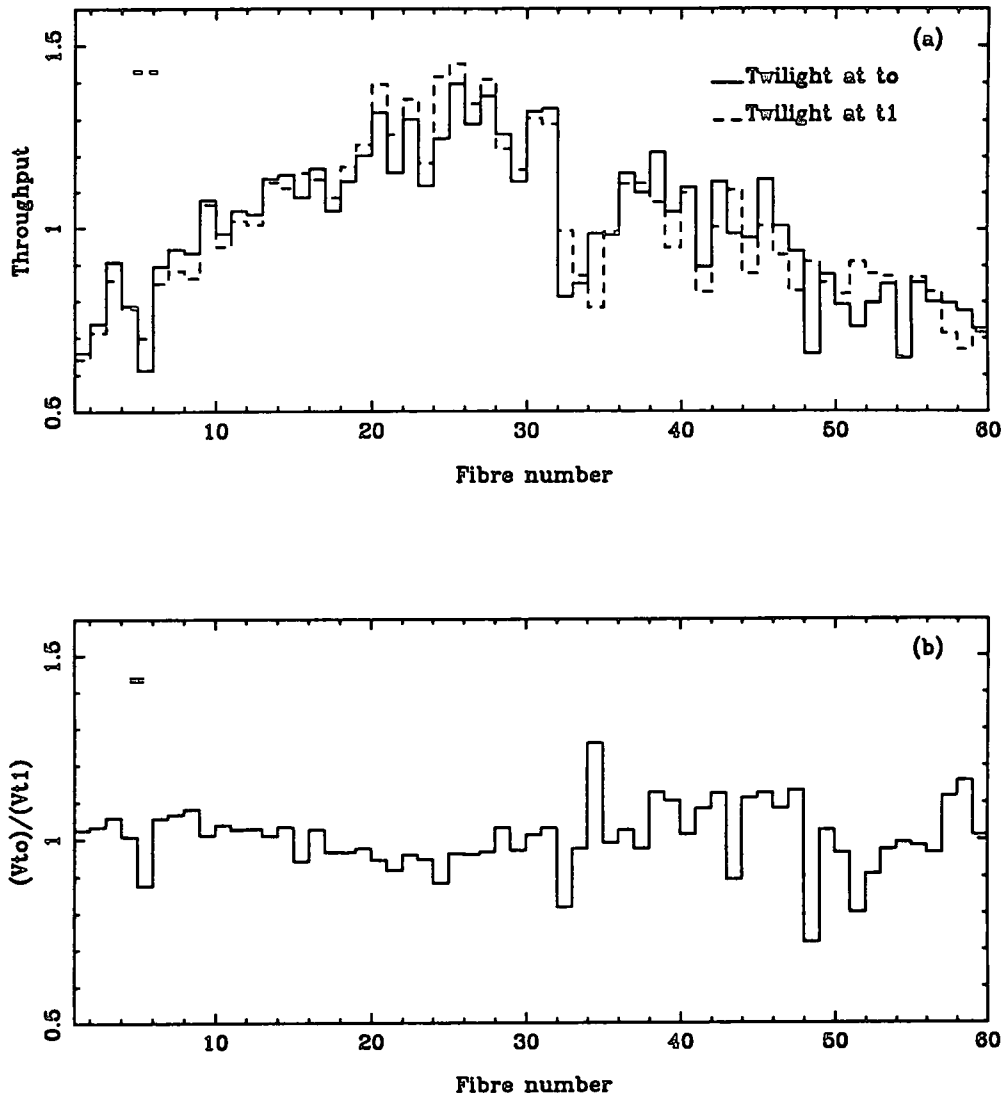

Figure 2.3. Data obtained during an Autofib-1 observing run at the AAT in 1990. a) The solid line is the vignetting function V_{t0}, obtained from a twilight exposure at the beginning of the night. The dotted line V_{t1}, is that obtained at the end of the night with the fibres in a different configuration. b) Ratio between the two vignetting functions.

fibre field configuration. Figure 2.3 (b) presents the ratio between the two functions. The differences obtained for many fibres are well above the Poissonian errors, as indicated by the error bar (σ) in the top left hand corner.

An alternative method is to obtain a dome flat by observing a screen located on the side of the dome and illuminated by a bright lamp. When obtaining dome flats care must be taken to prevent light scattering directly onto the focal plane from the telescope structure or elsewhere. The dome flats can potentially give good results if a minimum amount of light is scattered all over the telescope. To compare results, for the same fibre field configuration four exposures were obtained: a twilight, a night sky, a tungsten dome flat at full intensity and another one at 3/4 of full intensity. The latter two were obtained with the telescope pointing to the zenith.

Figure 2.4 (a) presents the vignetting functions derived from the offset sky exposure (solid curve) and that obtained from the twilight exposure (dotted curve). Figure 2.4 (b) shows the ratio of the two curves. Clearly, there are significant differences ($> 3\sigma$) for some fibres close to the centre of the slit and for those at the ends of the slit. A similar situation is obtained for the ratio between the dome and the offset sky vignetting functions, see figure 2.6 (a) and (b).

The differences in the results obtained from the dome flat exposures are not particularly sensitive to the intensity of the lamp as shown in figure 2.5 (a) and (b) where for most of the fibres the differences are within the Poissonian errors. In figure 2.7 (a) and (b) the fibre relative response curves obtained from the dome flat and the twilight exposures are compared.

In general the results obtained from the twilight and the dome exposures do not differ significantly, while those obtained from the night sky exposures present a difference depending of the fibre position on the slit. The results suggest that the central fibres are

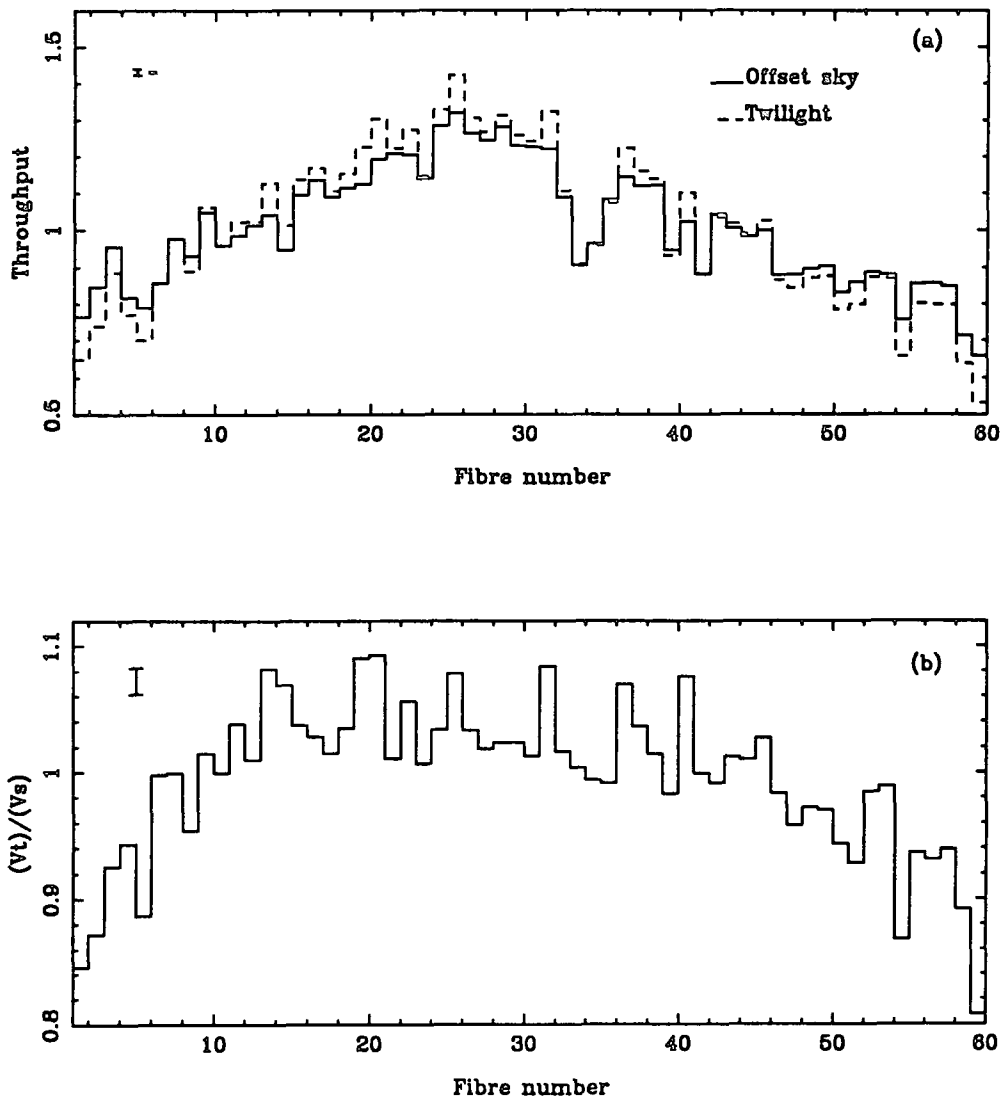

Figure 2.4. Data obtained during an Autofib-1 observing run at the AAT in 1990. a) The solid line is the vignetting function V_s, obtained from a night sky exposure. The dotted line V_t is that obtained from a twilight exposure at the beginning of the night. Both exposures were obtained with the fibres in the same configuration. b) Ratio between the two vignetting functions V_t/V_s.

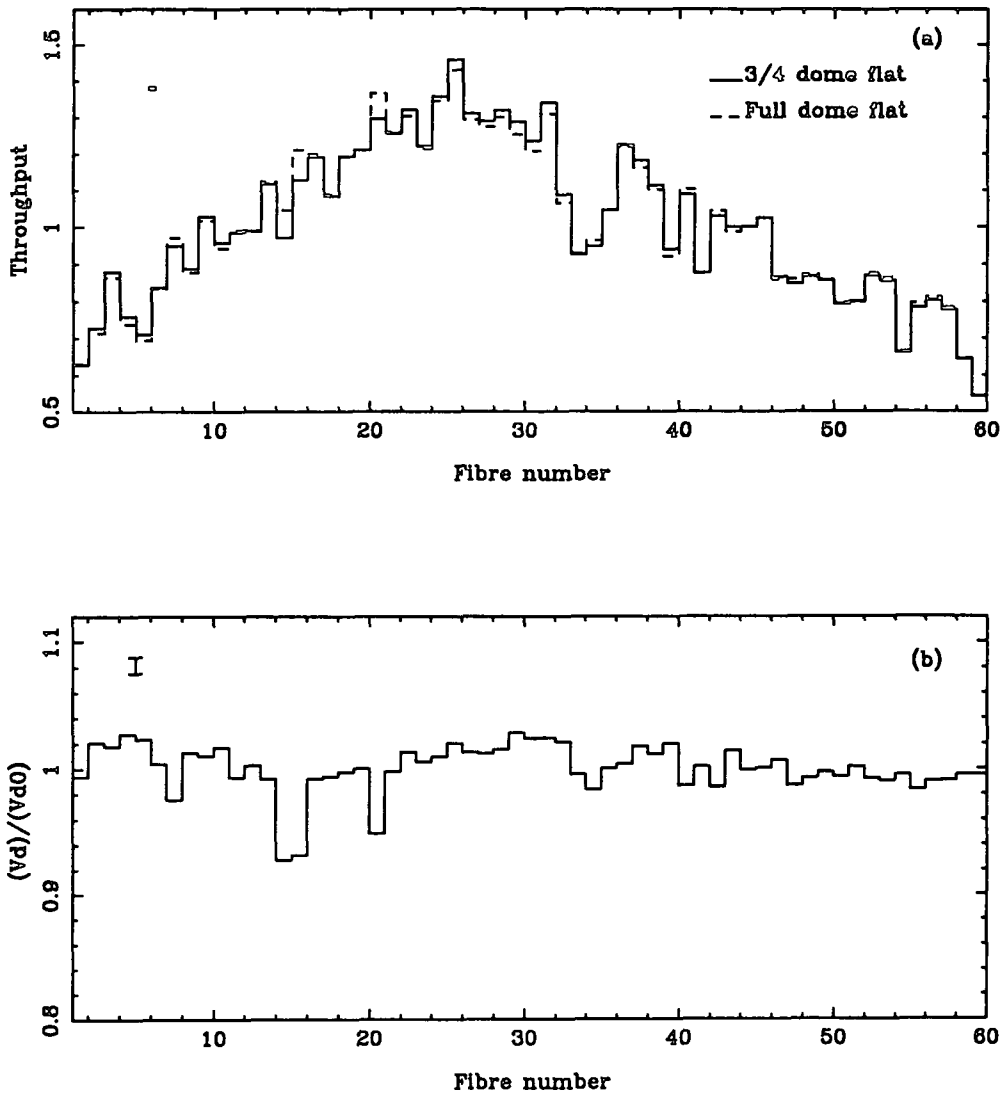

Figure 2.5. Data obtained during an Autofib-1 observing run at the AAT. a) The solid line is the vignetting function V_d, obtained from a dome flat with the tungsten lamp at 3/4 of full intensity and the dotted line corresponds to that obtained with the tungsten lamp at full intensity V_{d0}. b) Ratio of the vignetting functions obtained from the dome flat exposure V_d/V_{d0}.

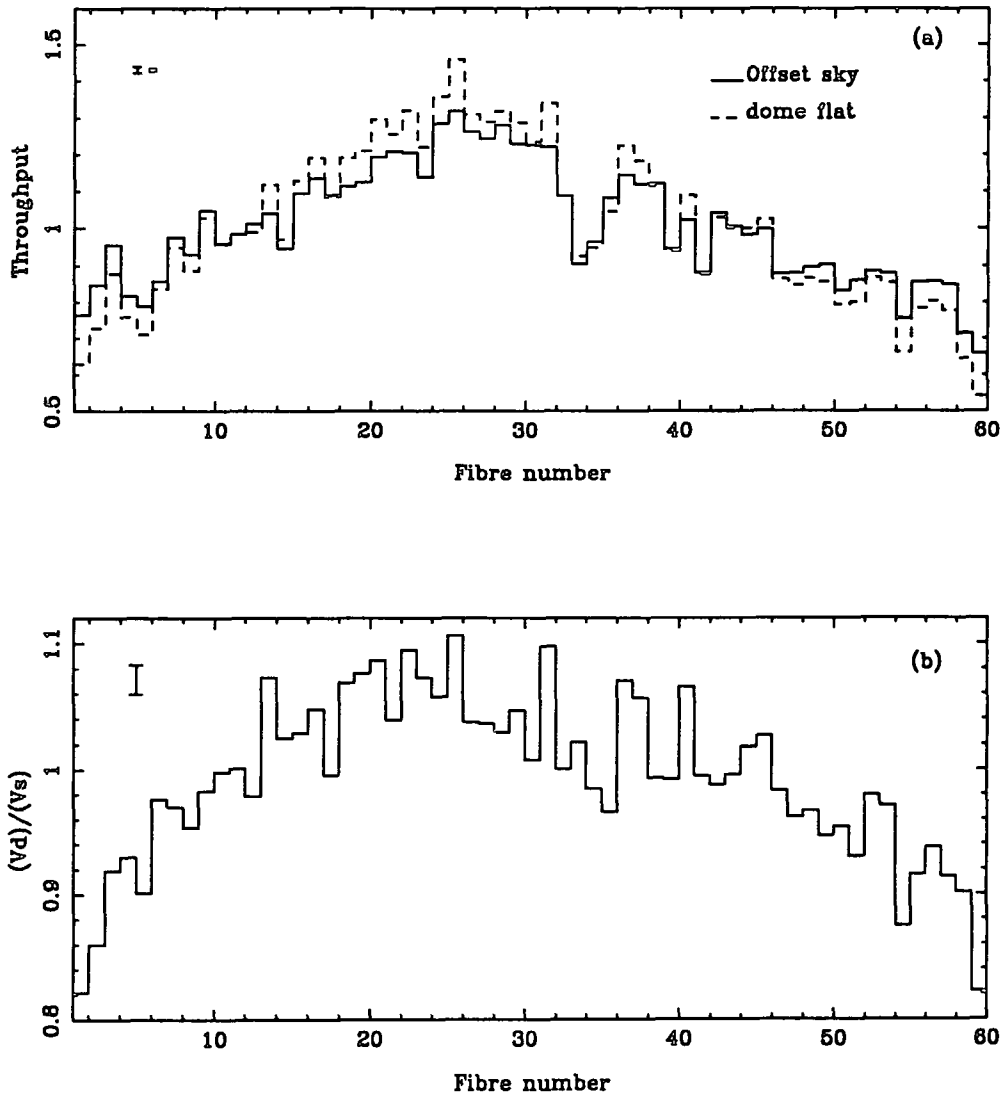

Figure 2.6. Data obtained during an Autofib-1 observing run at the AAT. a) The solid line is the vignetting function V_s from an offset sky exposure and the dotted line corresponds to that obtained from a dome flat exposure V_d. b) Ratio of the two vignetting functions V_d/V_s.

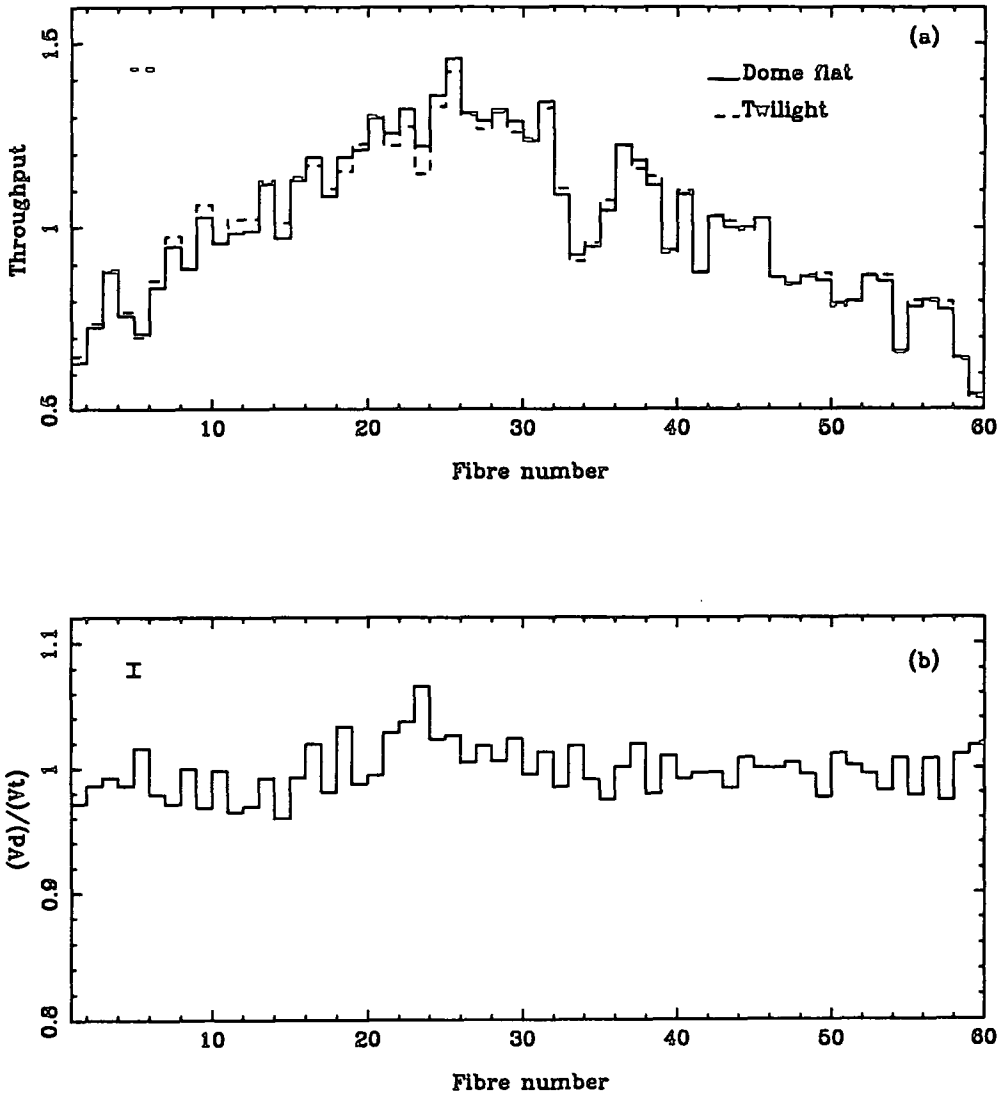

Figure 2.7. Data obtained during an Autofib-1 observing run at the AAT. a) The solid line is the vignetting function V_d, obtained from a dome flat exposure and the dotted line corresponds to that obtained from the twilight exposure V_t. b) Ratio of the vignetting functions V_d/V_t.

more efficient relative to those near the ends when they are illuminated by the twilight sky or a dome flat rather than with the night sky. One would expect that the illumination is not as uniform across the field with the twilight or the dome flat as it is with the night sky but it is difficult to see how this could account for the observed vignetting functions. The difference is more likely caused by the different count rates but it is not clear exactly how.

No correction for scattered light in the spectrograph was applied and in principle the inclusion of these corrections would improve the results. According to the results of Wyse and Gilmore (1992) the uniform scattered light is proportional to the total incident light, therefore it would be expected that the amount of scattered light would be less for the offset sky than for the twilight or the dome exposures. No correction to compensate any drift in the spatial stability of the IPCS was applied. Including corrections for this effect may also improve the results.

The results clearly show that different values of the vignetting function can be obtained for the same fibre field configuration depending on the source of illumination. The cause of these variations must be understood. The examples given above do not represent an exhaustive study of the fibre relative response curves but illustrate some of the many factors involved in the determination of the vignetting function. The results obtained can be summarised as follows:

1) The general shape of the vignetting function is dependent on the source type — fainter sources produce flatter curves.

2) Changing the field configuration affects a few fibres but the general shape of the vignetting function is not changed.

3) Some fibres appear to change significantly from one vignetting function to the next even when the light source and the configuration are the same.

More careful measurements are needed to see how the relative fibre transmission varies and after applying the correction for scattered light to study the causes of the differences. The wavelength dependence of the relative response should also be considered perhaps by replacing faint offset sky observations with brighter artificial calibration sources to give good signal to noise.

To quantify how a poor determination of the vignetting function affects the sky subtraction computer simulations were developed and some results are described in the following section.

2.9 Computer simulations

In order to characterise the contribution of the systematic errors to the Signal to Noise (S/N) ratio, computer simulations of fibre data have been made and some preliminary results are shown. The computer simulations allow us to model errors in deriving the relative fibre responses and errors in resampling the data when attempting to arrange that the spectra from different fibres end up on the same wavelength scale. These simulations then allow us to quantify how these errors affect the sky subtraction.

The program creates a continuum as the flux received from an object of magnitude m (energy per unit area, per sec, per unit wavelength interval) multiplied by the aperture of the telescope A, the integration time t and the wavelength interval. The number of photons is obtained by dividing this quantity by the energy of a photon of wavelength λ. The number of counts for each channel is then calculated by multiplying the photon number

by an efficiency factor E. This factor depends on the individual efficiencies associated with the atmosphere, the telescope, the spectrograph and the detector. To introduce the photon noise, the value X_o associated with each channel is replaced by a number taken randomly from a Poisson distribution with mean X_o.

The sky spectrum is created by generating Gaussian emission lines superimposed on a continuum of magnitude 21.5. The parameters of the lines are created randomly and do not correspond to real sky emission lines —although of course the same random sky spectrum form is used throughout the simulations. Given the system parameters *i.e.* telescope aperture, integration time, efficiency and object magnitude, three spectra are created with their associated photon noise: sky, sky + object and object without sky, the latter being used as a reference.

In order to evaluate how different sampling between the sky spectrum and the sky + object spectrum affects the sky subtraction, the sky is shifted before doing the subtraction. To investigate the effect of incorrectly estimating the difference in the instrumental response of the sky + object fibre relative to the fibre used for sky spectrum determination, γ is approximated by the constant *Vignetting* and the sky spectrum is multiplied by this factor before subtraction. In other words we deliberately scale the sky by the wrong amount before subtraction ($\gamma \neq 1$ even though $g = 1$).

Examples of the spectra obtained are shown in figure 2.8, where the input parameters are: telescope aperture A=*4.2m*, efficiency factor E=*10%*, integration time t=*7000* sec and object magnitude m=*22*. These spectra have count levels that are consistent with real observations (see Parry 1986), with a dispersion of 3.5Å per pixel. The first spectrum is the sky spectrum and the second one is the reference object spectrum. The latter is the spectrum which would be obtained if the sky were completely black. The equivalent width of the lines are $\sim$ 5Å for the first two lines, $\sim$ 13Å for the middle one and $\sim$ 11Å for the

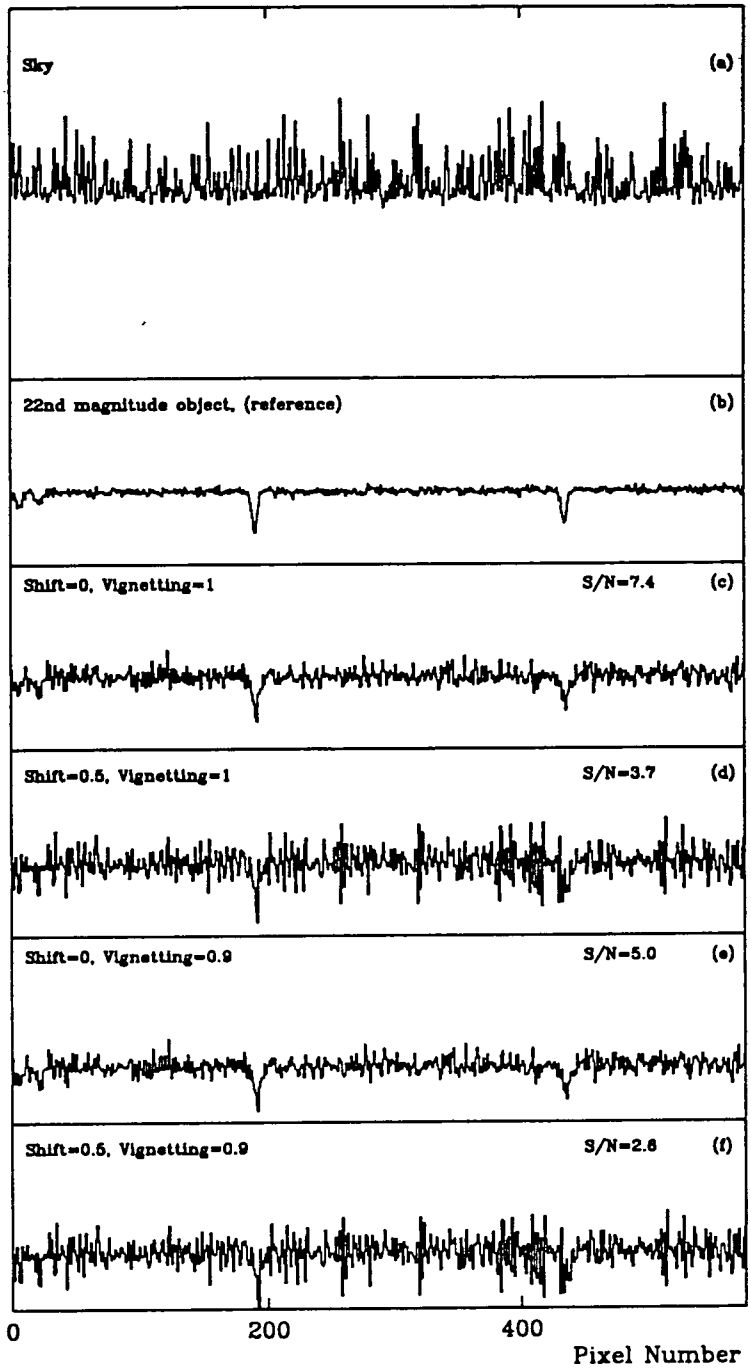

Figure 2.8. Computer simulated spectra. a) Sky. b) 22nd magnitude object without sky. c) – f) Results after subtraction for different values of the parameters Shift and Vignetting.

last one. The following spectra are the results after sky subtraction for different values of the program parameters *Shift* and *Vignetting*.

In figure 2.8 (c), *Shift=0* and *Vignetting=1*, which means that the sky + object spectrum and the sky spectrum are perfectly aligned in the wavelength direction and that the instrumental response of the two channels is correctly taken as being the same. As expected this spectrum is more noisy than the previous one, because of the process of subtracting off the sky background This is the optimum case and is the sort of result routinely obtained with slit spectroscopy.

If the sky spectrum is shifted half a pixel relative to the sky + object one (*Shift=0.5*) the noise increases even with *Vignetting=1* as shown in the next spectrum, figure 2.8 (d). Notice that some features are lost, for instance the weak lines near the left edge, demonstrating that correct alignment of the fibres in the wavelength direction is essential at faint levels. The effect of shifting the sky spectrum twice was also investigated: the first shift simulating the instrumental shift and the second equal and opposite shift to simulate the data reduction process. Although the spectra are correctly aligned when they are subtracted the resampling involved still introduces errors and we find that the resulting S/N ratio is not much better than that obtained using the instrumental shift alone as in the examples presented here. Figure 2.8 (e) shows what happens if we set *Shift=0* but set *Vignetting=0.9, i.e.* we deliberately make the false assumption that the relative fibre responses differ by 10%. Finally, figure 2.8 (d), shows the result when *Shift=0.5* and *Vignetting=0.9*.

The S/N ratio of a spectral line is calculated to quantify the effect of the systematic errors on the sky subtraction. The signal is taken to be a strong absorption line whose depth is 80% of the continuum level and the noise as the standard deviation of the resultant spectrum after subtraction. From the best case, figure 2.8 (c), to the worst case,

figure 2.8 (f) the S/N ratio changes from 7.4 to 2.6, *i.e.* decreases by a factor of ~3, which shows how sensitive the S/N ratio is to shifts and to poorly determined fibre response variations.

These simulations have been run many times to show how the S/N ratio varies as a function of integration time for different magnitudes and different values of *Shift* and *Vignetting* and the results are shown in figure 2.9 (a) – (f). Figure 2.9 (e) and (f) show that when the systematic errors are bad it can take up to 7 times longer to reach a given S/N ratio compared to the case where there are no systematic errors. This is equivalent to using a 1.5m telescope instead of a 4m telescope.

2.10 Conclusions

There is not a simple answer to the problem of sky subtraction with fibres. Observationally, the strategy depends of the wavelength passband of interest. In the blue region of the spectrum the standard method of dedicating a subset of fibres can provide reasonably accurate sky subtraction but it is generally incapable of achieving the faintness limits of multislit spectroscopy. In the red where the sky spectrum is highly structured a beam switching technique is far more likely to be successful. Very faint object spectroscopy with fibres must be possible but there is likely to be a trade-off between multiplex advantage and limiting magnitude. The extent of this trade-off is as yet unknown.

Instrumentally, there are many potentially useful techniques which could be employed to achieve good sky subtraction at faint levels. Improving the existing techniques by using fibres manufactured to the highest standards will minimise systematic differences. However, it is not the quality or the stability of the fibres that leads to poor results but

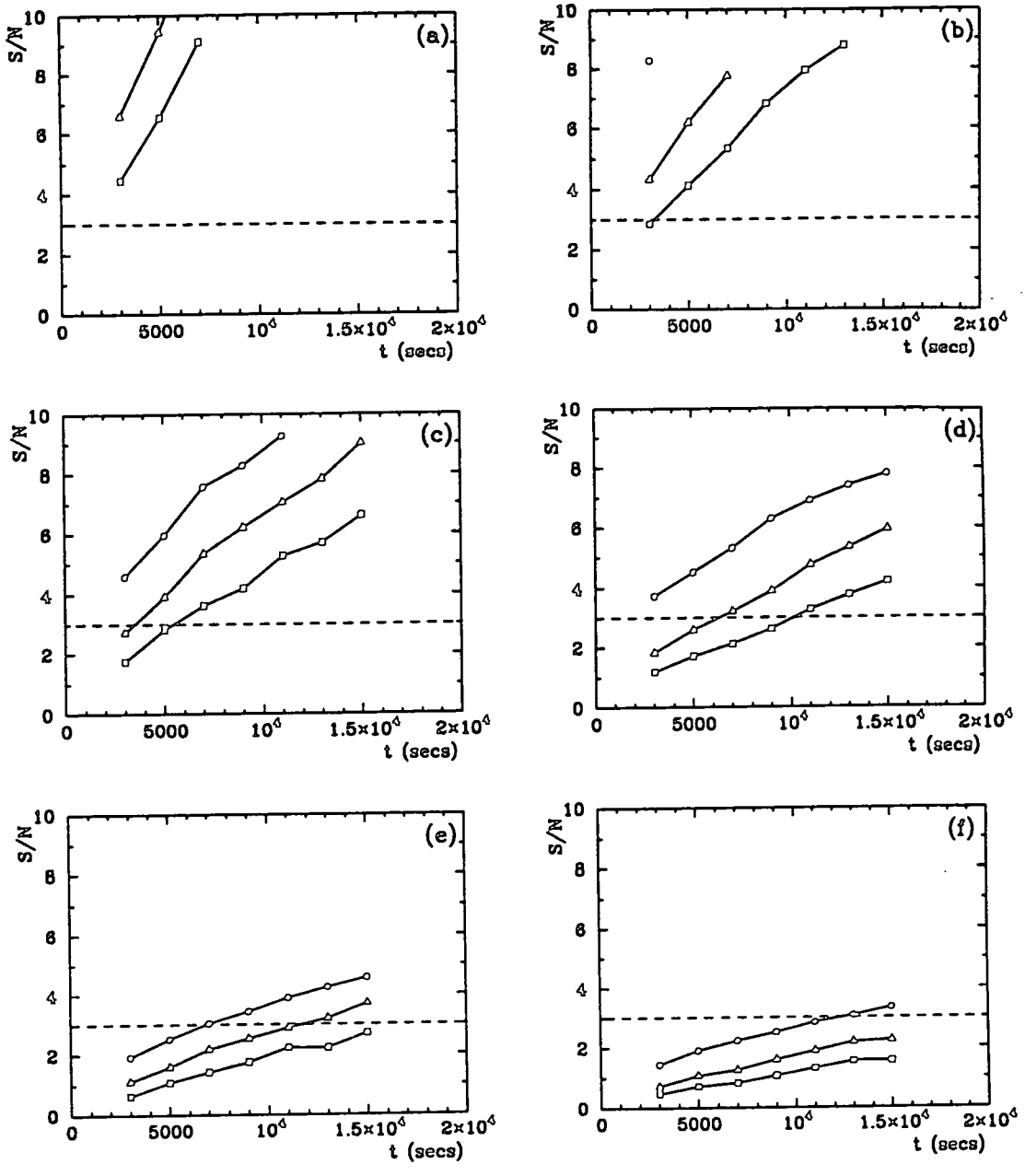

Figure 2.9. Computer simulated data, S/N ratio as a function of the integration time, each curve corresponds to a value of the parameter shift in pixels. The solid circles denote Shift=0, the solid triangles denote Shift=0.3 and the solid squares denote Shift=0.5. a) Magnitude=21, Vignetting=1. b) Magnitude=21, Vignetting=0.9. c) Magnitude=22, Vignetting=1. d) Magnitude=22, Vignetting=0.9. e) Magnitude=23, Vignetting=1. f) Magnitude=23, Vignetting=0.9.

the lack of adjacency at the detector which increases the systematic differences between the sky + object spectrum and the sky spectrum subtracted from it.

Progress has been made to optimise the performance of multiobject spectrographs. For example the WYFOSS spectrograph has been designed to have a wide field to avoid vignetting of the fibres near the edge of the slit. Also the use of fibres at a fast input f-ratio such as f/2.8 will minimise the losses due to FRD effects.

It is very important to identify the real limitations to the precision of sky subtraction and also to determine to what extent special observing and data reduction techniques are required. An experimental approach to this problem will be very useful. The entire observing apparatus can be simulated in the laboratory to investigate the different sky subtraction techniques under controlled conditions and determine their deficiencies. For example, the effects of systematic errors such as poor wavelength calibration can be analysed directly. This approach will allow us to develop better fibre calibration procedures. The computer simulations can also be extended by using high signal to noise observational data as the starting point and simulating other effects such as background light from scattering. The reanalysis of some real fibre data may help to improve data reduction techniques.

To achieve accurate sky subtraction, the general recommendations to be drawn from the discussion in this chapter are the following:

o Use the beamswitching technique. This is a proven technique for good sky subtraction but it is not ideal (see §2.6).

o Reduce the amount of scattered light in the spectrograph.

o Dedicate more detector pixels to monitoring the scattered light along the slit.

• Improve the methods for determining the vignetting function.

• Manufacture and install the fibres bundle to very high standards to make its optical performance as repeatable as possible.

• Ensure that the data reduction software properly handles scattered light and uses the most accurate resampling algorithms.

• The use of a "global" sky spectrum which is scaled and subtracted off each object spectrum should be avoided if possible since it will be sampled in a way that is different to all the individual object spectra. A possible alternative is to select an optimum set of sky fibres for each object fibre to improve adjacency and minimise sampling errors.

Sky subtraction with fibres is much more complicated than in the multislit case and has been limited by the systematic errors discussed above. Nevertheless, the larger multiplex gain and the ability to utilize large fields and high spectral resolutions make it vitally important that we improve the current techniques.

3 OPTICAL FIBRE PROPERTIES

3.1 Introduction

The propagation of light in an ideal fibre has been discussed by several authors (*e.g.* Allan 1973, Midwinter 1979 & Keck 1981). Basically, the wave equation for a homogeneous medium is solved for a structure of cylindrical symmetry applying the boundary conditions at the core-cladding interface. A detailed analysis of the solutions is beyond the scope of this chapter. Nevertheless to understand the most important features the simpler case of propagation of light in a planar waveguide is adequate.

In the real case of non-ideal fibres some perturbations will exist as a result of the processes by which it is fabricated or more likely as a result of its environment. The mathematical formalism to describe these perturbations becomes even more complicated and in many cases it is not possible to find an analytical solution, unless some approximations are applied. In the case of one of the perturbations responsible for focal ratio degradation, namely microbends, Gloge (1972) has developed a theoretical model to describe the distribution of optical power in a fibre as a function of the fibre length and of the axial angle of incidence.

A new method for measuring the degree of focal ratio degradation of an optical fibre has been developed based on Gloge's model and the solution proposed by Gambling *et al.* (1975). The principle is to characterise the fibre FRD performance by a single parameter which can be used to accurately model the fibre's performance in most astronomical applications. Computer programs have been written to model the far-field output of an optical fibre for various input beams including collimated beams and uncollimated pencil beams tilted with respect to the fibre's optical axis. This theory characterises the FRD with a single parameter D and successfully reproduces experimental results.

In section 3.2 a summary of the propagation of light in a planar dielectric waveguide is given. In section 3.3 the properties of multimode step index fibres are described. The optical power loss mechanisms are discussed in sections 3.4 to 3.6. Section 3.7 is devoted to microbending-induced FRD. Firstly, the theory behind the model is described and secondly, the modelling software and some examples are given. The examples illustrate the limitations imposed by the presence of FRD. Further mechanisms that induce FRD are also discussed. Finally, section 3.8 presents the conclusions.

3.2 Planar dielectric waveguides

A full mathematical treatment of propagation of light down dielectric waveguides requires the solution of Maxwell's equations with the appropriate boundary conditions (see Midwinter 1979). Nevertheless, insight may be gained by a consideration of the rather simpler problem of light ray propagation within a planar waveguide.

When an electromagnetic wave is incident upon the boundary between two dielectric media whose refractive indices are n_1 and n_2, with $n_1 > n_2$, then in general part of

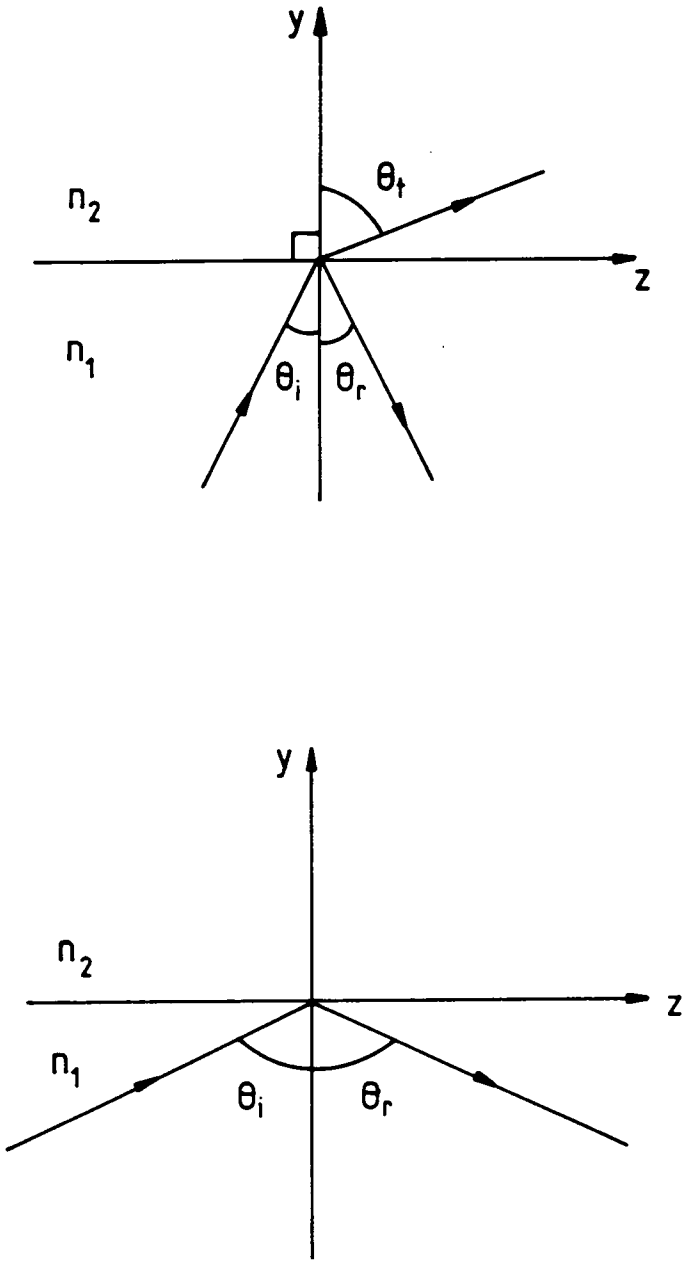

Figure 3.1. a) When an electromagnetic wave is incident upon the boundary between two dielectric media whose refractive indices are n_1 and n_2, with $n_1 > n_2$, then in general a portion of the wave is reflected and the remainder is transmitted. b) Total internal reflection is produced when $\theta_i > \theta_c$.

the wave is reflected and the remainder is transmitted. Assume that the wave is incident on the interface at an angle θ_i to the normal and that the reflected and transmitted waves are at angles θ_r and θ_t respectively, as shown in figure 3.1, where the coordinates are defined so that the direction of incidence lies in the y-z plane with the surface forming the x-z plane. The solutions for the amplitude and propagation characteristics of waves in such a structure are found by solving the wave equation in a homogeneous medium to find suitable waves in the two bounding media. Boundary conditions are applied to link them together. Maxwell's equations require that both the tangential components of $\mathbb{E}$ and $\mathbb{H}$ and the normal components of $\mathbb{D}= (\epsilon\epsilon_0\mathbb{E})$ and $\mathbb{B}= (\mu\mu_0\mathbb{H})$ are continuous across the boundary and this determines their relative amplitude and other relations such as

$$\frac{\sin\theta_i}{\sin\theta_t} = \frac{n_2}{n_1} \tag{3.1}$$

which is Snell's law of refraction. There is an angle of incidence (the critical angle θ_c) at which the reflected amplitude equals the incident wave amplitude. This corresponds to the condition

$$\sin\theta_c = \sin\theta_i = (n_2/n_1) \tag{3.2}$$

For angles of incidence greater than θ_c the reflected wave undergoes a change of phase but its amplitude remains constant. The phase change depends upon both the angle of incidence and the polarization —transverse electric (TE) or transverse magnetic (TM).

Consider now the simplest form of optical waveguide one which consists of a slab of a dielectric of thickness d and refractive index n_1 between two semi-infinite regions both of refractive index n_2, as shown in figure 3.2 (a). Assuming $n_1 > n_2$ and $\theta_i > \theta_c$ then total internal reflection occurs at both interfaces. An incident plane wave gives rise to a reflected

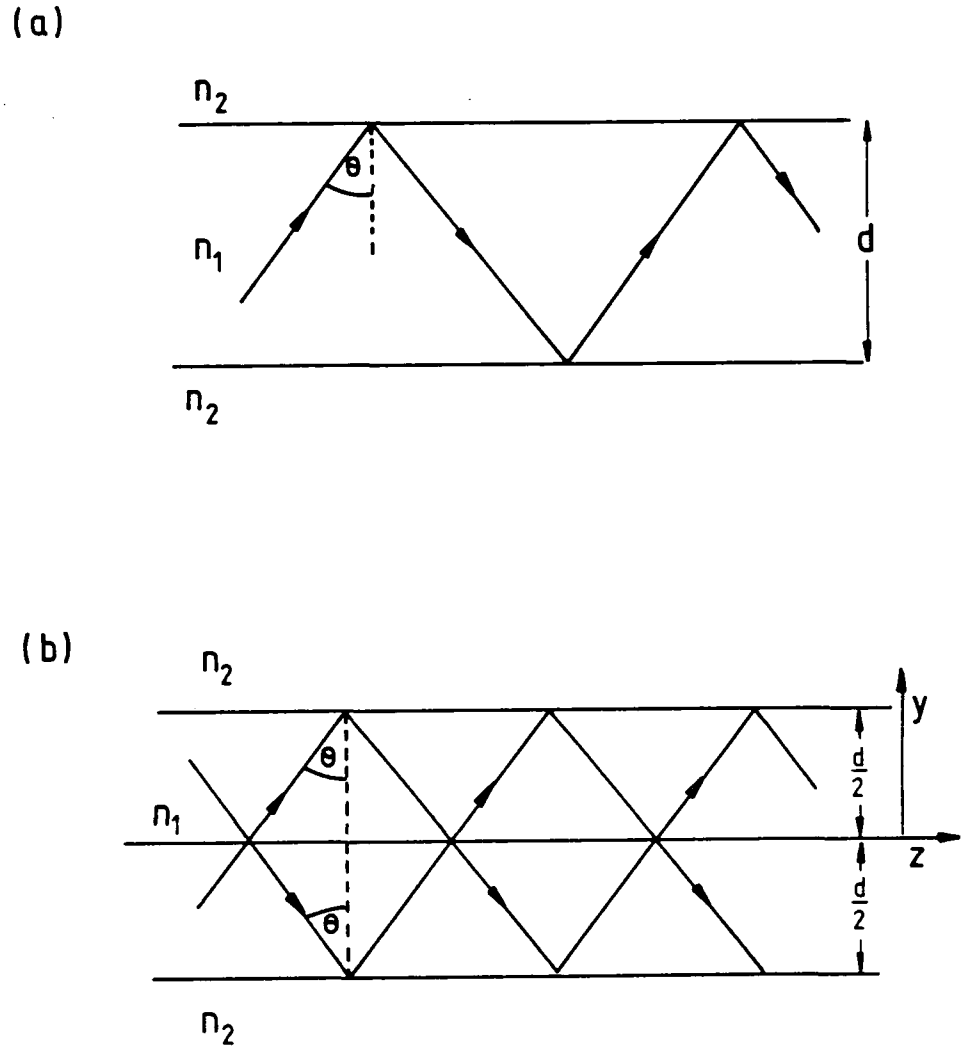

Figure 3.2. a) Diagram of a planar dielectric waveguide of thickness d and refractive index n_1 between two semi-infinite regions both of index of refraction n_2. Total internal reflection results when the angle of incidence at the interface θ is greater than the critical angle θ_c. The wave is guided along the structure in a zigzag path by successive reflections. b) Two waves are shown traveling down a guide with the same angle of incidence θ.

wave, which in turn is reflected again at the second interface $y = d/2$. Consequently the wave is guided along the structure in a zigzag path by successive reflections.

Reflection at a single interface couples the amplitudes and phases of all the waves involved at the interface, so that, given one the others are totally specified. In a guide the solutions exist only for certain values of the wavevector $\overline{k}$ ($|k| = 2\pi/\lambda$) which are called modes of propagation.

In the general case the spatial variation of the electric field $\overline{E}(\overline{r})$ can be written as

$$\overline{E}(\overline{r}) = \int \overline{E}(\overline{k}) \exp(-i\,\overline{k}\cdot\overline{r})\; d^3k \tag{3.3}$$

In the two dimensional case of monochromatic light ($|k| = k_0$), angle of incidence θ and propagation forwards, as shown in figure 3.2 (b), $\overline{E}(\,\overline{r})$ is reduced to

$$\overline{E}(\overline{r}) = \overline{E}_{up}\;\exp(-i\,\overline{k}_{up}\cdot\overline{r}) + \overline{E}_{down}\;\exp(-i\,\overline{k}_{down}\cdot\overline{r})$$

where:

$$\overline{k}_{up} = k_0(\hat{y}\;\cos\theta + \hat{z}\;\sin\theta)$$

$$\overline{k}_{down} = k_0(-\hat{y}\;\cos\theta + \hat{z}\;\sin\theta)$$

$$\overline{r} = \hat{y}\;y + \hat{z}\;z$$

$\hat{y}$ and $\hat{z}$ are the unitary vectors along the y-axis and the z-axis respectively. Thus,

$$\overline{E} = \exp(-ik_0 z\sin\theta)\left[\overline{E}_{up}\;\exp(-ik_0 y\cos\theta) + \overline{E}_{down}\;\exp(ik_0 y\cos\theta)\right] \tag{3.4}$$

where the unknowns are the vectors $\overline{E}_{up}$ and $\overline{E}_{down}$ representing amplitude and direction of the waves that cross the guide at $y = d/2$ and $y = -d/2$ respectively. At the interface there is a phase change ϕ on reflection and the $\overline{E}_{up}$ component becomes $\overline{E}_{down}$ and viceversa, *i.e.*

$$at \quad y = \frac{d}{2} \qquad E_{up} \rightarrow E_{down} \ \exp(-i\ \phi)$$

$$at \quad y = \frac{-d}{2} \qquad E_{down} \rightarrow E_{up} \ \exp(-i\ \phi)$$

More exactly, we have a system of equations: at $y = d/2$

$$\overline{E}_{up} \ \exp(-i\ k_0\ d/2\ \cos\theta) = \overline{E}_{down} \ \exp(i\ k_0\ d/2\ \cos\theta)\ \exp(-i\ \phi) \tag{3.5}$$

while at $y = -d/2$

$$\overline{E}_{down} \ \exp(-i\ k_0\ d/2\ \cos\theta) = \overline{E}_{up} \ \exp(i\ k_0\ d/2\ \cos\theta)\ \exp(-i\ \phi) \tag{3.6}$$

Substituting $\overline{E}_{up}$ from equation 3.5 in equation 3.6, we have

$$\overline{E}_{down} = \overline{E}_{down} \ \exp[2i\ (k_0\ d\ \cos\theta - \phi)] \tag{3.7}$$

There are two solutions to these equations, either

$$i) \qquad \overline{E}_{down} = \overline{E}_{up} = 0 \qquad for \quad any \quad k$$

or

$$ii) \quad \overline{E}_{down} = \overline{E}_{up} \ \exp(-i \ m \ \pi) \tag{3.8}$$

for

$$k_0 \ d \ \cos\theta - \phi = m \ \pi \tag{3.9}$$

where m is an integer. Substituting $k_0 = 2 \ \pi n_1/\lambda_0$ leads to the result

$$m = \frac{2 \ n_1 \ d \ \cos\theta}{\lambda_0} - \frac{\phi}{\pi} \tag{3.10}$$

Now substituting equation 3.10 in equation 3.4, we obtain

$$\overline{E} = \overline{E}_{up} \exp(-ik_0 z \sin\theta) \exp(-im\frac{\pi}{2}) \left[\exp -i(k_0 y \cos\theta - m\frac{\pi}{2}) + \exp i(k_0 y \cos\theta - m\frac{\pi}{2}) \right]$$

$$\overline{E} = \overline{E}_{up} \exp(-ik_0 z \sin\theta) \exp(-im\pi/2) \left[2\cos(k_0 y \cos\theta - m\pi/2) \right]$$

using equality 3.9 and the fact that $\cos x = \cos(-x)$ we can express the above result as

$$\overline{E} = 2\overline{E}_{up} \exp(-ik_0 z \sin\theta) \exp(-im\pi/2) \cos\left[\frac{m\pi}{2} - (\pi m + \phi)\frac{y}{d} \right]$$

or

$$\overline{E} = 2\overline{A}_0 \cos\left[\frac{m\pi}{2} - (\pi m + \phi)\frac{y}{d} \right] \tag{3.11}$$

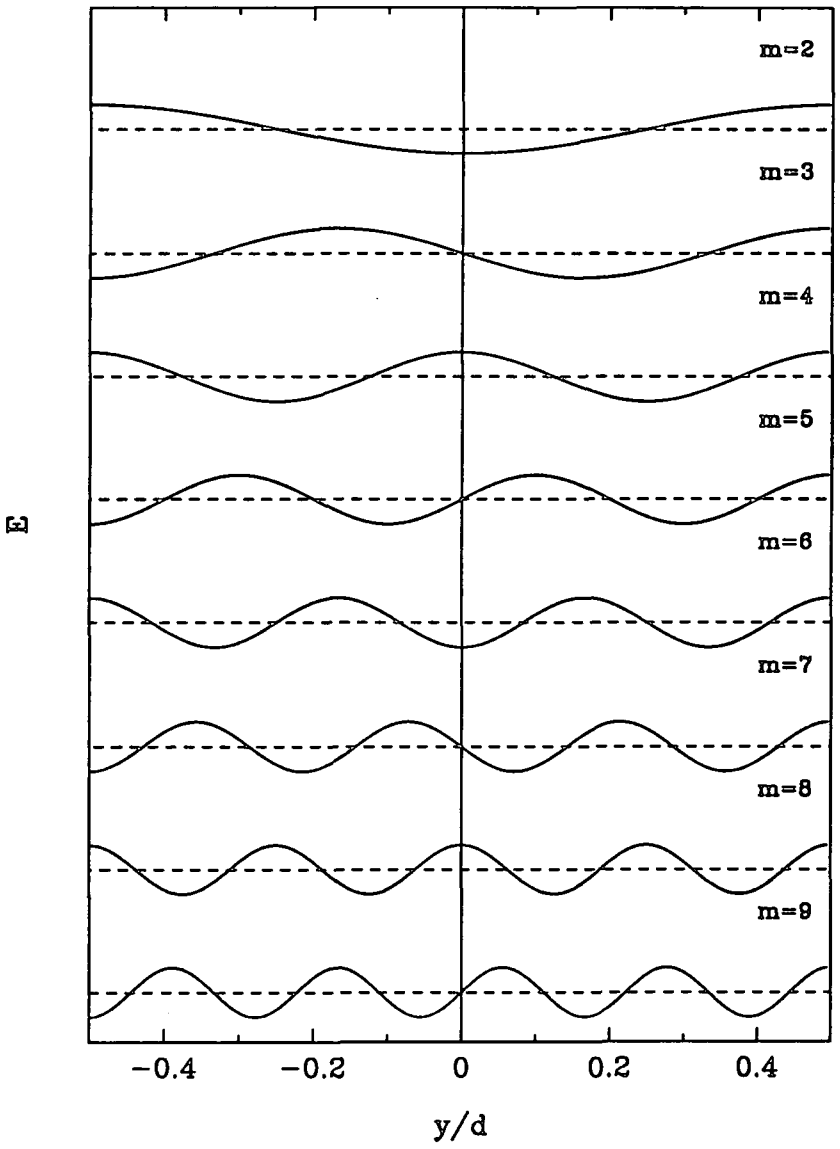

Figure 3.3. The variation of the electric field $\overline{E}$ across the guide, according to equation 3.11, for different values of m as indicated.

Each value of m is associated with a distinct wave pattern or *mode*. The variation of the electric field across the guide given by equation 3.11 is shown in figure 3.3 for different values of m. The mode is characterised by the mode number which is equal to the number of zeros of the intensity distribution in the transverse direction. At the centre of the guide (y=0) this will have the value $\pm 2A_0$ or zero depending of whether m is even or odd. At the guide edges (y=d/2) the amplitude is $2A_0 \cos \phi/2$.

The allowed values of θ (θ_m) are determined by the value of m given by equation 3.10. To maintain total internal reflection $\sin \theta_m > n_2/n_1$ and consequently

$$m \leq \frac{2dn_1}{\lambda_0}\left[1-(n_2/n_1)^2\right]^{1/2} - \frac{\phi}{\pi}$$

or

$$m \leq \frac{V}{\pi} - \frac{\phi}{\pi} \tag{3.12}$$

where

$$V = \frac{2\pi dn_1}{\lambda_0}\left[1-(n_2/n_1)^2\right]^{1/2} = \frac{2\pi d}{\lambda_0}(n_1^2 - n_2^2)^{1/2} \tag{3.13}$$

V is known as the normalized film thickness. In any particular situation the maximum value that m can take is given by equation 3.12. If V< ϕ then no mode whatsoever can be propagated. However, for any value of V it is always possible to find an angle θ such that the corresponding value of ϕ is less than V and consequently at least one mode can always be propagated.

3.3 Step index fibres

Consider the simple step index waveguide which, as shown in axial cross section in figure 3.4 (a) consists of a uniform core region of diameter d and index n_1 surrounded by a cladding of index n_2. Two types of rays exist in such an structure, meridional rays, which pass through the guide axis and skew rays which do not. A typical meridional ray is shown in the figure. The angle θ_0 that the ray in the external medium (usually air) makes with the normal to the end of the guide is related to the internal angle θ by Snell's law, so

$$\frac{\sin\theta_0}{\sin(\pi/2-\theta)} = \frac{n_1}{n_0} \tag{3.14}$$

hence

$$\sin\theta_0 = \frac{n_1}{n_0}\cos\theta \tag{3.15}$$

The maximum value that θ_0 can take θ_{0max} is determined by the minimum value that θ can take which is of course the critical angle θ_c. Therefore, for $n_0 = 1$

$$\sin\theta_{0max} = n_1(1-\sin^2\theta_c)^{1/2} = (n_1^2 - n_2^2)^{1/2} \tag{3.16}$$

The numerical aperture (NA) of the fibre is defined as

$$NA = (n_1^2 - n_2^2)^{1/2} = \sin\theta_{0max} \tag{3.17}$$

θ_{0max} is known as the fibre acceptance angle. The numerical aperture can be taken as a measure of the capacity of the guide to transmit light power. Assuming a waveguide in

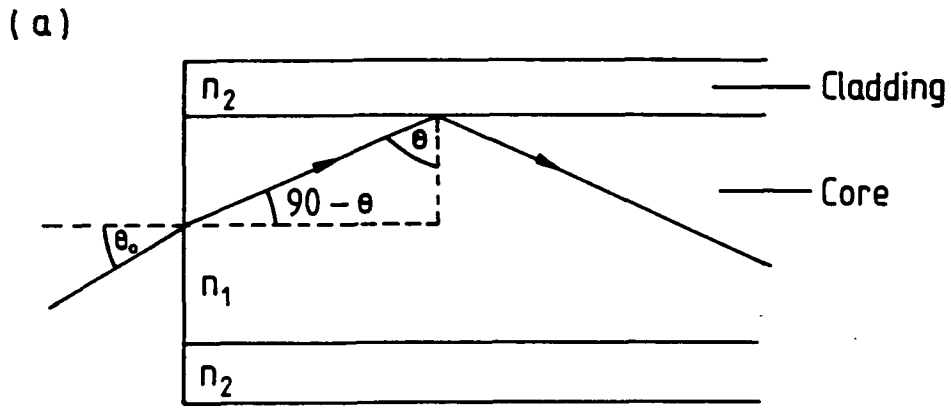

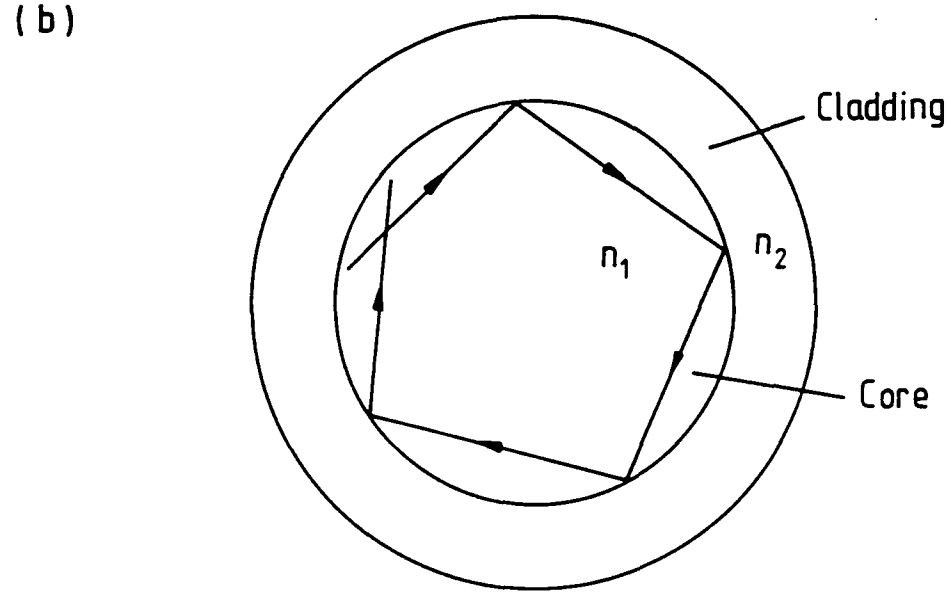

Figure 3.4. a) Path of a meridional ray as it enters a circular step index waveguide. The ray is incident on the end of the fibre at an angle θ_0 to the normal. Inside the fibre the ray makes an angle θ with the normal to the fibre axis. b) Path of a skew ray in a circular step index fibre and its projection normal to the fibre axis

air with $n_1 = 1.457$ and $n_2 = 1.440$, then NA=0.22 and the maximum angle ray accepted by the waveguide is $\theta_0 = 12.7°$ which corresponds to an f-ratio of 2.22. These are typical values for the all-silica fibres used in astronomical applications.

The meridional rays discussed so far give rise to modes which, as for the planar waveguide may be designated transverse electric (TE) and transverse magnetic (TM). Two integers l and m are required to completely specify the modes, essentially because the guide is bounded in two dimensions. Thus we refer to TE_{lm} and TM_{lm} modes.

Skew rays describe angular helices as they propagate along the fibre. Figure 3.4 (b) shows the projected path of such a ray. Because of the angles involved, components of both **E** and **H** can be transverse to the fibre axis. Consequently the modes originating from skew rays are designated as either HE_{lm} or EH_{lm} depending of whether their magnetic or electric character dominates. In most practical waveguides the refractive index of core and cladding differ from each other by only a few per cent and in this case it may be shown (Midwinter 1979) that the full set of modes can be approximated by a single set called linearly polarized (LP_{lm}) modes. The number of modes that can propagated in a fibre can be related to a parameter V

$$V = \frac{\pi d}{\lambda_0} NA \tag{3.18}$$

which is very similar to that used for planar waveguides defined by equation 3.13. The number of modes N the guide can support, couple to and radiate into is given approximately (Wilson 1983) by

$$N \simeq \frac{V^2}{2} \tag{3.19}$$

These relations give a useful guide to the number of modes carried by a multimode guide. For example, in a 200μm core diameter fibre with NA=0.22 and $\lambda_0 = 6000\text{Å}$, the number of modes is $N \sim 27000$.

It should be emphasized that the arguments followed in this section have been in terms of geometrical optics and while it is accurate enough to predict the main properties of guides a full understanding of the propagation of light down a waveguide requires finding the appropriate solutions to Maxwell's equations.

3.4 Attenuation

The optical attenuation or power losses which occur as a light beam passes through a transparent medium such as a fibre are due to a variety of mechanisms and are a function of wavelength. Power losses in optical fibres are usually expressed in terms of an attenuation coefficient (α) measured in decibels (dB) per unit length, normally 1km. The attenuation coefficient is related to the ratio of the input P_i to the output P_0 powers and the fibre length L (in km) via the expression

$$\frac{P_o}{P_i} = 10^{-(\alpha L/10)} \tag{3.20}$$

The attenuation coefficient described by equation 3.20 is a property of the optical medium itself and does not incorporate losses due to partial reflection of light at the input end faces.

The transmission losses within a fibre are due to absorption and scattering. Both sources of attenuation are the result of a variety of intrinsic and extrinsic factors. The

theoretical total intrinsic attenuation coefficient α_i has the form, according to Drexhage (1990),

$$\alpha_i = A \exp(a/\lambda) + B/\lambda^4 + C \exp(-c\lambda) \tag{3.21}$$

where a, A, B, c and C are material constants and λ is the wavelength. The first term represents the losses due to ultraviolet or electronic absorption, the second term represents those due to Rayleigh scattering and the third term represents the losses due to multiphonon absorption.

At short wavelengths optical absorption occurs when the energy of a photon causes an electron in the material to jump from the valence to the conduction band. The details of this electronic absorption in crystal and glasses are not well understood but experimental data for many materials show that the attenuation caused by it decreases exponentially with wavelength in accordance with the form of the first term in equation 3.21 (Drexhage 1990). These losses are negligible beyond about 1μm.

In glass, Rayleigh scattering can arise from two separate effects, density and composition fluctuations. All transparent materials scatter light as a result of thermal fluctuations of the constituent atoms that are frozen in during solidification. These cause changes in density and hence index variations. The physical scale of the irregularities is of the order of one tenth wavelength or less, so that each irregularity acts as a point source for scattered radiation. This mechanism is an important source of opacity shortward of about 750nm and usually dominates in the region about 500nm–700nm. Rayleigh scattering is important since it represents the fundamental limit to attenuation in waveguides.

At long wavelengths the transparency of an optical material is limited by the existence of an infrared vibrational edge. The individual constituents of a glass are bonded

together chemically. Thermal energy maintains them in a constant state of random motion, so that any particular bond, say an SiO bond in glass, is continually vibrating. Each bond oscillates at a characteristic frequency and at that frequency an absorption line is seen. Evidence suggests at present that these mechanisms becomes serious only beyond about 2.5μm wavelength. A large number of vibrational modes in addition to the fundamental can occur. The atoms in the structure have many degrees of freedom and the bending motions of ionic pairs or other atomic structural groupings all absorb energy at wavelengths longer than that of the fundamental and in addition overtones of the fundamental itself give rise to a continuous absorption spectrum referred to as the infrared vibrational or multiphonon edge (Drexhage 1990).

Extrinsic factors include absorption due to impurities and contaminants in the material, such as hydroxyl (OH) groups and water. The OH ion is undesirable because overtones of the fundamental vibration give rise to absorption at 1.4μm, 970nm and 750nm and thus interfere with the transmission band of interest in glass. Other sources of extrinsic scattering are improper processing or fabrication such as non-uniformity in fibre radius core/cladding interface defects and localized deviations from the expected refractive index.

The total loss (scattering plus absorption) of two typical 15m length high quality fused silica fibres as a function of wavelength are shown in figure 3.5. For these fibres Rayleigh scattering and intrinsic absorption contribute roughly equally over the range 300nm–1μm (Angel 1977). The transmission characteristics of a fibre with substantial contamination by the hydroxyl radical (so-called 'wet' fibres) are shown in solid triangles. It has vibrational overtone absorption peaks near 750nm and 950nm. The transmission curve of a fibre with little hydroxyl content (so called 'dry' fibres) is shown in solid circles. It presents an absorption peak near 650nm and decreased transparency in the near ultraviolet. These curves were derived from data provided by Polymicro Technologies.

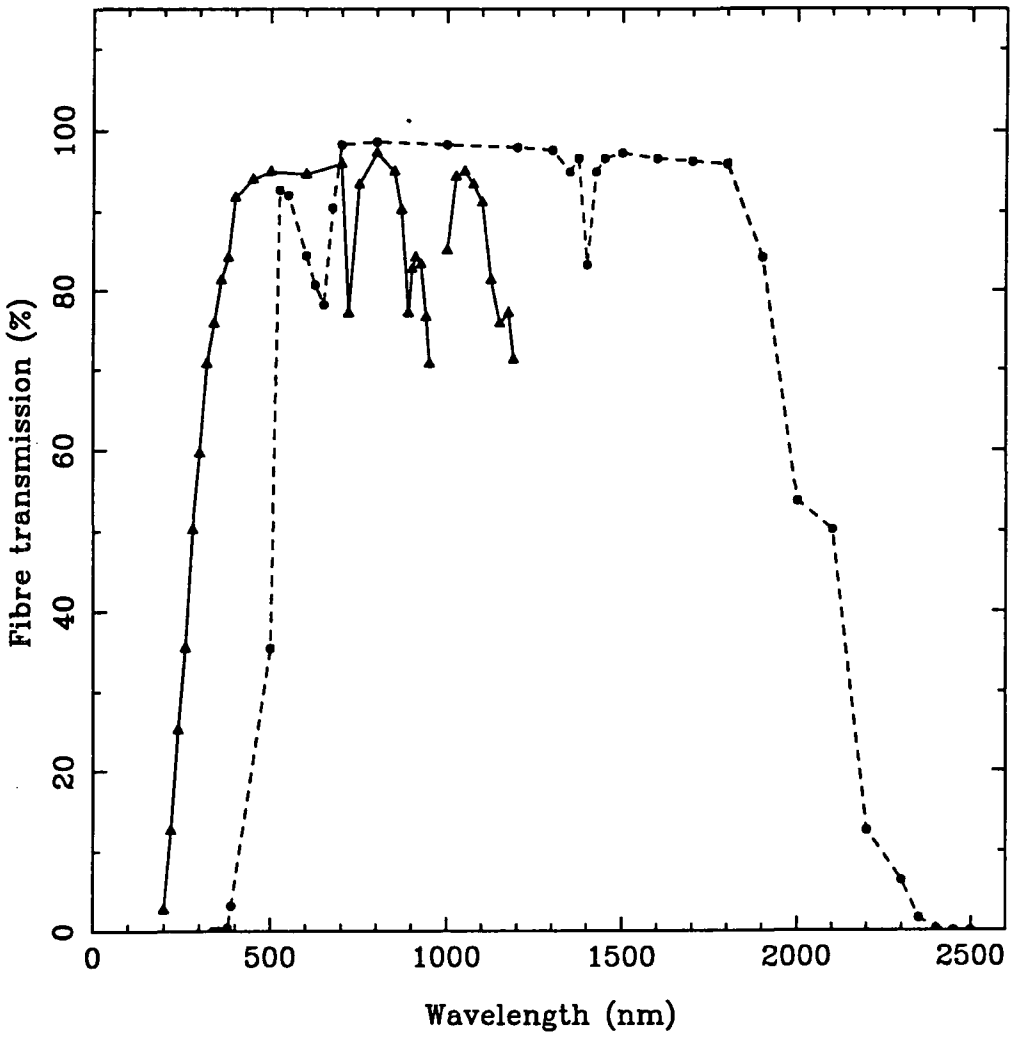

Figure 3.5. Transmission characteristics as a function of wavelength for 15m long fibres, with numerical aperture of 0.22. The curves were derived from data of Polymicro technologies. The properties of a fibre with a high OH^- content are shown in solid triangles (FV series). The transmission of a fibre with low OH^- is shown in solid circles (FL series).

3.5 Bending losses

Love and Winkler (1978) have studied the radiation loss due to bending for optical waveguides. The radiation is calculated by using geometric optics to determine the ray path within the core of the bent waveguide. The situation to be analysed is shown in figure 3.6 (a). A diffuse or Lambertian source illuminates the entire endface of an ideal multimode step-index waveguide. The guide is straight for a distance l beyond which a coil of uniform radius R is introduced. At this point if l is sufficiently large all the leaky rays have lost their power and essentially only bound rays remain in the core. Thus the ray power intensity distribution in the cross section XX' at the beginning of the coil may be taken as the Lambertian

$$I = I_0 \cos\theta \tag{3.22}$$

where I_0 is constant and $0 \leq \theta \leq \theta_c'$, where θ is the angle the ray path makes with the axis of the straight guide and $\theta_c' = \cos^{-1}(n_2/n_1)$ is the complement of the critical angle. The core and cladding indices are n_1 and n_2 respectively and the fibre diameter is 2ρ.

Every ray which is bound in the straight part of the guide now has an attenuation coefficient in the bent part of the guide. The overall attenuation of power around the bent guide is due to the attenuation of the power of the individual rays. In figure 3.6 (b) a typical ray path suffers successive reflections at points P and Q at the core-cladding interface. Regardless of whether the ray is meridional (*i.e.* in the plane defined by the centre of the bend C and the bent waveguide axis) or skew, the angular displacement $\Delta\phi_i$ around the bend from P to Q is considered. Assuming that the fraction of incident ray power lost upon reflection at Q is T_i, the power at ϕ can be calculated using a previous result by Snyder & Mitchell (1974) as follows:

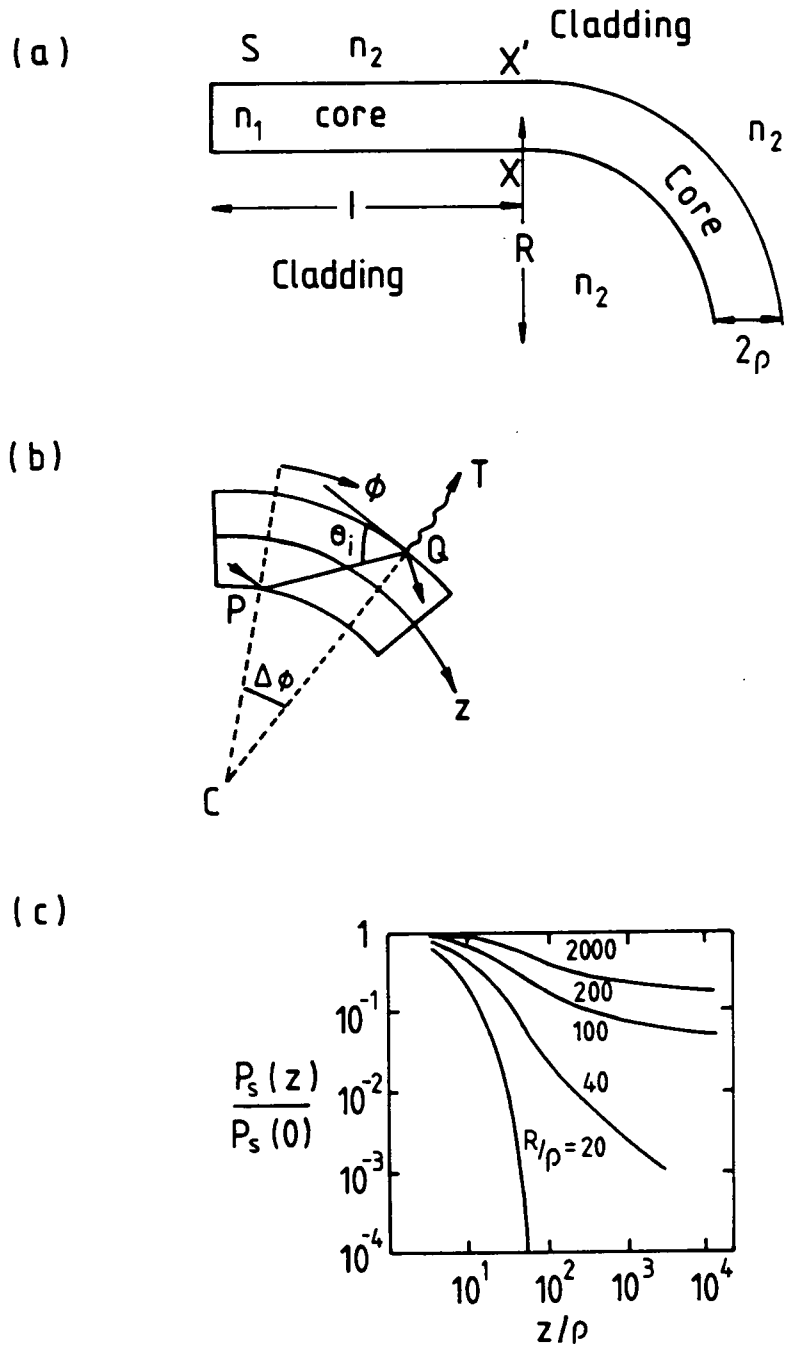

Figure 3.6. a) A diffuse source illuminates a multimode step index fibre. b) A typical ray in the core of a bent multimode guide is reflected from point P to point Q suffering transmission loss T at Q. c) The fraction of initial power remaining *vs* normalized distance z/ρ with z measured along the axis of the guide for various values of R/ρ where R is the radius of the bend. Results obtained by Love and Winkler (1978).

$$P(\phi) = P(0)\exp\Big(-\phi\sum_{i=1}^{N} T_i \Big/ \sum_{i=1}^{N}\Delta\phi\Big)$$

where P(0) is the power in the ray at the beginning of the bend and N is the number of reflections in angular displacement ϕ. Attenuation of the total power around the bend is obtained by summing this equation over all the paths of all the rays originating at $\phi = 0$ and using equation 3.22 to determine the initial power P(0) carried by each ray. Figure 3.6 (c) shows the fraction of initial power remaining along such a coiled fibre. The authors plot the normalized power ratio $P_s(z)/P_s(0)$ in terms of the distance z along the bent fibre, normalised to the half width z/ρ for various values of R/ρ, for a step profile fibre for which the parameter V given by equation 3.18 is equal to 50. It can be appreciated from the graph that for practical values of bending radius, when $R/\rho \geq 10^3$, bending losses are negligible.

3.6 Fresnel losses

The considerations of propagation of light through an optical fibre discussed so far do not include losses due to reflection at the fibres ends. Fresnel losses are incurred at the input and output faces of the fibre and are due to the difference in refractive index between the core glass and the immersion medium. For a large range of angles the equation for normal incidence is sufficiently accurate (Allan 1973) *i.e.*

$$R_f = \left(\frac{n_1 - n_0}{n_1 + n_0}\right)^2 \tag{3.23}$$

where n_1 and n_0 are the refractive indices of the core and immersion medium respectively and R_f is the fraction of the incident light which is reflected. For silica fibres in air ($n_0 = 1$)

a typical value for the transmission losses due to Fresnel reflections is about 8%. For any application the fibre end polishing should be extremely smooth to minimise scattering losses.

3.7 Focal ratio degradation

For astronomical applications the ability of the fibre to preserve the f-ratio of the input beam is as important as the spectral attenuation. In an ideal case light incident on a fibre at angle θ to the axis will emerge as a cone of angle θ to the axis. Thus if the fibre is illuminated by light from a lens or mirror at a certain focal ratio, the emergent light will be ideally at the same focal ratio. In practice the f-ratio of the output beam is always faster than that at the input end. The extent of this degradation is of practical importance in the optical design of a spectrograph because the maximum surface brightness that can be obtained at the detector will be reduced if beam divergence is increased on passage through the fibre.

Focal ratio degradation or beamspreading is in part due to the presence of numerous geometric defects in the fibre on a scale comparable to the fibre core diameter. These microbends scatter the axial angle of incidence of guided rays causing a decrease in the focal ratio of the guided beam. If sufficiently severe, such beamspreading can cause the NA of the fibre to be exceeded with consequent light loss from the beam.

From a modal point of view the presence of imperfections such as microbends due to external pressure and large scale deviations such as bends, causes a transfer of power from one mode to another so that the power distribution at the output of a fibre may be different from that at the input. This transfer of energy from one particular mode to

another is called mode coupling. Experimentally, mode coupling can be demonstrated, for example, by the observation of the far-field output intensity pattern when pressure is applied to the fibre. An increase in size and dispersion of the far-field pattern shows that mode conversion is induced and power is coupled to higher order modes. The same effect can be observed as a function of the fibre length (Gambling *et al.* 1975).

A theoretical treatment of this phenomenon leads in general to rather complex mathematics. Generally, Maxwell's equations must be solved for the mode fields subject to the specific distortion of the waveguide. According to Gloge (1972) coupling and delay differences among the modes of multimode fibres influence their transmission characteristics in a very complicated way. An approximation of the modes by a continuum leads to a description of the optical power of a fibre by one differential equation. The author showed that the far-field distribution represents a direct image of the modal power distribution. The power distribution is obtained directly from a power rate equation which considers the variation dP_m in the power P_m of the m^{th} mode along a guide increment dL. In the time invariant case, the variation dP_m is due to two mechanisms: *(i)* dissipation and loss (scattering) to the outside and *(ii)* coupling to other modes. With this basis and assuming that mode coupling takes place only between next neighbours, Gloge derived the following partial differential equation to describe the optical power P in a fibre of length L in terms of the angle of incidence θ

$$\frac{\partial P}{\partial L} = -A\theta^2 P + \frac{D}{\theta}\frac{\partial}{\partial \theta}\left(\theta \frac{\partial P}{\partial \theta}\right) \tag{3.24}$$

where A is an absorption coefficient and D is a parameter given by

$$D = \left(\frac{\lambda}{2d_f n}\right)^2 d_0, \tag{3.25}$$

λ is the wavelength of the light, d_f the fibre core diameter, n the index of refraction of the core and the constant d_0 is the coupling coefficient between modes. The first term in equation 3.24 corresponds to dissipation and loss scattering to the outside while the second term identifies next neighbour mode coupling as a diffusion process in the continuum. The coupling between modes is related to specific imperfections of the configuration or straightness of the fibre, *i.e.* to microbends. Therefore the constant d_0 can be identified as a diffusion constant that characterizes microbending.

Midwinter (1979) reports that equation 3.24 has been solved for a number of different situations with different objects in view. In particular, Gambling *et al.* (1975) have used the mode coupling diffusion equation to analyse the case of an excitation corresponding to an incident laser beam at an angle θ with respect to the fibre axis.

For astronomical applications we are interested in fibre performance in terms of the preservation of the f-ratio of an incident beam. Therefore, the particular solution given by Gambling *et al.* (1975) for his specific case has been generalised for a pencil beam incident on the input end of a fibre. The idea is to characterise the fibre by finding experimentally the value of the parameter d_0. This is done by studying the far-field pattern when a laser beam is incident on the input end of a fibre at an angle θ. Knowing this parameter the fibre beamspreading is predicted by the model developed. The results obtained by the model and by experiment are in good agreement and are discussed in detail in chapter 4 (§4.5). In the following section a description of the model is presented.

3.7.1 Focal ratio degradation model

The solution to equation 3.24 given by Gambling *et al.* (1975) for the case of a collimated input beam of angle of incidence θ_i is:

$$P(\theta) = \exp\left[-\left(\frac{\chi_i + \chi}{2}\right)\left(\frac{1+e^{(-bL)}}{1-e^{(-bL)}}\right)\right]\left(\frac{e^{(-bL/2)}}{1-e^{(-bL)}}\right) I_0\left(\frac{(4\chi_i\chi)^{1/2}e^{(-bL/2)}}{1-e^{(-bL)}}\right) \qquad (3.26)$$

where $\chi = (A/D)^{1/2}\theta^2$, $b = 4(AD)^{1/2}$ and I_0 is the modified Bessel function of zeroth order. For short fibres we can take $bL \ll 1$ and therefore approximate $\exp(-bL) \simeq 1 - bL$, from which

$$P(\theta) \simeq \frac{1}{bL}\exp\left(-\frac{\theta^2+\theta_i^2}{4DL}\right) I_0\left(\frac{\theta\theta_i}{2DL}\right) \qquad (3.27)$$

The two asymptotic forms of equation 3.27 are: a) if $\theta\theta_i/2DL \ll 1$, then

$$P(\theta) \propto \exp\left(-\frac{\theta^2+\theta_i^2}{4DL}\right) \qquad (3.28)$$

thus, for nearly axial collimated input beams the output beam will be a Gaussian centered on the optical axis, while b) if $\theta\theta_i/2DL \gg 1$, then

$$P(\theta) \propto \exp\left(-\frac{(\theta-\theta_i)^2}{4DL}\right) \qquad (3.29)$$

and so for collimated beams at high angle of incidence θ_i the output will be a ring of angular radius θ_i also of Gaussian cross section of width $\sigma = (2DL)^{1/2}$.

The approximated solution P as given by equation 3.27 has been evaluated for the case of a collimated input beam of angle of incidence θ_i and compared with experimental

data (§4.5.1). In agreement with the results of Heacox (1986), the prediction corresponds well with the laboratory results.

For a fibre of a given length L the parameter to be determined is D. If D is known, the case of a collimated input beam of angle of incidence θ_i can be generalised to the case of a beam of any aperture:

$$F(\theta) = \int_0^{2\pi} \int_0^{\pi} G(\theta', \phi')\, P(\theta, \theta')\, sin\theta'\, d\theta'\, d\phi' \tag{3.30}$$

where $sin\theta'\, d\theta'\, d\phi' = d\Omega$ is the differential of solid angle and G is a function that represents the input beam. In this case, the function $F(\theta)$ describes the cross section of the far-field distribution. There are particular cases that can be intuitively analysed. For instance, if the input beam is symmetrical with respect to the fibre axis the function G that describes it will be only a function of θ, $G = G(\theta')$.

Consider the case where the input beam is a uniform pencil of light of cone angle $\delta\theta$. Here G is a step function given by:

$$G(\theta') = \begin{cases} 1, & \text{if } \theta' \leq \delta\theta; \\ 0, & \text{if } \theta' > \delta\theta. \end{cases} \tag{3.31}$$

Because there is no ϕ dependence, the function F is simplified to

$$F(\theta) = 2\pi \int_0^{\delta\theta} P(\theta, \theta')\, sin\theta'\, d\theta' \tag{3.32}$$

Phenomena such as central obstructions can be modelled provided that the function G describes the central obstruction. For a tilted input beam, G will not be symmetrical

to the fibre axis and the only difference with respect to the former case is that there will be a dependence on ϕ', *i.e.* $G = G(\theta', \phi')$.

In principle any analytic function $G = G(\theta', \phi')$ can be integrated and F evaluated. Perhaps more interestingly is when G is a function obtained experimentally so that F can be evaluated numerically and compared with experimental results.

This formalism allows us to model different phenomena relevant to astronomical applications. Given the input function G and the experimentally determined parameter D, which is directly related to the diffusion constant d_0 that characterizes microbending, the function F can be predicted. The following section describes the modelling software that has been developed based on the above theory.

3.7.2 Modelling software

The software is divided in two main sections. The first is dedicated to the case of a collimated input beam and evaluates equation 3.27 given the fibre length L, the value of D and the angle of incidence θ_i. An example of the program output is shown in figure 3.7 (a); the profile was obtained for a fibre with $L = 2$m, $D = 0.7 \times 10^{-5}$ m^{-1} and an angle of incidence of the collimated input beam $\theta_i = 8.13°$.

The second part is devoted to the general case of an input beam of any aperture. The program evaluates the function F according to equation 3.30. The input parameters are: the fibre length L, the f-ratio of the input beam, the function G and the value of D. Figure 3.7 (b) shows the function F obtained with the same values used in the case of a collimated input beam for L, D and θ_i, which is the angle subtended by an f/3.5 beam. G was taken as a step function given by equation 3.31. The software also considers different cases such as a tilted input beam or an input beam with a central obstruction.

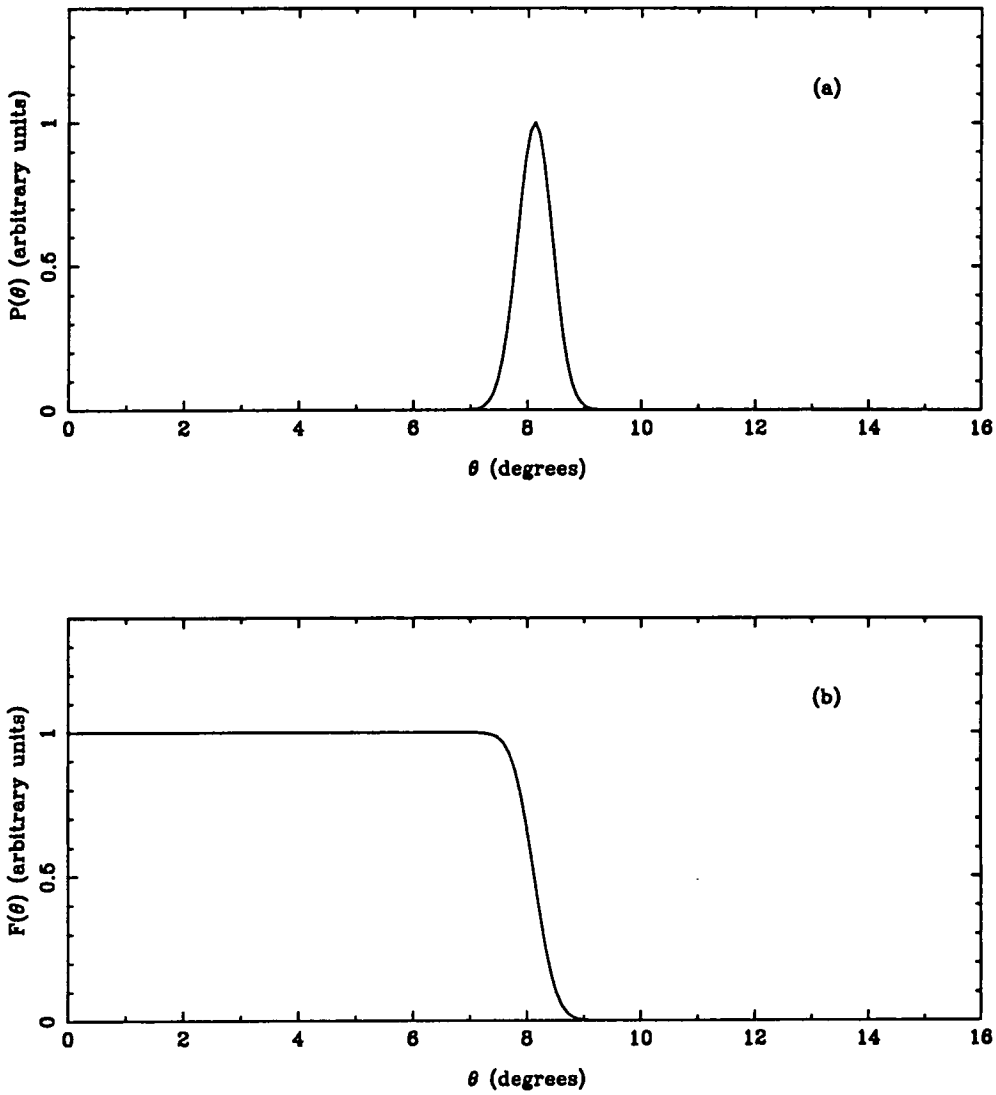

Figure 3.7. Optical power distribution for a 2 m long fibre with $D = 0.7 \times 10^{-5}$ m_{-1} according to the model. a) For a collimated input beam at an angle of incidence $\theta_i = 8.13°$. b) For an f/3.5 input beam, which corresponds to a pencil of light of cone angle $\theta_i = 8.13°$.

Once the modelling software was developed its predictions were tested experimentally. In section 4.5.1 the experiments conducted to verify the predictions for the case of a collimated input beam according to equation 3.27 are described. In section 4.5.2 the case of an uncollimated input beam is discussed. The predictions from the model reproduce the laboratory results very well. This good agreement between theory and experiment proves the validity of the approach presented. With this basis the formalism will be applied to illustrate the dependence of beamspreading on parameters such as the f-ratio of the input beam and the tilt of the input beam with respect to the fibre axis.

3.7.3 Examples

The FRD dependence on the input f-ratio has been extensively measured by different authors, for different types of fibres under different experimental conditions (*e.g.* Gray 1983, Powell 1983, Barden 1987 & Ramsey 1988). Each author chose the fibre and the experimental parameters according to his (hers) specific application. Furthermore, the problem becomes more complicated because the individual fibre performance depends on the preparation of the fibre ends. Due to the presence of so many parameters, the results reported in the literature represent to some extent particular cases. Therefore, the approach chosen for this section is to show in general terms the FRD dependence on some parameters according to the model.

Assume that G is a step function *i.e.* the fibre is uniformly illuminated and let $L = 15$m. The program evaluates the function F according to equation 3.32. For an input beam of a given f-ratio (f_{in}), the output profile is of the shape shown in figure 3.7 (b). The f-ratio of the output beam (f_{out}) is estimated from the angle θ for which the profile falls to zero. Figure 3.8 (a) presents a curve f_{in} *vs* f_{out} for different values of the parameter D. The values of D are physically realistic values which can be achieved experimentally. In

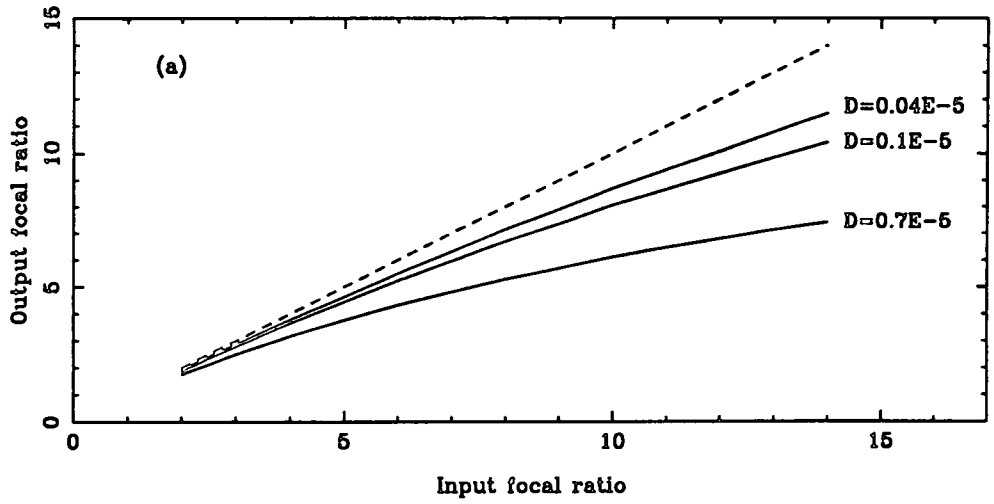

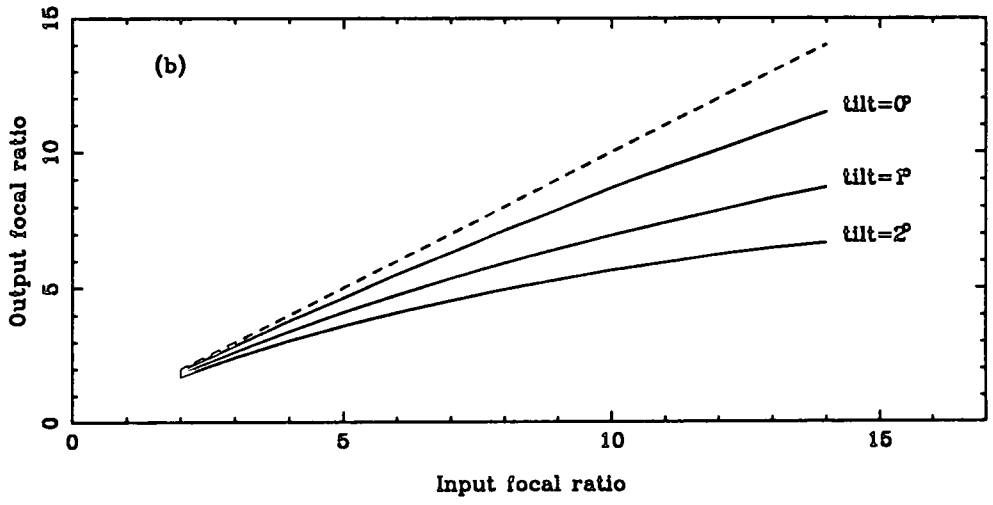

Figure 3.8. Focal ratio degradation curves predicted by the model for a fibre of length $L = 15$m, assuming a perfectly uniform illumination across the fibre. The dotted lines represent the ideal case of zero FRD. a) The solid curves correspond to different values of the parameter D as indicated. The curves are consistent with experimental results. Clearly the FRD is worse for slow input beam. b) The curves were obtained for $D = 0.04 \times 10^{-5}$ m^{-1}, assuming a tilt of the input beam with respect to the fibre axis as indicated. It can be appreciated that the FRD becomes more accentuated as the tilt angle increases.

particular, the value of $D = 0.04 \times 10^{-5}$ m^{-1} represents the case of a extremely good fibre, based on the results obtained by Barden (1987) as discussed in section 4.5.2. Considering any of the cases shown in the figure it can be seen that the FRD effect is more severe for slow input beams.

The alignment of the fibre with the incoming telescope beam is of critical importance, particularly for wide field systems where the angle the principal ray makes with the focal plane increases with field angle and can be large ($2° - 4°$) at the field edge. The effect of a tilt of the input beam with respect to the fibre axis can be visualized in figure 3.8 (b). The curves were obtained for L = 15m and $D = 0.04 \times 10^{-5}$ m^{-1}. The tilt angles are indicated. The results clearly show that even for an extremely good fibre the presence of a tilt degrades the fibre performance.

FRD also decreases the fibre's ability to transmit the central shadow of the telescope pupil. Consider the case of a very good fibre (like the one shown in figure 3.7) for which L = 2m and $D = 0.7 \times 10^{-5}$ m^{-1}. Let the input function G be a centrally obstructed f/3.5 uniform beam such as for the prime focus of the AAT. The function F obtained with these parameters is shown in figure 3.9 (a). Under the same conditions a poor fibre with $D = 15 \times 10^{-5}$ m^{-1} will have a profile shown in figure 3.9 (b).

From the previous discussion it is evident that FRD represents a loss for any astronomical application. It is therefore very important to understand the mechanisms responsible for this phenomenon.

3.7.4 Mechanisms that induce FRD

The losses due to FRD can be divided into two categories: *i)* those which are inherent in the fibre itself, such as microbends due to imperfections in the core-cladding interface

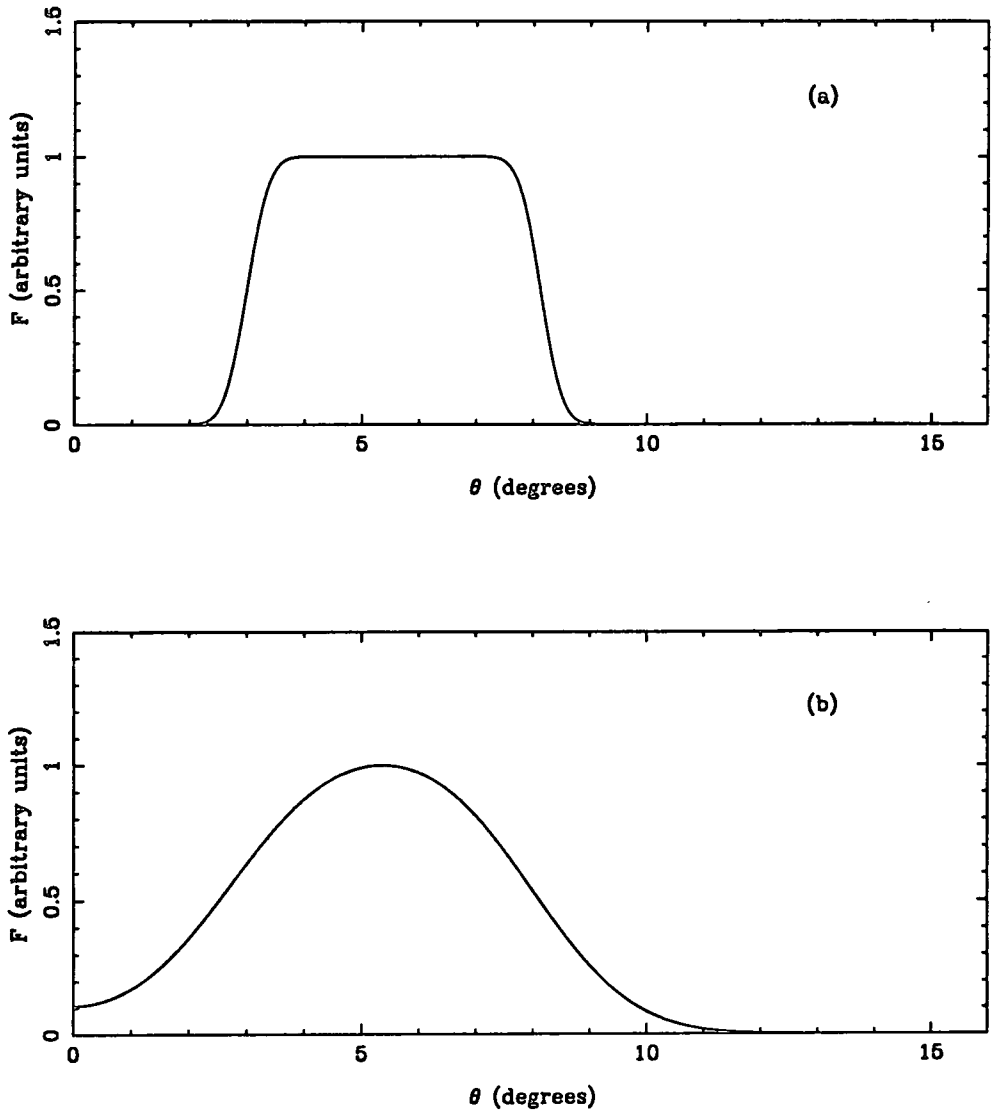

Figure 3.9. Profiles predicted by the model for a centrally obstructed input beam incident onto a fibre 2m long. a) Very good fibre with $D = 0.7 \times 10^{-5}$ m^{-1}. b) Poor fibre with $D = 15 \times 10^{-5}$ m^{-1}.

and *ii)* those which result from the distortion of the fibre such as further microbends and losses induced by the fibre end preparation. From the point of view of astronomical instrumentation the first category can only be minimised by carefully selection of fibre manufacturer whereas the second category can be minimised by careful design, manufacture and installation.

According to Heacox (1986), large mechanical deformation of the fibre or macrobends increase FRD in two ways. First, there is an increase in beamwidth of about

$$\frac{\Delta\theta}{\theta} \sim \frac{d}{R} \tag{3.33}$$

where d is the fibre diameter and R is the radius of curvature of the bend. Clearly very sharp bends must be avoided, but in practice this mechanism will not be important. Second, macrobends can exacerbate microbending by induction of stress in the core-cladding interface. This effect is pronounced in fibres where microbending is already present but is not significant in good quality fibres. The author finds that for a 50μm core diameter fibre no increase in beamwidth is apparent with bends of radii of curvature as small as 1cm, for θ between 4° and 9°.

Fibre end preparation induces stress and as a consequence FRD. A common method of fibre end preparation involves epoxing a ferrule onto the end of the fibre to support it during polishing and in subsequent use. However many epoxies tend to shrink as they cure and this mechanism tends to induce FRD, presumably by either moving the fibre into contact with the metal edge of the end ferrule or more likely by inducing pressure on the fibre. It is worth noting that the best FRD results (Barden 1987) were obtained with fibres that had the ferrules removed after polishing. Unmounted fibres might be useful for measurements but they are not robust for general use. Therefore, fibre end preparation techniques are critical to achieve low FRD.

The facial roughness of fibres can also have an effect on FRD. Roughness on the macroscopic scale will cause light, properly guided by the fibre, to be launched out of the fibre at extreme angles. High optical quality of the fibre ends is an essential factor in achieving a good junction with any optical surface. The importance of having a flat surface perpendicular to the fibre axis is clear from figure 3.8 (b).

3.8 Conclusions

The principles of light propagation and attenuation mechanisms in optical fibres have been outlined with particular reference to FRD. A new method to measure the performance of any optical arrangement has been presented.

To make fibres of spectroscopic quality it is necessary to quantify the degree of FRD by studying which fibres and mounting techniques provide the minimum in FRD. Also, given that the new generation of multiobject spectroscopic systems use large number of fibres it is important that the fibre evaluation techniques are quick and reliable. The model described in the previous sections forms an excellent basis for this type of evaluation because it allows us the use of a simple parameter to characterise FRD performance. This has the additional advantage that different workers using this parameter can quickly compare results.

The experimental method proposed is the following: First, the parameter D must be determined experimentally, via a very simple experiment in which a laser is used to input collimated light and the far-field output of the fibre is observed. By fitting the model to this data D can be obtained. Then, the FRD performance for any particular

application can be predicted from equation 3.30 using the value of D obtained and the function G that describes the input beam.

The model successfully predicts real experimental results, as will be discussed in chapter 4 (§ 4.5). Moreover, the examples given in the previous section illustrate the potential of the model for studying different situations relevant to astronomical applications, without the need to setup experiments for each specific case.

4 OPTICAL FIBRE EVALUATION TECHNIQUES

4.1 Introduction

The importance of the losses due to FRD was established when the first multifibre systems were built (Angel *et al.* 1977, Gray 1983). Since that time many groups have developed techniques to evaluate the degree of FRD for different types of fibre. It became apparent that apart from the beamspreading caused by imperfections of the fibre, there are other mechanisms that contribute to increase the FRD. Such mechanisms include procedures for fibre end preparation and polishing. Furthermore, measurements of FRD might also depend on the experimental techniques used for the measurements themselves.

The inconsistency in the results of different experimenters (*e.g.* Gray 1983, Powell 1983, Barden 1987 & Ramsey 1988) has been attributed, in part, to the lack of a standard way of calibrating the fibres. Indeed, the results depend critically on many factors involved in the complex evaluation techniques.

The new generation of multifibre systems will have hundreds of fibres and it is therefore essential, given the large number of fibres involved, that the fibre performance be measured accurately and efficiently. Furthermore, since progress has been made to optimise the performance of multiobject spectrographs it is crucial that fibres meet the

specifications of such spectrographs. Without a reliable evaluation method it is practically impossible to understand and therefore to minimise the mechanisms that degrade the fibres.

In this chapter four different methods developed in the laboratory for measuring fibre throughput are described. These developments were a continuous process resulting, usually from encountering specific problems. The first method is based on a photodiode (the photodiode experiment), the second one is based on a cryogenic CCD (the CCD experiment). The third technique is based on a CCD TV camera (the image experiment). The results obtained with the three methods are consistent. However, the time involved in these measurements is not practical for routine evaluation of hundreds of fibres.

Another approach to the problem was attempted. The outcome was the development of a technique based on a simpler experiment and a theoretical model. The model was described in chapter 3 (§ 3.7). The experimental verification of the model predictions required a new experimental setup (the laser experiment) and the use of the facility provided by the image experiment. The model reproduces successfully the experimental results. As a consequence a new technique to measure the FRD of any fibre via a very simple laser experiment and the theoretical model is proposed. This technique has proved to be efficient and reliable.

The techniques are presented here in order of complexity, rather than in chronological order. The most sophisticated one is the image experiment and it is described first, in section 4.2. The software developed to reduce the data frame, the detector performance and some throughput results are shown and discussed. In section 4.3 the photodiode experiment and the results obtained with this technique are described. Section 4.4 presents the CCD experiment and a discussion of the results obtained with it is given. In section 4.5 the experiments carried out to test the validity of the theoretical model are presented.

Section 4.5.1 describes the collimated input beam case (the laser experiment) and section 4.5.2 the uncollimated beam case (the image experiment). Finally, the conclusions are presented in section 4.6.

4.2 The Image experiment

The main aim of this experiment was to measure the total transmission of the fibre relative to a circular aperture of the same dimensions as the fibre core. The losses and errors introduced in the equipment which launches the light into the fibre or pinhole will be the same for both and therefore the results will be an accurate representation of the losses due to the fibre.

A diagram of the experimental setup is shown in figure 4.1. The diffuse tungsten source provides uniform illumination for the iris I_1. This is imaged, by a 400F/50D achromatic lens and a 50F/40D camera lens with an adjustable iris I_2, onto the input end of the fibre in the focal plane FP1. A beam splitter mounted near the source allows viewing of the fibre end with a CCD video camera (C_a). Light from the other end of the fibre is collected directly by another CCD TV camera (C_b) which is the main detector for the experiment. The system is arranged in such a way that the fibre can be easily removed and the whole detector assembly moved forward such that the two focal planes FP1 and FP2 coincide. The fibre ends and the detector are mounted on x, y, z micropositioning stages.

For focal ratio measurements, the image of iris I_1 is focused onto the input fibre end. Iris I_2 is set at the desired input focal ratio and the far-field output of the fibre is captured via the frame-grabber. The fibre is then removed and a direct measurement of

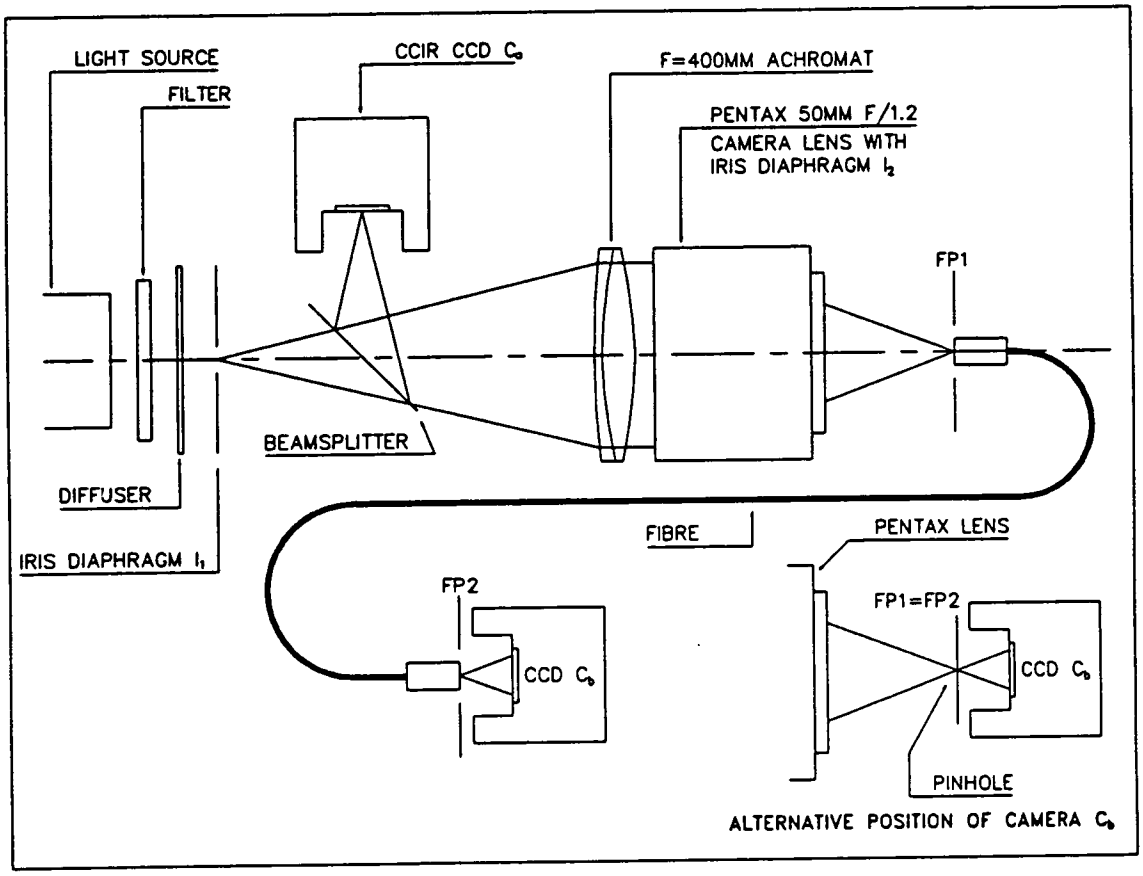

Figure 4.1. Schematic setup for the image experiment. The FRD is measured by comparing an input beam of a given f-ratio with the f-ratio of the output beam.

the input intensity is made, using a pinhole of the same dimensions as the fibre core. It is vital that the pinhole and the fibre ferrule at the output end are very black otherwise reflections from the CCD cover glass can come back to the CCD. A shiny fibre and ferrule can give results which indicate that the fibre is more efficient than the pinhole!

The configuration allows the pinhole to be positioned in exactly the same place as the fibre input end. The output end of the fibre is fixed to the detector with a special holder that positions the fibre at the same distance from the detector as that of the pinhole. This distance was determinated with an accuracy of 1.2%. The time between exposures is very short so effects due to drifts of the light source are practically eliminated.

Camera C_a was introduced to guarantee that the fibre and the pinhole are in the same position and focus. This is simply achieved by monitoring the output of camera C_a when adjusting the position and focus. The correct alignment of the fibre with the input beam is obtained by adjusting the fibre tilt until the size of the beam shown by C_b is minimised.

The diffuser is to provide uniform illumination both in beam angle and across the fibre input end. The system is versatile and it is not restricted to a particular fibre size. If desired I_1 can be completely open to project a bigger image than the fibre core. This option is useful to test the sensitivity of the results to the image size. The actual size of the fibre core and cladding as well as the pinhole size can be measured *in situ*. The degrees of freedom offered by the x-y micrometer stage in combination with the acquisition camera make the measurements easy to perform. The estimated errors in the FRD measurements are about 5%.

4.2.1 Reduction software

The resultant images from C_b are stored in a PC via a frame grabber (PCVISIONplus, Imaging Technology Inc.) and afterwards they are transferred to the local STARLINK VAX cluster, using an Ethernet network, where the reduction is carried out. The reduction software integrates the light falling within annuli of varying radii to obtain a measurement of the output throughput.

The throughput of the fibre and of the pinhole is found by the software as a function of the output focal ratio. The first step is the estimation of the background level to be subtracted from all the pixels: the program calculates the average number of counts in two sets of columns of 2450 pixels each. These columns were chosen close to the CCD edge, avoiding the image of the fibre output beam but at the same time excluding extreme pixels that might introduced edge effects.

The software then finds the image centre by calculating the weighted average of all the pixels where the weight is their intensity. It associates a radius to each pixel and calculates the eccentricity which in the ideal case should be equal to zero and is a useful parameter sensitive to tilting of C_b. The image profile is calculated as the number of counts within each annulus divided by its area. To find out the total number of counts integrated for each radius the program adds up the contribution of all the annuli up to that radius. The radii are converted to output focal ratio taking their reciprocal and multiplying them by the appropriate constant which is the distance between the pinhole/fibre output end and the detector. A correction is applied to compensate for the fact that the off-axis rays do not hit the CCD at right angles and therefore give a lower reading than on-axis rays of the same intensity.

Once the throughput of the fibre and of the pinhole are calculated as a function of the output f-ratio, absolute results are obtained by normalising the fibre throughput

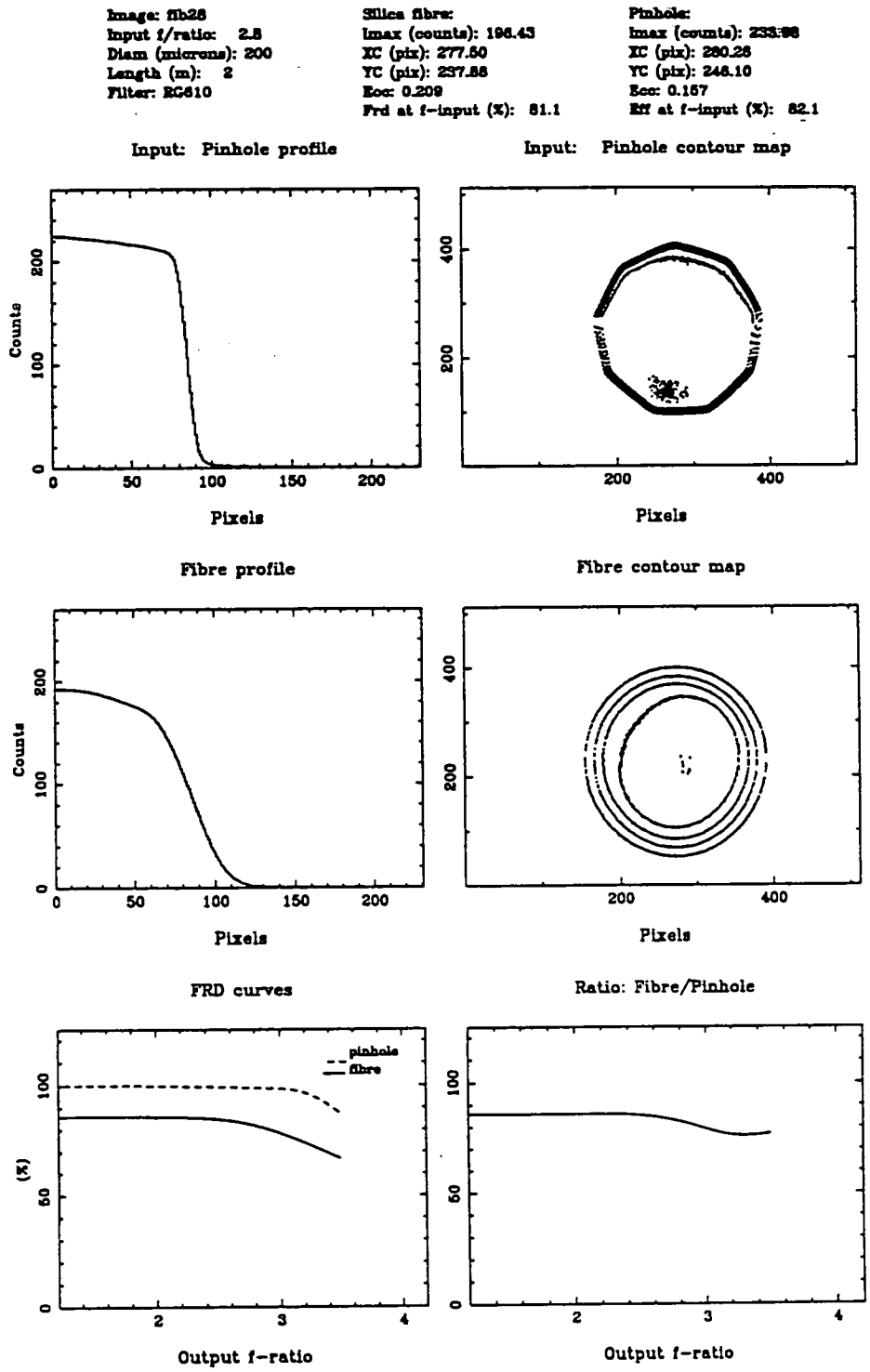

Figure 4.2. Example of the output plot from the data reduction package for the experiment shown in figure 4.1.

values with the pinhole throughput value at maximum aperture. The latter is defined as the minimum distance between the centre of the image and the nearest edge.

The throughput values obtained for the pinhole are normalised with the same constant so the input profile is available for comparison. Thus an equivalent FRD curve is obtained for the pinhole. The efficiency is defined as the ratio between the pinhole and the fibre FRD curves. The output of the program is a set of curves: the pinhole profile and its contour map, the fibre profile and its contour map, the FRD plot of the pinhole and the fibre and the plot of the ratio between them. It includes the parameters of the experiment such as input f-ratio, fibre core diameter, fibre length, any filters used and the output values including maximum intensity, centre coordinates and eccentricity. Figure 4.2 is an example of the output file for a test fibre.

4.2.2 The use of a video camera as a detector

The detector most commonly used for measuring fibre throughput has been the photometer. Normally it is based on a photodiode due to its high stability and resolution of approximately 1 in 1000. A system composed of a TV camera and a frame grabber has lower resolution, of about 1 in 200 but offers the great advantage of providing image information. Therefore a CCD TV camera (COHU Inc.) was chosen as the main detector for this experiment, C_b in figure 4.1.

In a CCD TV camera the background level is caused by the dark current and by the bias level of the analog to digital converter. It produces a uniform number of counts with an amplitude of about 2% of the full scale when no light is incident on the detector. When only a fraction of the CCD is illuminated the background level has to be measured in those pixels that are not receiving light. If the system is well coupled this level will be constant and the system is photometric.

For throughput measurements camera C_b was configured to give a linear video signal relative to black and white levels *i.e.* the automatic gain control was disabled. To test the linearity of C_b the following experiment was carried out. Light from a tungsten lamp provided uniform illumination across the CCD, a long pass filter RG610 blocked the radiation below 610 nm. The intensity of the light source was decreased, via neutral density filters, according to the relationship,

$$I_t = I_o 10^{-D} \tag{4.1}$$

where I_t is the transmitted intensity, I_o is a reference intensity and D is the filter reduction factor. If more than one filter is used the total reduction factor is the sum of the individual contributions. Eight images were obtained with increasing numbers of filters. The resultant images were transferred to the local STARLINK VAX where the reduction was carried out. A dark frame was taken to estimate the background level to be subtracted from the rest of the images. For each data frame the intensity I_t was calculated as the mean value of the total number of counts per pixel. The reference intensity I_0 was defined as the mean intensity of the first image obtained without any filter.

The same experiment was repeated after replacing camera C_b by the photodiode. Figure 4.3 shows the measured intensity (I_t/I_0) as a function of the predicted intensity (I_t/I_0), according to equation 4.1. The solid circles represent the experimental results obtained with the CCD TV C_b camera and the crosses are the data corresponding to the photodiode. It can be seen that the CCD TV camera response is practically as linear as the photodiode response.

The variations in the background level were estimated from a set of seven images of the pinhole, obtained in the same conditions, successively during a one hour period.

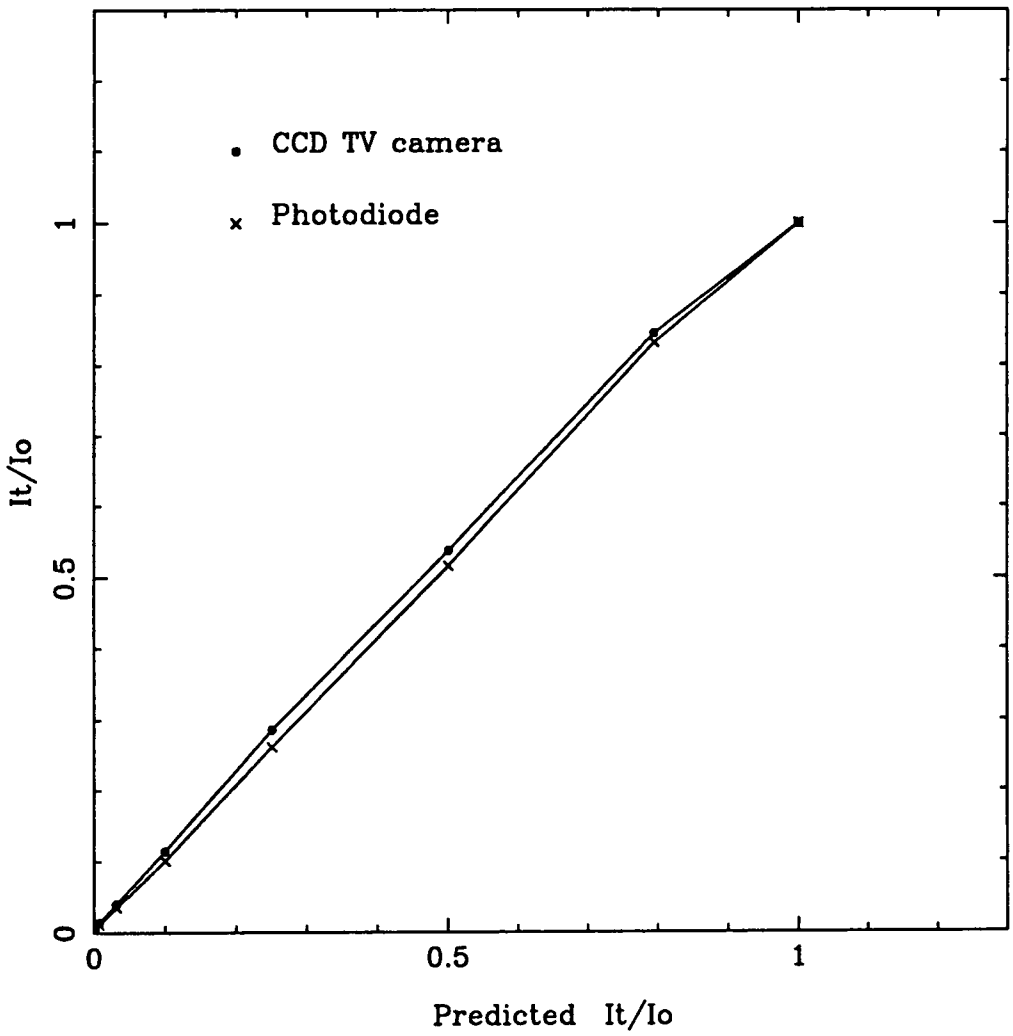

Figure 4.3. Detector linearity test. Predicted intensity according to equation 4.1 *vs.* Measured intensity. The solid circles and the crosses are the experimental results obtained with the CCD TV camera and the photodiode, respectively.

The background level was calculated for each of the seven images, as the average number of counts in two set of columns of 2450 pixels each. The variations were less than 2% . An estimation of the CCD spatial uniformity was made by comparing the residual counts in the columns used to estimate the background. The two set of columns were chosen from opposite sides near the edges. It was found that on average the difference was less than 1% .

In summary, the CCD TV camera response is good enough for the image experiment both in terms of linearity and uniformity. Furthermore, it has the advantage of the real time display facility which is essential to achieve good alignment.

4.2.3 Focal ratio degradation results

The test fibre used in these experiments was an all-silica fibre of 600μm core diameter, 2m long, manufactured by Polymicro Technologies (FWP600720820). It was prepared in the laboratory and polished by hand with different grades of aluminum oxide papers ($30, 9, 3, 1$ & 0.3μm). The fibre transmission characteristics are shown in figure 4.4. It was chosen for its high transmission up to 2μm with the purpose of measuring its performance in the optical and the IR. The following results were obtained in the optical with the experimental setup shown in figure 4.1 and described in last section, using a long pass filter RG610.

The first results were obtained with the iris diaphragm I_1 open such that the fibre input end was fully illuminated. For FRD measurements the image of iris I_1 was focussed onto the input fibre end and three images of the fibre far-field output were obtained at the following input f-ratios: f/2.8, f/5.6 and f/11. The fibre was then removed, iris I_1 was focussed onto a pinhole of the same dimensions as the fibre core and direct measurements of the input intensity were made at the same input f-ratios.

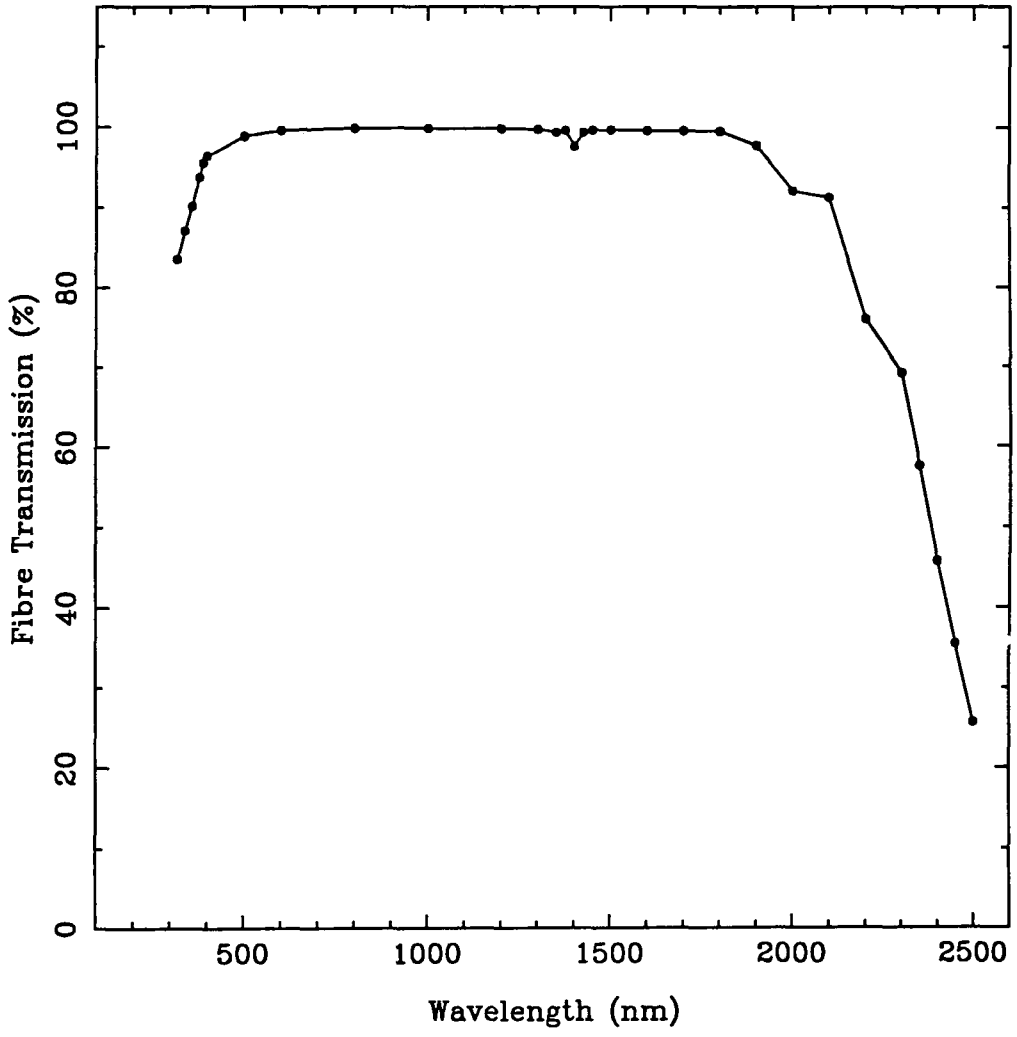

Figure 4.4. Fibre transmission characteristics according to Polymicro Technologies, series FWP. The curve corresponds to a fibre 2m long.

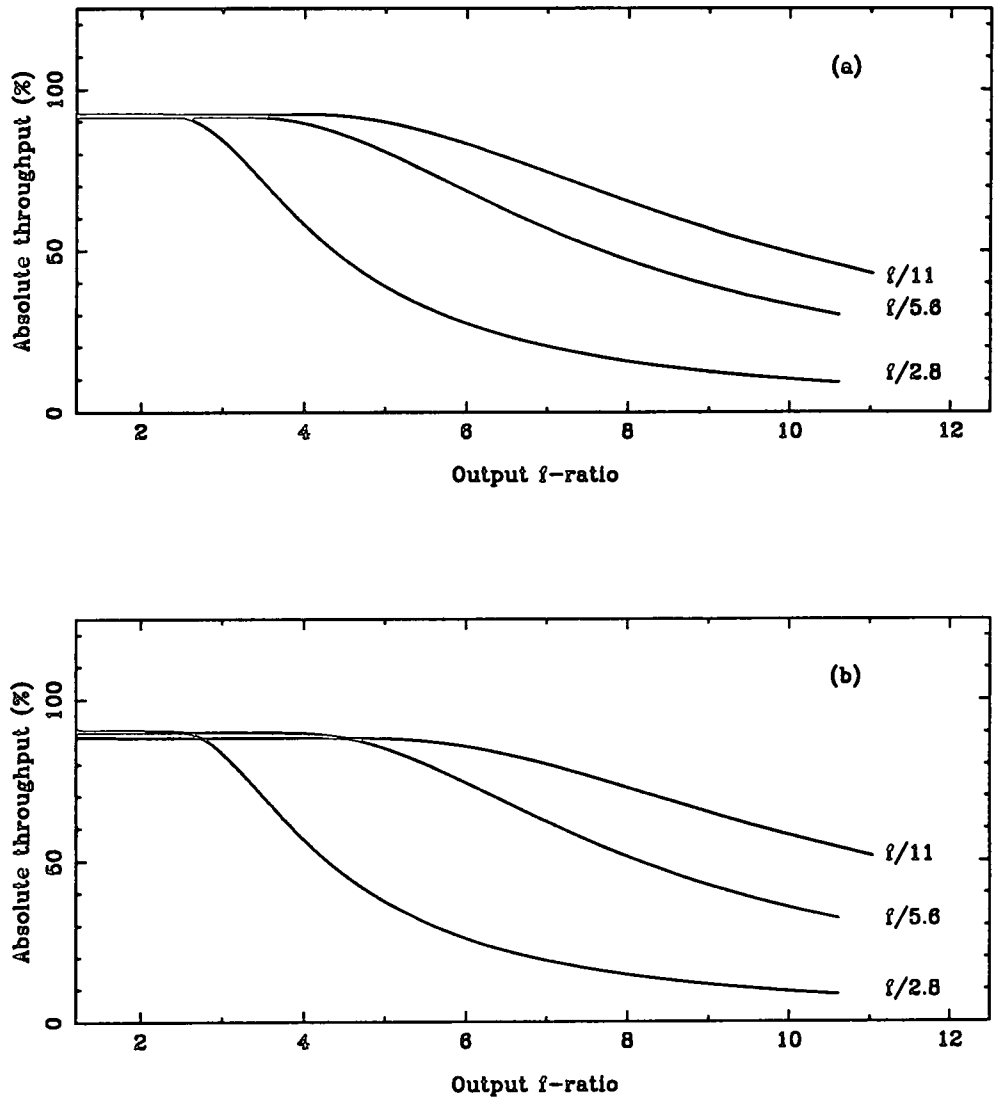

Figure 4.5. Focal ratio degradation curves for a test fibre 600μm core diameter, 2m long manufactured by Polymicro Technologies and polished by hand in the laboratory. The f-ratio of the input beam is indicated. a) Results obtained with the fibre input end fully illuminated. b) Corresponding results to the fibre input end partially illuminated.

The FRD curves obtained for each input f-ratio are shown in figure 4.5 (a). The three curves intersect the y-axis at about 90%, therefore the absorption losses and those due to Fresnel reflections at its ends are about 10%. A summary of the results is given in table 4.1 (a), where the first column shows the f-ratio of the input beam f_{in}, the second column shows the percentage of the input beam output into the same f-ratio and the third one presents the f-ratio of the output beam for which all the light is collected, f_{out}. The latter is estimated from the angle for which the profile of the fibre far-field output reaches zero.

Table 4.1 (a). FRD results for full illumination

f_{in}	% of f_{in}	f_{out}
f/2.8	87.8	2.26
f/5.6	73.0	3.45
f/11	42.8	4.32

The fibre performance in terms of FRD is poor in spite of the high quality of its ends. For an f/2.8 input beam the total amount of light within an f/2.8 output beam is 87.8%, for an f/5.6 input beam the corresponding proportion of light is 73% while for an f/11 input beam is only 42.8%. The results show clearly that the FRD is more severe for slow input beams, as discussed in chapter 3. The effect can be better appreciated by examining f_{out}, from which it is seen that for an f/11 input beam the output f-ratio is f/4.32, but for an f/2.8 input beam the output f-ratio is only degraded to f/2.26.

Another set of measurements were carried out with the input fibre end partially illuminated, projecting a 300μm light spot. The FRD curves are shown in figure 4.5 (b). It

can be appreciated that the performance obtained is similar. The results are summarised in table 4.1 (b) where the information is presented as in the previous table.

Table 4.1 (b). FRD results for partial illumination.

f_{in}	% of f_{in}	f_{out}
f/2.8	87.2	2.40
f/5.6	78.5	4.00
f/11	51.4	5.20

For an f/2.8 input beam there is practically no difference from the results obtained under full illumination, but at f/5.6 the throughput increment is about 5% while for an f/11 input beam it is almost 9%. The improvement in the FRD results at f/5.6 and f/11 in the second measurement is possibly because the input rays avoid the first part of the core/cladding interface which are likely to be stressed due to the end ferrule. Thus, a strong local source of FRD is avoided. The FRD from the rest of the fibre and the output end remains the same. The difference between the full and partial illumination results may also be due to alignment differences or possibly the partial illumination sampled a cosmetically clean area of the input face.

A difference between the fibre core diameter and the pinhole diameter would change the normalization constant, which is the total number of counts within the maximum aperture in the pinhole data frame. Therefore the percentage of the total intensity would change but not the shape of the curves. The error introduced by the manufacturing tolerances are of the order $4\delta r/r$ where r is the radius and δr is the difference in the radius. For $\delta r = 2.5\mu$m the error will be about 3%. The diameter of the fibre core and

of the pinhole were carefully measured using a measuring machine with 5μm resolution. The results obtained, as the average of several measurement, are the following for the fibre input end $d_c = 604\mu$m, for the output end $d_c = 610.5\mu$m and for the pinhole $d_p = 603.5\mu$m.

The sensitivity of the results to the intensity of the light source was tested as follows. For an f/2.8 input beam three images of the pinhole were obtained, firstly without any neutral density filter, then with a 0.1 neutral filter and finally with a 0.3 neutral filter. The decrease in intensity according to equation 4.1 was 20% for a 0.1 reduction factor and 50% for 0.3. The corresponding fibre images were obtained in the same conditions, therefore errors due to misalignments were eliminated. The differences in the results were less than 1%. The light source stability, estimated as described in section 5.3.2., is about 2.25% within a 1 hour time period. Moreover the time elapsed between exposures was a few minutes, therefore the error introduced by the light source is minimal.

Another series of experiments were carried out with a 200μm core diameter fibre, 2m long, manufactured by Polymicro Technologies (FHP200240270). Figure 4.6 shows the transmission characteristics of this type of fibre. The test fibre was provided by the Royal Greenwich Observatory and had two brass ferrules and a brass block epoxied over the fibre at the midpoint. The fibre ends were prepared and polished by Logitech Ltd. An image of each end is shown in figure 4.7 and 4.8 , where the magnification factor is 300. The high quality of the fibre ends can be appreciated.

The throughput results were obtained, using a long pass filter RG610, for the following input f-ratios: f/2.8, f/5.6 and f/8. The first measurements were taken under the full illumination condition, *i.e.* with iris I_1 open so that the fibre input end was completely illuminated. Another series of measurements were made under the partial illumination condition, projecting a 100μm diameter spot onto the fibre input end.

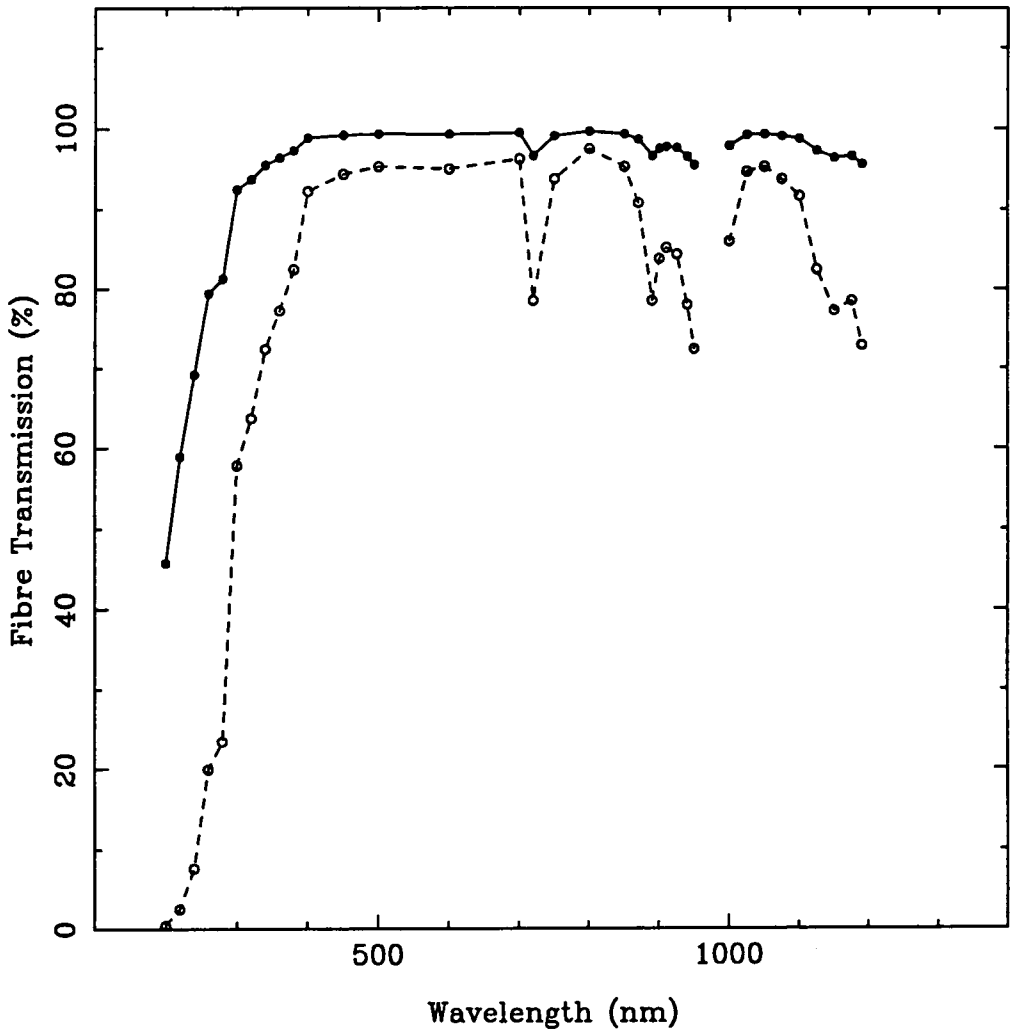

Figure 4.6. Fibre transmission characteristics according to Polymicro Technologies FHP series. The solid line corresponds to the transmission of a fibre 2m long. The dotted curve corresponds to the transmission of a fibre 14m long (see §4.3).

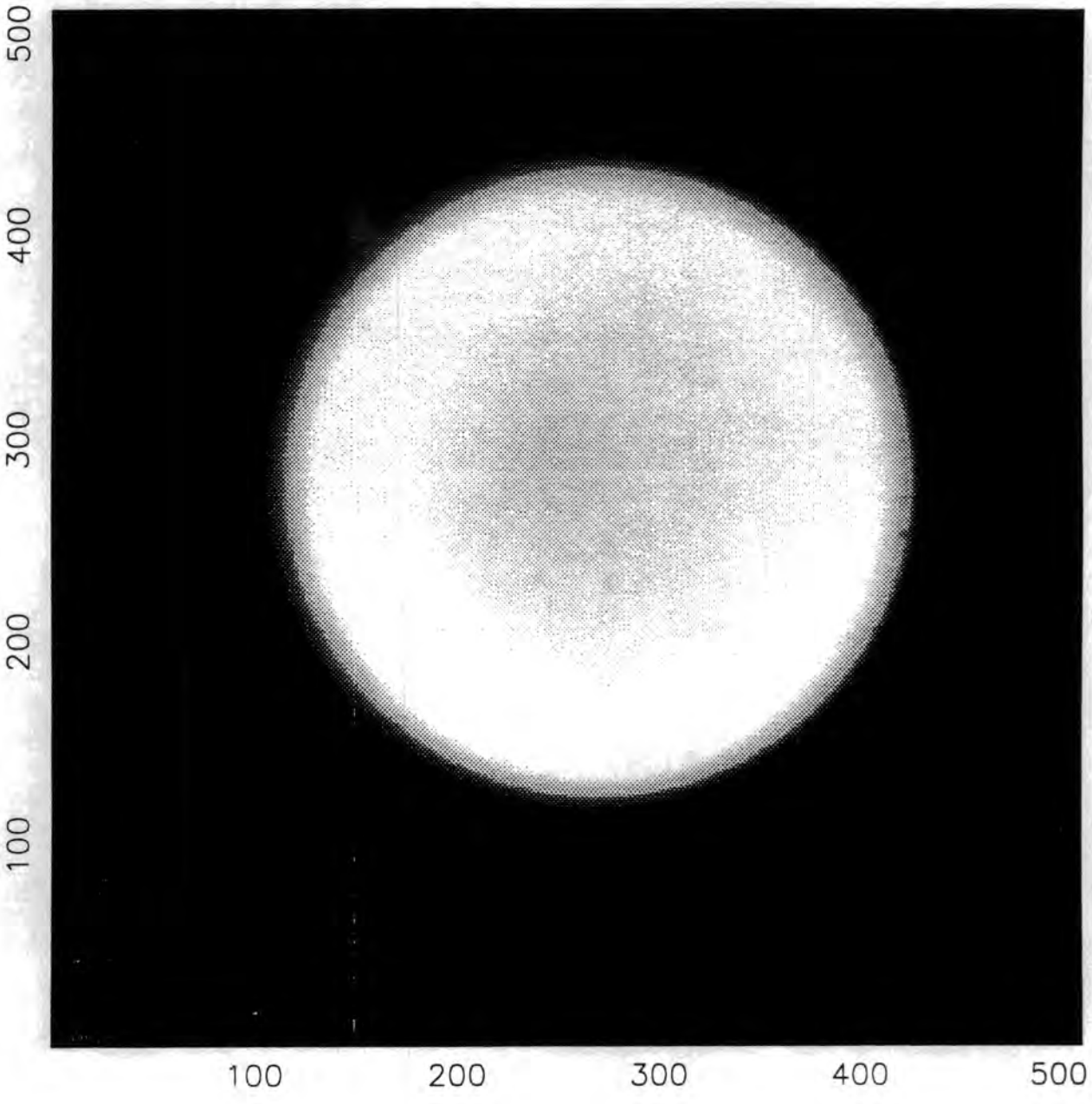

Figure 4.7. Input end of the 200μm core diameter fibre, 2m long, manufactured by Polymicro Technologies (FHP200240270), used in the FRD experiments.

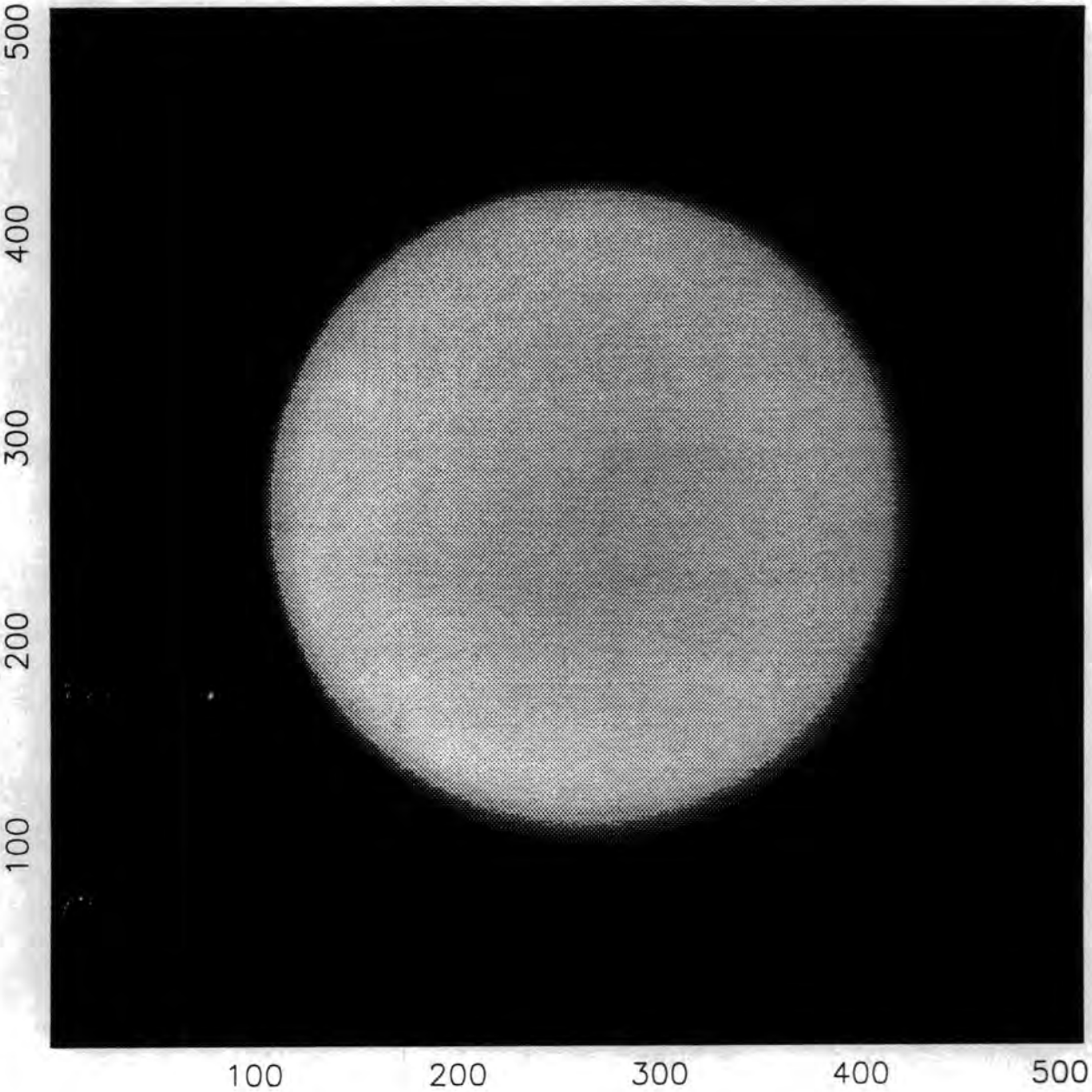

Figure 4.8. Output end of the 200μm core diameter fibre, 2m long, manufactured by Polymicro Technologies (FHP200240270), used in the FRD experiments.

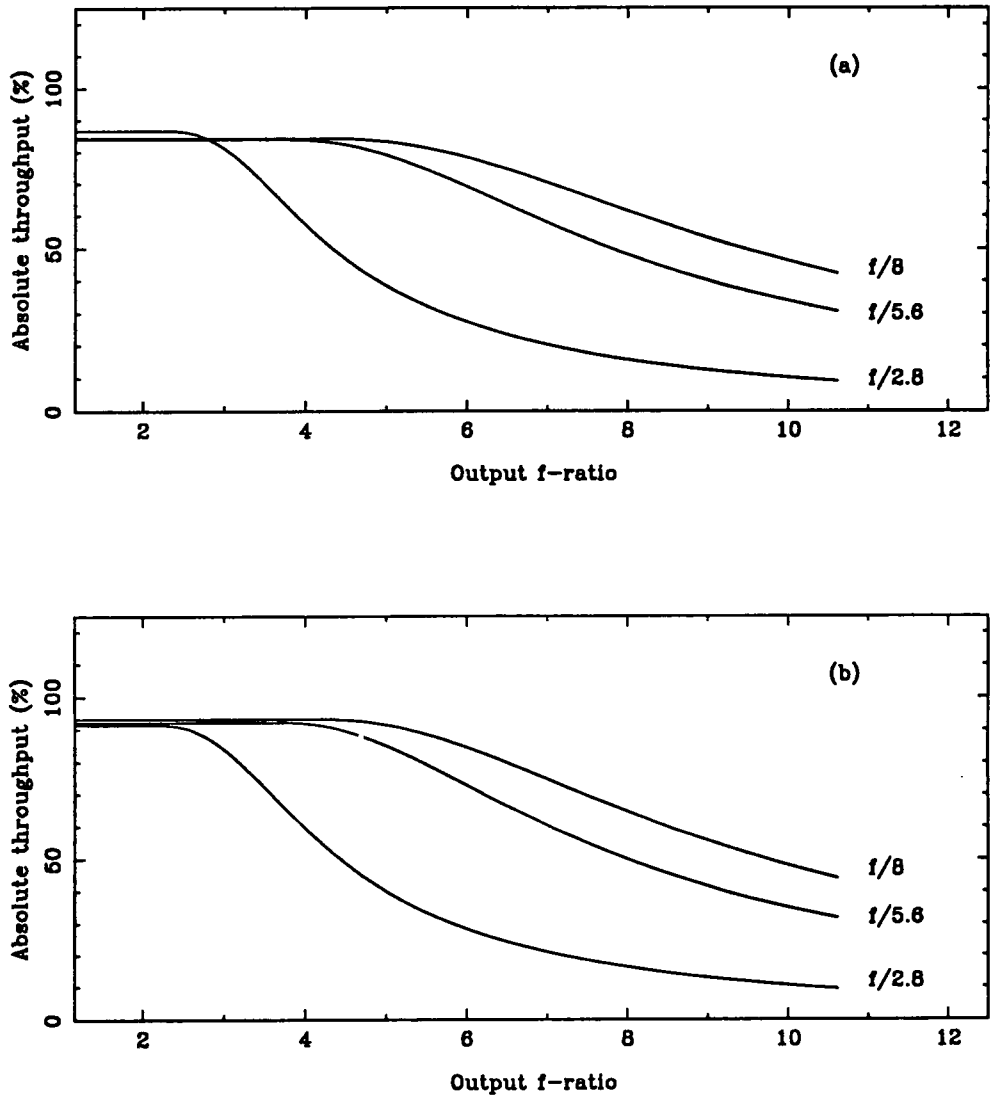

Figure 4.9. Focal ratio degradation curves for a test fibre 200μm core diameter, 2m long, manufactured by Polymicro Technologies and polished by Logitech Ltd. The f-ratio of the input beam is indicated. a) Results obtained with the fibre input end fully illuminated. b) Results corresponding to the fibre input end partially illuminated.

Figures 4.9 (a) and (b) show the throughput curves as a function of the output f-ratio, obtained for full and partial illumination respectively. Tables 4.2 (a) and 4.2 (b) summarised the results and the information is presented as before: the first column shows f_{in}, the second the percentage of the input beam output into the same f-ratio and the third column shows f_{out}.

Table 4.2 (a). FRD results for full illumination

f_{in}	% *of* f_{in}	f_{out}
f/2.8	87.2	2.39
f/5.6	77.5	3.94
f/8.0	63.5	4.52

Table 4.2 (b). FRD results for partial illumination.

f_{in}	% *of* f_{in}	f_{out}
f/2.8	83.9	2.30
f/5.6	72.9	3.84
f/8.0	60.5	4.45

The difference between the results of the two measurements is, on average, about 4%. In terms of f_{out} the discrepancies are marginal. It is interesting to notice in figures 4.9 (a) and (b) the error introduced by the background estimation. The Fresnel and absorption losses are the same, yet the curves in (a) intersect the y-axis at about 87% while in (b) at about 93%.

The sensitivity of the FRD results to the position of the spot at the input fibre end was tested by moving the same test fibre (200μm core) via the xy micrometer stage, such that the spot was displaced 50μm of axis. The measurement was made for an f/2.8 input beam. The percentage of the input beam in an output beam of the same f-ratio was 85.1% which is comparable to the result (83.9%) for an on axis spot.

There is not a significant difference between the results obtained for the two fibres, in particular for those obtained under partial illumination. This suggests that the preparation and polishing by hand in the laboratory gives the same sort of performance as the commercial preparation. However, the differences in the fibre dimensions and characteristics should be kept in mind, for instance, Ramsey (1988) has reported that larger core fibres appear to have better FRD characteristics than smaller core fibres with identical construction. The condition of having high quality fibre ends is necessary but is not sufficient to guarantee good FRD performance.

Regardless of the quality of the test fibres, the most relevant point is that the method described is reliable and versatile. It allows the systematic evaluation of different types of fibres under various circumstances and the data reduction process is easily performed.

4.3 The photodiode experiment

The aim of this section is to compare the throughput results obtained with the image experiment with those obtained using a more traditional method. The technique described here was developed before the image experiment and it was used to evaluate the Autofib-1.5 fibre bundle. All the experimental results obtained with that purpose will be presented

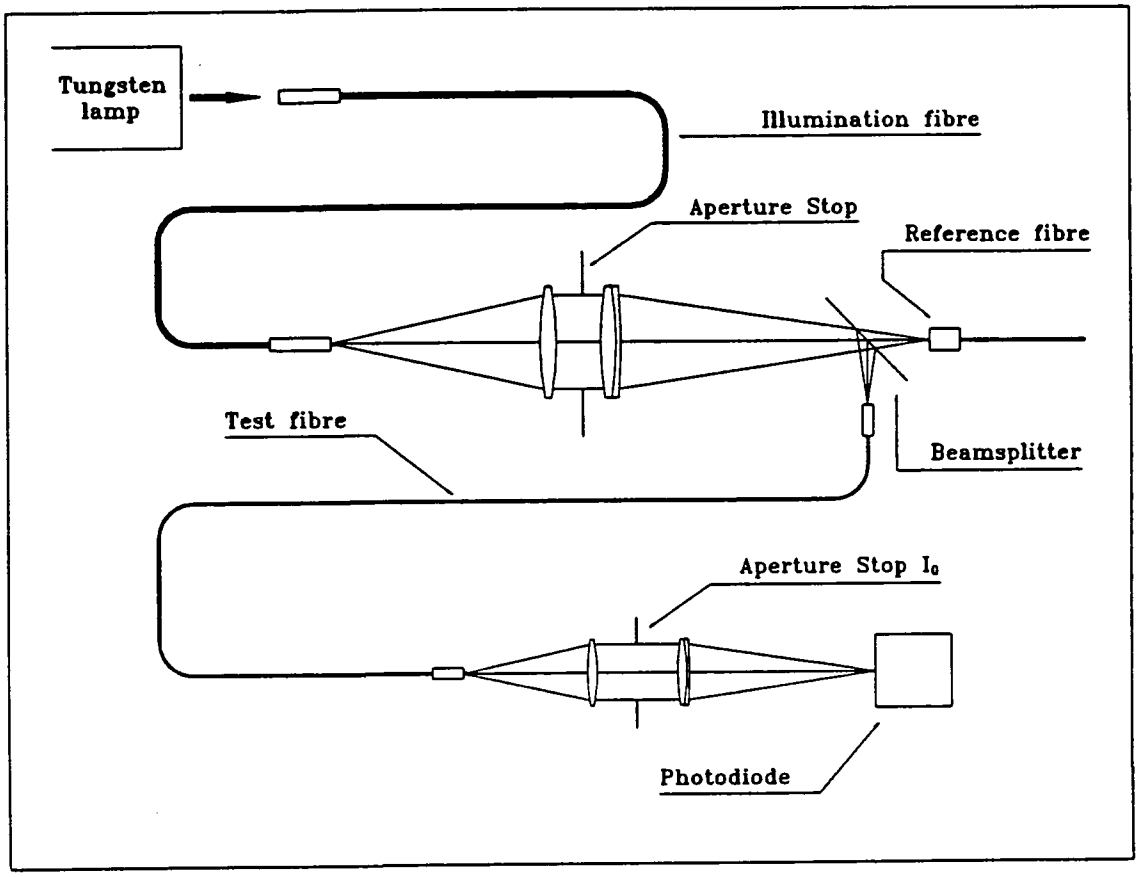

Figure 4.10. Schematic setup for the photodiode experiment. The FRD is measured using a photodiode as the detector.

in chapter 5 while here the experimental setup, simply referred to as the photodiode experiment, will be described.

The setup is shown in figure 4.10. Light from a tungsten lamp is transferred via a 1 mm core fibre to the input of the system. An image of this fibre was focussed and projected onto the end face of the fibre being tested and at the same time, onto a reference fibre by means of a beam splitter. The image was formed by a combination of a singlet 150F/40D lens and an achromat 300F/40D lens. An aperture stop AS defined an f/11 beam such as for the Cassegrain focus of the WHT.

The output end of the fibre was imaged onto a photodiode via 80F/20D and 160F/20D lenses with the output f-ratio defined by iris I_o. The fibre was positioned in a V-groove and held in place by a magnet to keep it in the right position without inducing any stress. This device guarantees a simple and repeatable way of positioning the fibres.

The input optical arrangement was fixed on a bench specially built for this experiment such that the complete system could be moved as a unit without misaligning the components. Similarly the output optical arrangement was mounted on a standard optical bench that could also be moved as a whole without touching the components and changing the alignment.

The light source stability was estimated from the throughput results of the reference fibre. The error introduced by these variations, defined as the standard deviation divided by the mean, was estimated to be 2.2% . The error in positioning the fibre end to align it with the input beam was less than 1% . The repeatability was about 3%, which is the same as the rms values of the error mentioned.

To transform the results to an absolute scale the intensity of the input beam was measured as follows. The test fibre was replaced with a 100μm diameter pinhole such

that the input and the output optical systems formed a single unit. Measurements of the intensity at different output f-ratios were carried out. The scale factor was calculated as the ratio between the pinhole and the fibre areas divided by the intensity of the input beam measured through the pinhole. The results were scaled multiplying the throughput values with that obtained for the pinhole at an f/4.7 output f-ratio.

The following results were obtained measuring the throughput of fibre 24 and 26 of the Autofib-1.5 fibre bundle. The throughput was measured at output f-ratios of f/4.7, f/5, f/6.3, f/8 and f/11.2. The 260μm core diameter fibres, manufactured by Polymicro Technologies in a special custom draw (FHP26286316) are 14m long. Figure 4.6 shows the transmission characteristics of this type of fibre in dotted lines.

Throughput measurements were carried out for the same fibres via the image experiment for an f/11 input f-ratio. For comparison purposes the results for the test fibres were normalised with the throughput value obtained for the pinhole at an f/4.7 output f-ratio. The FRD curves obtained with both methods are shown in figure 4.11 (a) and 4.11 (b) for fibre 24 and fibre 26, respectively. The solid lines are the results obtained with the image experiment while the dotted lines correspond to those obtained with the photodiode experiment. The differences between the curves are within the experimental errors. Undoubtedly the FRD performance is very poor for the two fibres, the amount of light within an f/11 output beam is only 30%. Nevertheless the relevant point is that the results obtained with two completely different methods are consistent.

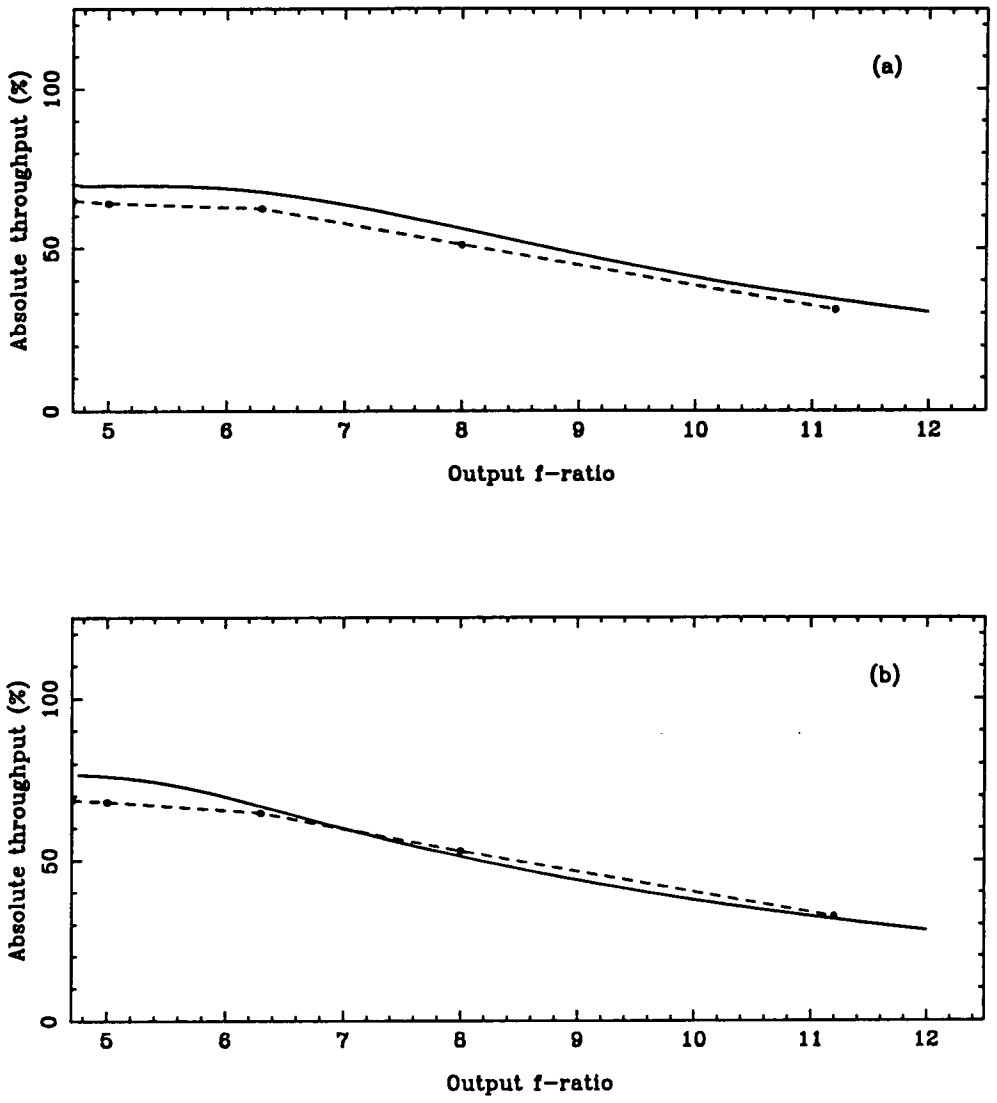

Figure 4.11. Focal ratio degradation curves for two test fibres obtained for an f/11 input beam. Both fibres are part of the Autofib-1.5 fibre bundle. The solid lines are the results of the image experiment and the dotted lines correspond to those obtained with the photodiode experiment. a) Fibre 24. b) Fibre 26.

4.4 The CCD experiment

Another version of the experiment described in the last section was obtained by replacing the photodiode with a cryogenically cooled slow-scan CCD. Chronologically this experiment was developed after the photodiode experiment but before the image experiment.

The setup is shown in figure 4.12. The input optical system was the same as in the photodiode experiment *i.e.* the optics defined an f/11 input beam. However at the output end the fibre far-field output was directly fed onto the CCD. The simplicity of the output setup was adopted to eliminate potential alignment errors in the output optics of the photodiode experiment. At the time the experiments were carried out the detector available was a CCD EEV P8603B.

The actual distance between the fibre end and the detector was determined by focussing a test image onto the CCD using the Hartmann method and measuring the position of the cryostat with respect to a reference. The dewar was then replaced by a screen and its position relative to the reference was also measured. Using these measurements the distance between the fibre output end and the detector was determined with an accuracy of 2.2%. Care was taken to assure that the tungsten lamp intensity was the same as in the photodiode experiment to avoid any wavelength dependent effects. A relatively long integration time of one second was chosen to prevent any possible error introduced by the shutter time response, since the centre of the beam is closed off after the outer parts.

The resultant images were transferred to the local STARLINK VAX cluster where the image reduction process was carried out with software written for this purpose. With the experimental setup described the throughput measurements had to be relative because it was physically impossible to move the CCD dewar to the position required for measuring the intensity of the input beam. Therefore the results were normalised with the fibre throughput value obtained at an f/5 output f-ratio. The FRD curves for fibre 24 and

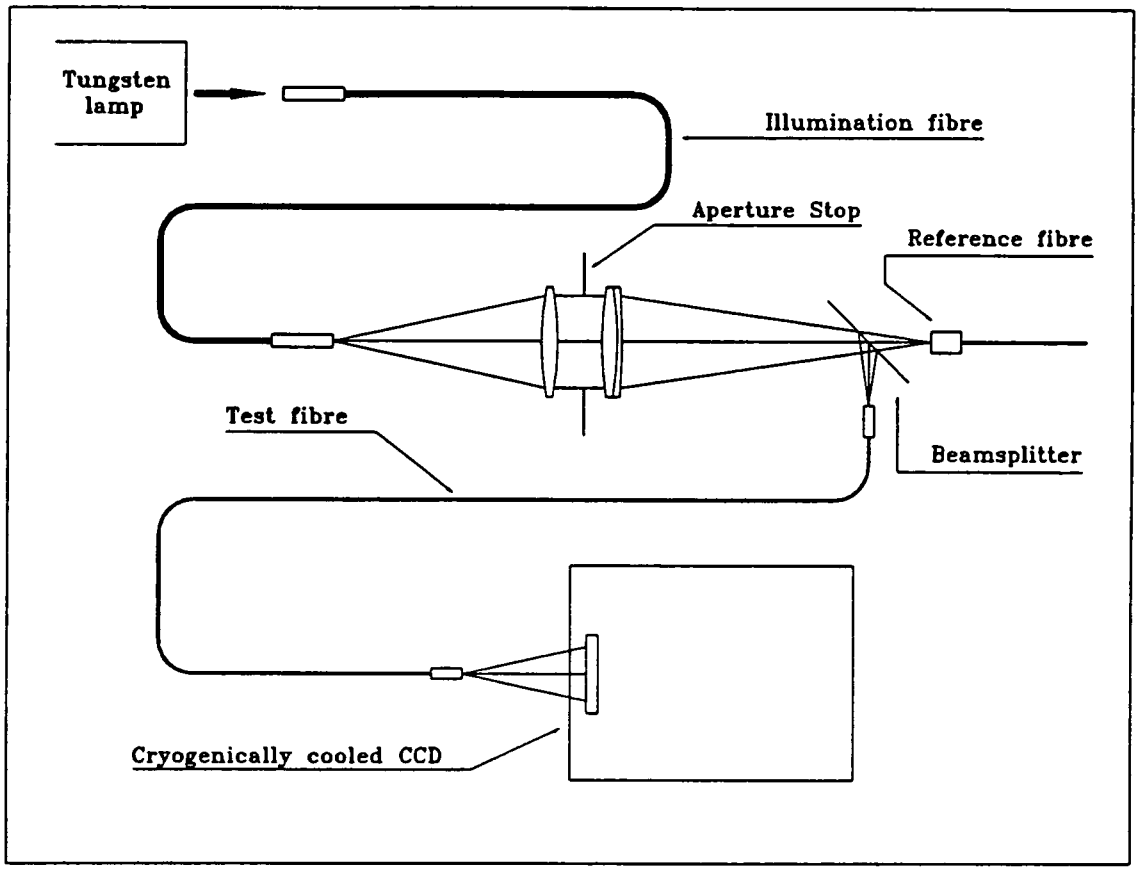

Figure 4.12. Schematic setup for the CCD experiment. The FRD is measured using a cryogenically cooled slow scan CCD as the detector.

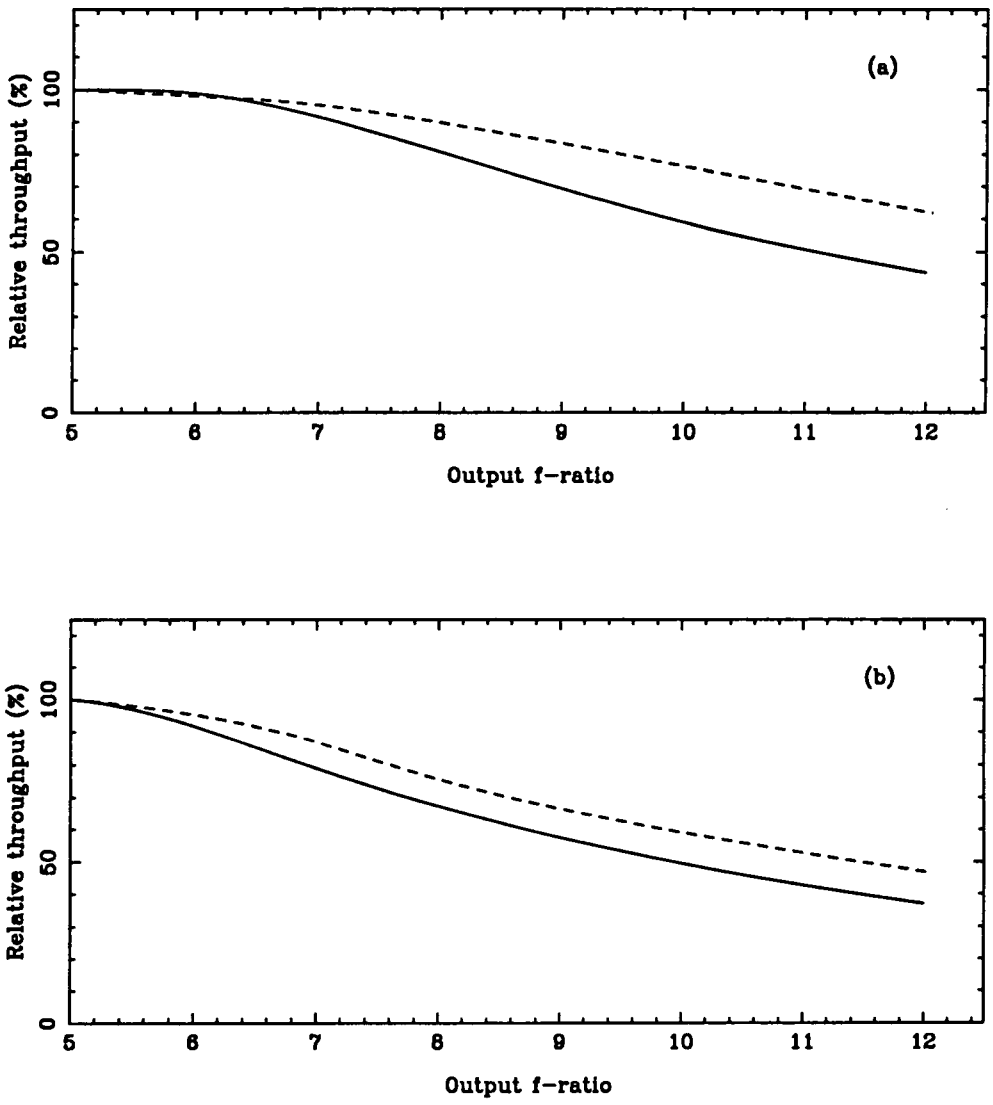

Figure 4.13. Focal ratio degradation curves for two test fibres obtained for an f/11 input beam. Both fibres are part of the Autofib-1.5 fibre bundle. The solid lines are the results of the image experiment and the dotted lines correspond to those obtained with the CCD experiment. a) Fibre 24. b) Fibre 26.

26 of Autofib-1.5 fibre bundle, are shown in figure 4.13 (a) and (b) respectively as the dotted lines. The solid lines are the results shown in figure 4.11, obtained via the image experiment, but now normalised with the fibre throughput value at an f/5 output f-ratio.

For both fibres the results obtained with the CCD experiment are better than those obtained with the image experiment. In the CCD experiment the positioning of the fibre output end at exactly the required distance from the detector was very critical because the dewar window and the shutter left very little space for manoeuvreing. If the fibre output end is closer than it should be an underestimation of the FRD will result. This can explain the differences, in particular because the results obtained via the photodiode experiment are in good agreement with those obtained via the image experiment as can be appreciated in figure 4.11 (a). Another possibility is the normalization point.

A second order effect is the intensity of the tungsten lamp. In the photodiode and the CCD experiment care was taken to assure that the intensity was the same and only neutral filters were used. The image experiment was developed months later and the intensity of the light source was chosen according to the conditions imposed by the experimental setup. Additionally for all the images obtained with this setup a long pass filter RG610 was used.

The results reported so far are illustrative of the complexity involved in the fibre evaluation techniques. Of the three methods discussed the image experiment proved to be the easiest to perform. It provides absolute throughput measurements and all the data, for a given input f-number, is acquired from just two images. The image information is very useful to study phenomena such as radial scrambling and the performance of the fibre under different circumstances. The reduction software already developed is versatile and allows the acquisition of results relatively quickly.

The image experiment offers the advantage over the photodiode experiment that all the information for a pinhole or a fibre is obtained in a single image, avoiding any error that might be introduced by setting the iris at a given output f-ratio. Moreover the intensity of the input beam is measured immediately after the fibre throughput measurement, minimising the effect of any drifts in the light source. In the photodiode experiment the intensity of the input beam was measured only once at different output f-ratios. On the other hand, the photodiode experiment offers the advantage that the throughput measurements are displayed *in situ*, without any further data reduction process.

The image experiment was developed from the CCD experiment to provide a real time display facility, essential when trying to achieve good alignment and to obtain absolute throughput measurements by comparison with a pinhole. The sensitivity of a cryogenic CCD is higher and the level of noise is lower than that of a CCD TV camera, however for throughput laboratory measurements these properties are not very important. Finally the geometry of the dewar makes the CCD rather unwieldy.

In summary, the image experiment represents an improvement over the other two methods previously developed and it can be very useful in studies of the different properties of optical fibres. Nevertheless the level of effort involved and the potential for systematic errors render the image experiment impractical for an instrument with 200 or more fibres. Since the new generation of multifibre systems, such as the 2dF for the AAT and Autofib-2 for the WHT, will have hundreds of fibres it is essential to have a reliable as well as an efficient method of testing fibres.

4.5 The experimental verification of the FRD model

The validity of the theoretical model described in chapter 3 (§3.7) was tested by observing the far-field output of a fibre in the laboratory and by comparing it with the model's predictions. For the case of a collimated input beam (laser light) the beamspreading was measured as a function of the input beam angle. The parameter D was determined by finding the best fit to the data. Using this value of D the model successfully predicts the results of another experiment where the far-field output beam is recorded for input pencil beams of varying f-ratio.

4.5.1 The collimated input beam case

The setup for this experiment, simply referred to as the laser experiment, is shown in figure 4.14. The fibre under test was directly illuminated by a laser beam at an angle of incidence θ_i. The far-field output was projected onto a screen which was imaged by a CCD TV camera. Several images were stored on the data acquisition PC, via a frame grabber, as the angle of incidence of the input beam was changed. The images were transferred to our local STARLINK VAX cluster and reduced via software specifically written for this purpose. An example of the display facility generated by the software is given in figure 4.15. The profile and a contour map of the ring observed in the far-field, when the fibre is illuminated by a laser beam, are shown.

The test fibre used in this series of experiment was another all-silica fibre of 200μm core diameter and 2m length manufactured by Polymicro technologies (FHP200240270). It was polished by Logitech Ltd. and has high quality end faces.

For each angle of incidence a Gaussian fit to the profile of the ring was carried out and its centre and FWHM determined. The distance from the centre of the ring to the

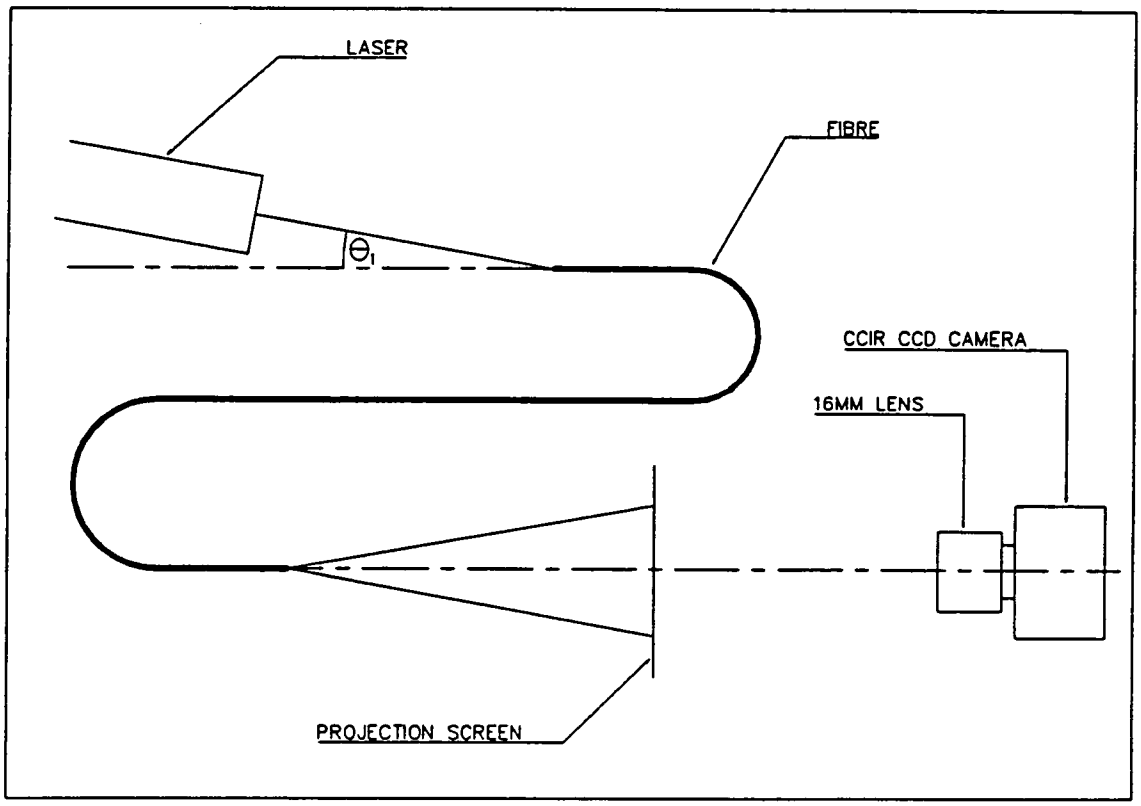

Figure 4.14. Schematic setup for the laser experiment. A collimated input beam is launched at an angle of incidence θ_i into a test fibre. The far-field output pattern, consisting of an annular ring at a mean angle θ_i, is projected onto a screen which is imaged by a CCD TV camera.

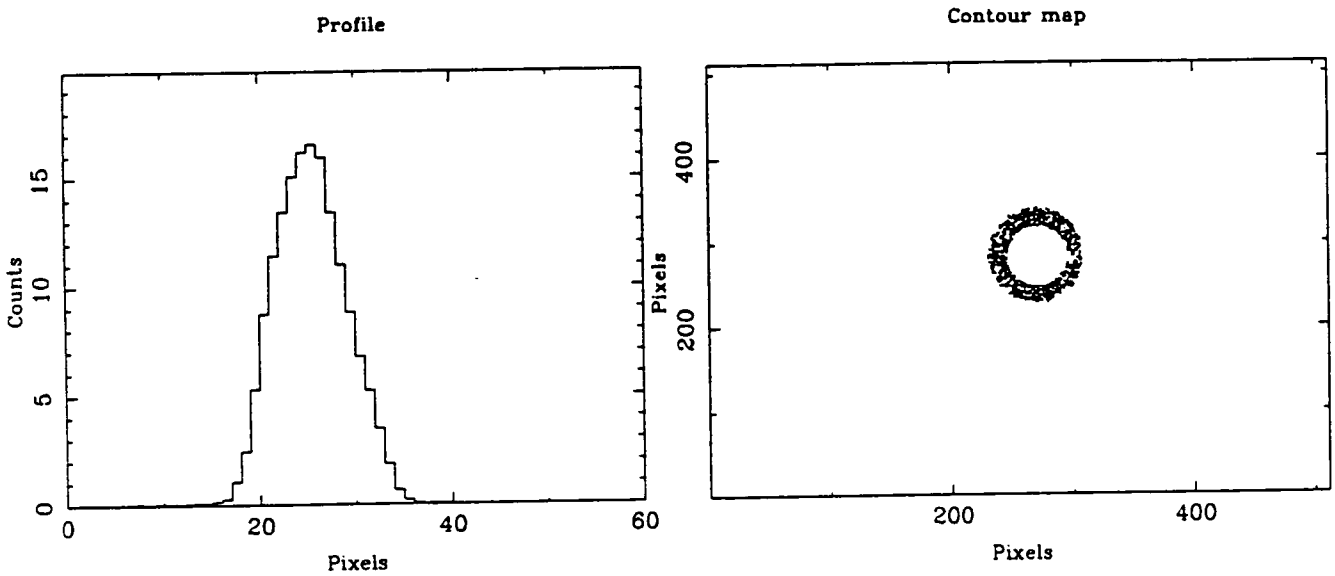

Figure 4.15. Example of the output plot from the data reduction software developed for the experiment shown in figure 4.14.

centre of the Gaussian was associated with the angle of incidence θ_i. To find the value of the parameter D, the approximate solution for P given by equation 3.27 was numerically evaluated for the same angle of incidence θ_i, for a range of values of D and the best fit to the experimental data was noted. The modelling software also gives the radial position of the centre and the FWHM of the predicted Gaussian profile. It is clear from equation 3.27 that D is directly related to the width of the curve: given the length of the fibre L and θ_i the only free parameter is D.

If we assume the laser beam is an extreme ray of a conical input beam we can directly relate θ_i and FWHM to the input and output f-ratios according to the relationships:

$$f_{in} = \frac{1}{2\tan\theta_i} \tag{4.2}$$

$$f_{out} = \frac{1}{2\tan(\theta_i + fwhm/2)} \tag{4.3}$$

Figure 4.16 shows in solid lines the profiles experimentally obtained and in dotted lines the profiles predicted by the model for a value of $D = 15 \times 10^{-5}$ m^{-1}. The input f-ratio calculated according to equation 4.2 is indicated. The agreement between the curves for large angles of incidence *i.e.* for fast input f-ratios, is very good. For small angles of incidence the experimental errors become more significant and the differences are slightly bigger. Nevertheless, the coefficient D is a parameter that characterises the fibre.

Figure 4.17 (a) shows the results obtained for different angles of incidence in a curve θ_i *vs.* FWHM. The solid circles are the experimental results and the curve corresponds to the results from the profiles predicted by theory according to equation 3.27 for $D = 15 \times 10^{-5}$ m^{-1}. The results in terms of f-ratios are shown in figure 4.17 (b), the circles are the experimental results while the solid line corresponds to the prediction from theory.

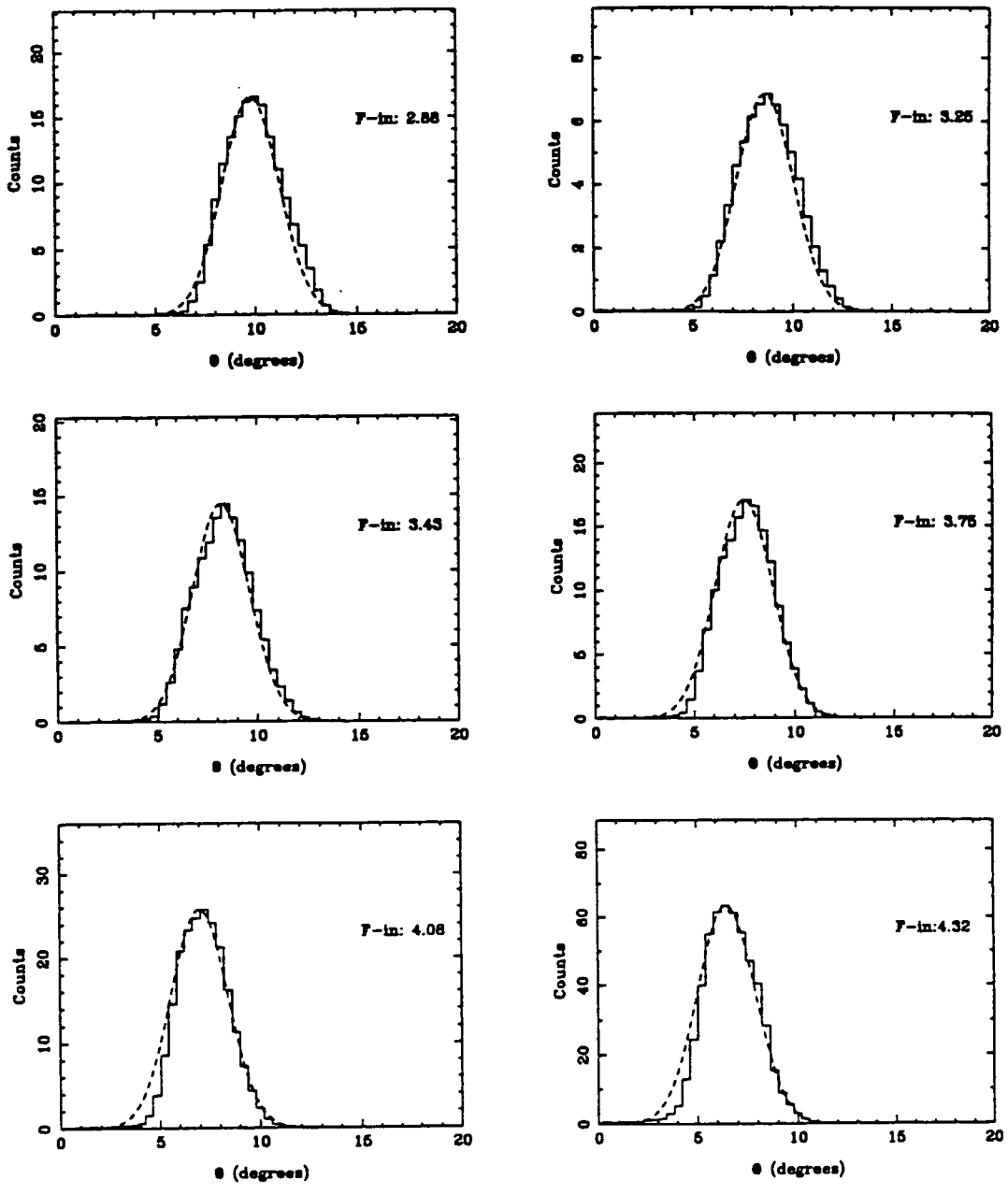

Figure 4.16. Profiles of the far-field output observed when the fibre is illuminated by collimated light (laser beam) at different angles of incidence, as indicated. The solid lines are the experimental results. The dotted lines correspond to the prediction by the model according to equation 3.27, for $L = 2\text{m}$ and $D = 15 \times 10^{-5}\ \text{m}^{-1}$. The value of D was determined by finding the best fit to the experimental results.

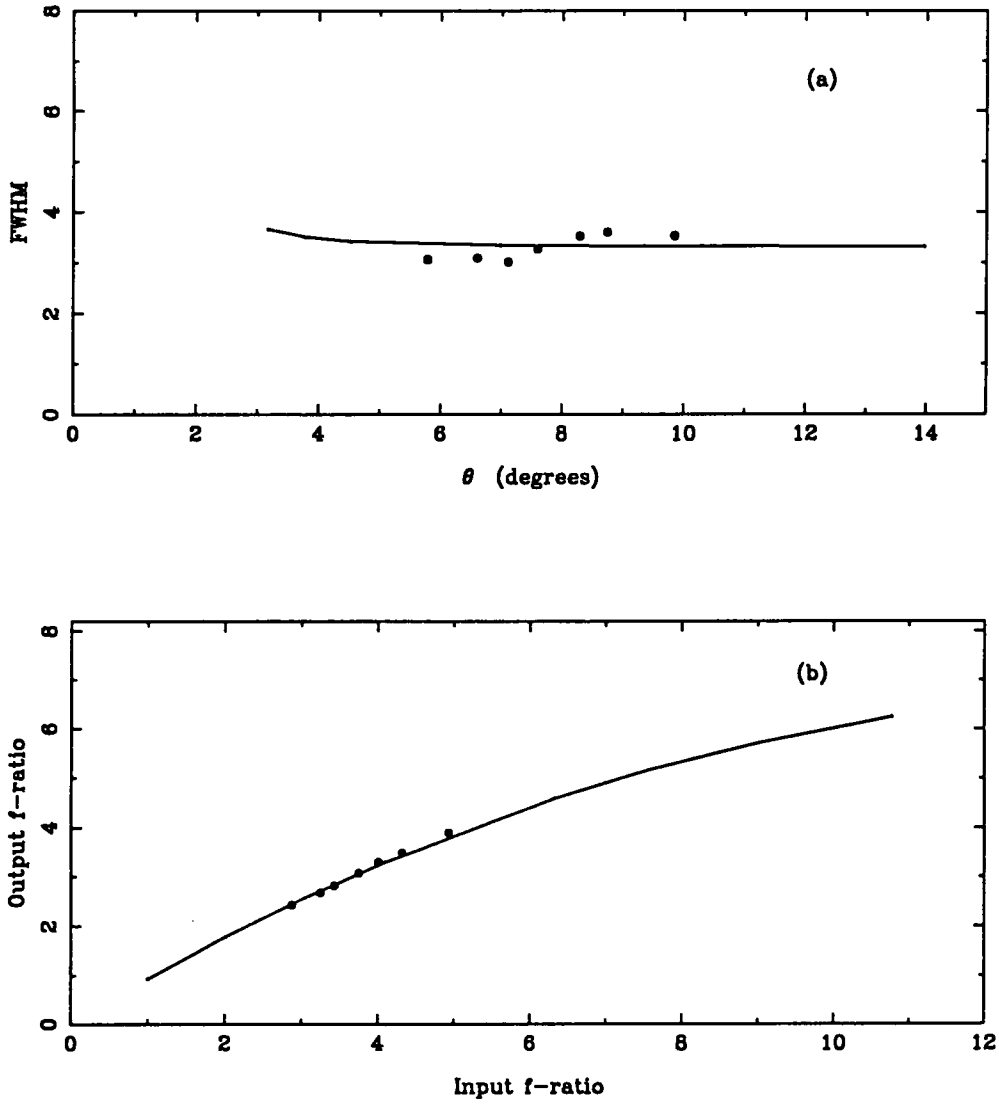

Figure 4.17. a) FWHM of the ring profiles for different angles of incidence. The solid circles are the results from the laser experiments. The curve corresponds to the predictions from theory for $D = 15 \times 10^{-5}$ m^{-1}. b) Output f-ratio as a function of input f-ratio for the test fibre defined according to equations 4.1 and 4.2 respectively. The circles are the experimental results while the curve corresponds to the predictions from theory.

Although equations 4.2 and 4.3 represent an approximation they are very useful because they relate the centre and the FWHM of the profiles to the pencil beam parameters f_{in} and f_{out}.

4.5.2 The uncollimated input case

The validity of the model was also tested against FRD measurements that compare directly an input beam of a given f-ratio with the output f-ratio. The image experiment described in section 4.2 was ideal for this type of measurement. The data frames obtained were analysed via the reduction software presented in section 4.2.1.

As established in section 3.5 (equation 3.30), to determine the function F we must know the input function G that describes the input beam. In this particular case G was obtained experimentally and corresponds to the pinhole profile. The function F was calculated numerically by using the value of D previously estimated from the laser experiment.

Two of the profiles are shown in figure 4.18. The solid lines are the profiles obtained experimentally and the dotted lines correspond to the profiles predicted by the model for an input f-ratio of f/2.8. In figure 4.18 (a) the model assumes that the fibre is accurately aligned with the input beam and it reproduces a reasonable fit to the experimental profile. However a much better fit is obtained when a small tilt is introduced into the model, as shown in figure 4.18 (b), where the input function G is tilted by 1.1°.

Figure 4.19 presents in solid lines the profiles obtained experimentally and in dotted lines those predicted by the model for several input f-ratios. In each case $D = 15 \times 10^{-5}$ m^{-1}, G is defined by the pinhole profile and tilted by 1.1°. The input f-ratios are indicated in each curve. The agreement between theory and experiment is very good for fast input f-ratios. As the input f-ratio increases the difference between the shape of

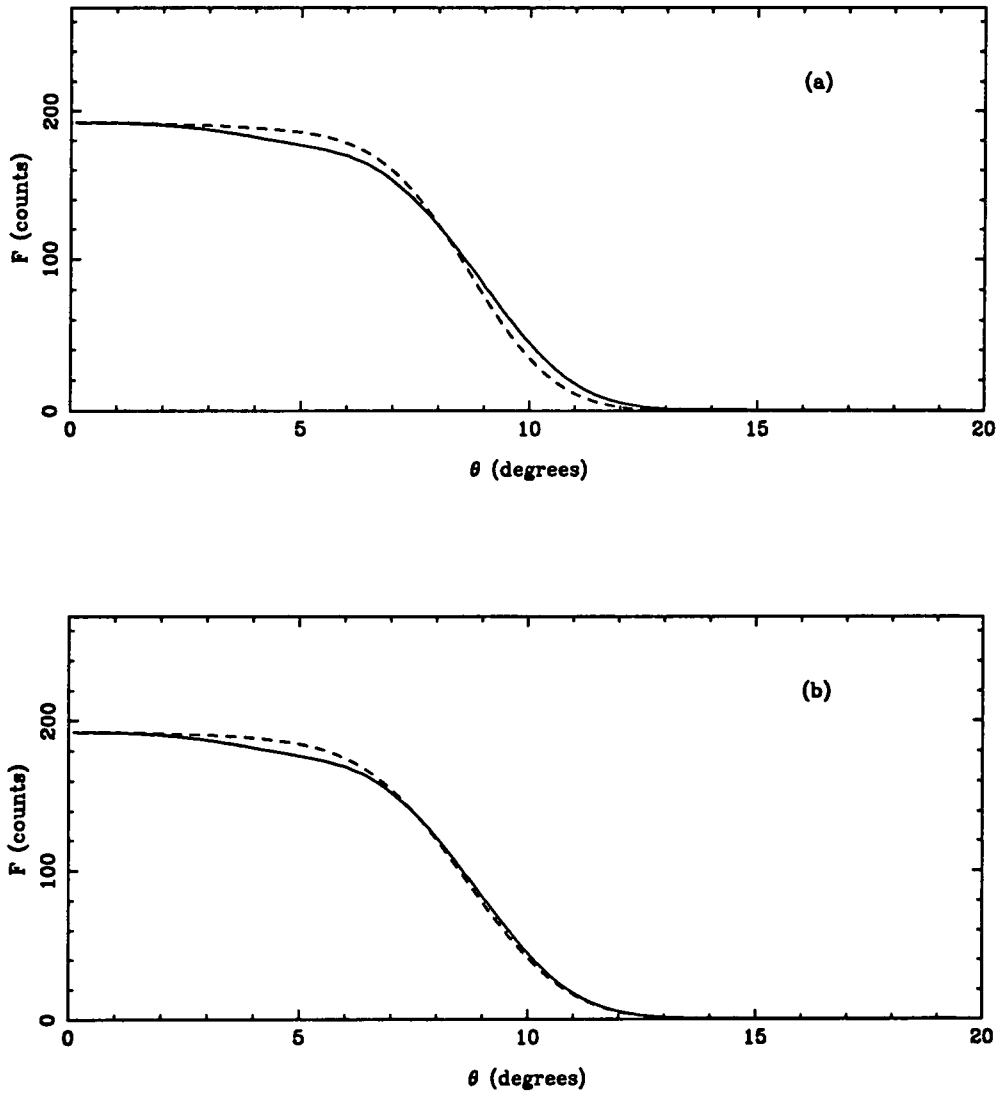

Figure 4.18. Far-field output profiles obtained for an f/2.8 input beam. The solid lines are the profiles obtained experimentally and the dotted lines correspond to the predictions by the model for a fibre with $L = 2$m and $D = 15 \times 10^{-5}$ m^{-1} . a)Predicted profile when the input function G is untilted. b) When G is tilted by 1.1°.

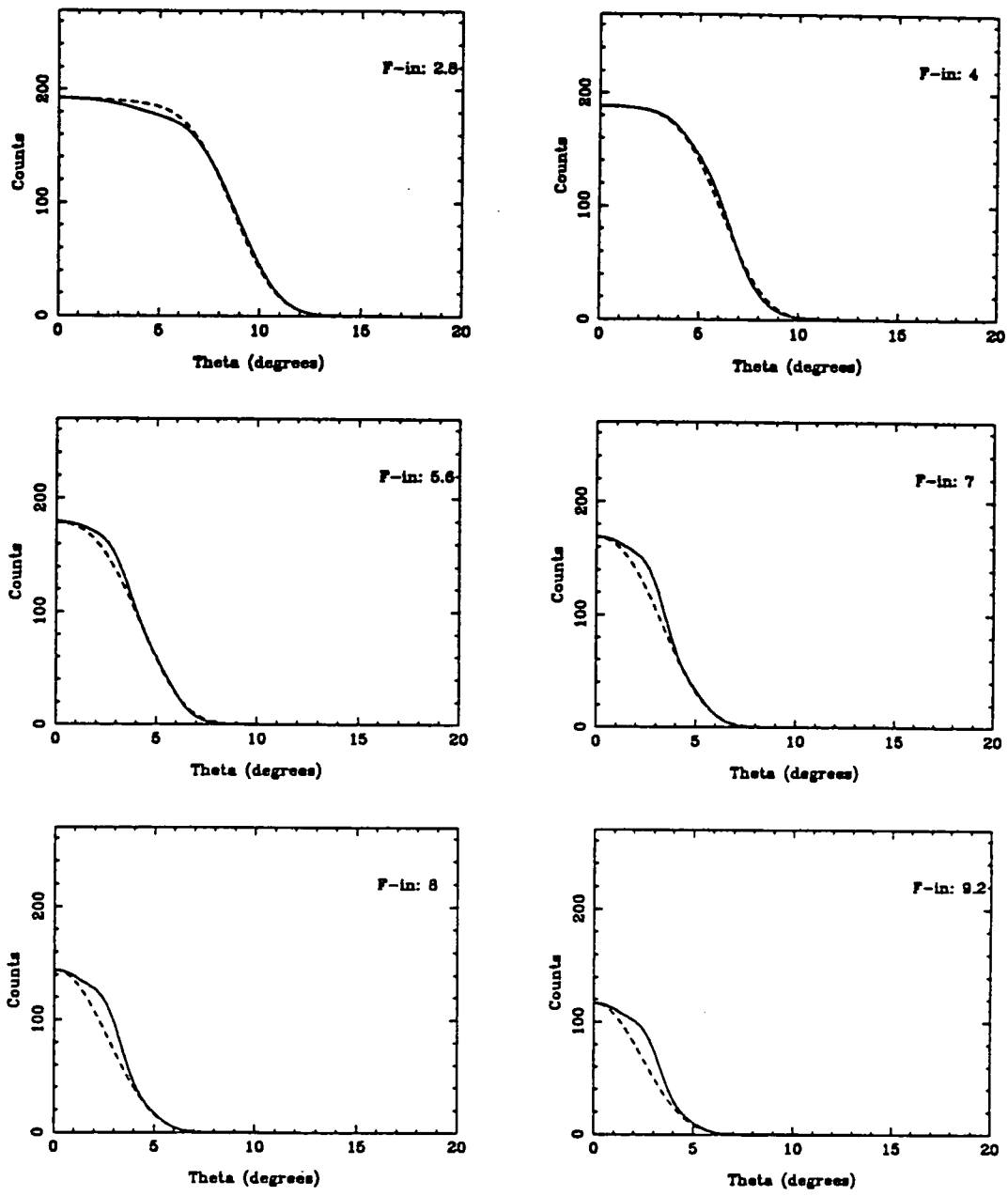

Figure 4.19. Far-field output profiles obtained for different input beams as indicated. The solid lines are the profiles obtained experimentally and the dotted lines correspond to the predictions by the model for a fibre with $L = 2$m and $D = 15 \times 10^{-5}$ m^{-1} and the input function G tilted by 1.1°.

the profiles increases slightly. Naturally, for slow input beams all the experimental errors become more critical, for example the semiangle subtended by an f/11 beam is only 2.6°. Nevertheless, these differences are not significant if we are interested in measuring the f-ratio of the output beam for which all the light is collected f_{out}, because this is estimated from the angle θ for which the profile reaches zero.

Figure 4.20 (a) shows a plot of f_{in} *vs.* f_{out} where the solid circles are the experimental results and the solid line represents the predictions by the model for a tilt of 1.1°. The average difference between them is 2.5% and is within the experimental errors. The dotted line which corresponds to the prediction without any tilt is shown for comparison. Clearly, the FRD performance of the test fibre is very poor in spite of the high quality of the end polishing. Stress induced by the epoxy might be responsible for such poor performance. Regardless of the fibre quality, the important point is that the model reproduces the experimental results.

The coefficient D was also found for a set of experimental results obtained by Barden (1987), who reports his results as plots of percentage of light contained within the output aperture, for different input apertures. For comparison purposes the output f-ratio is estimated from the point for which the curve becomes flat, for each of the input f-ratios. A graph of f_{in} *vs.* f_{out} is shown in figure 4.20 (b). The solid circles are the data derived from Barden's results for a fibre 31.7m long, manufactured by Polymicro Technologies (FLP320385415). The curve corresponds to the prediction from the model for $L = 31.7$m and $D = 0.04 \times 10^{-5}$ m^{-1}. The agreement between theory and experiment is not as good as in the previous case and this maybe because the input function G is unknown. It was simply assumed that G was a step function. However, these results allow us to determine the value of the parameter D that characterises a very good fibre.

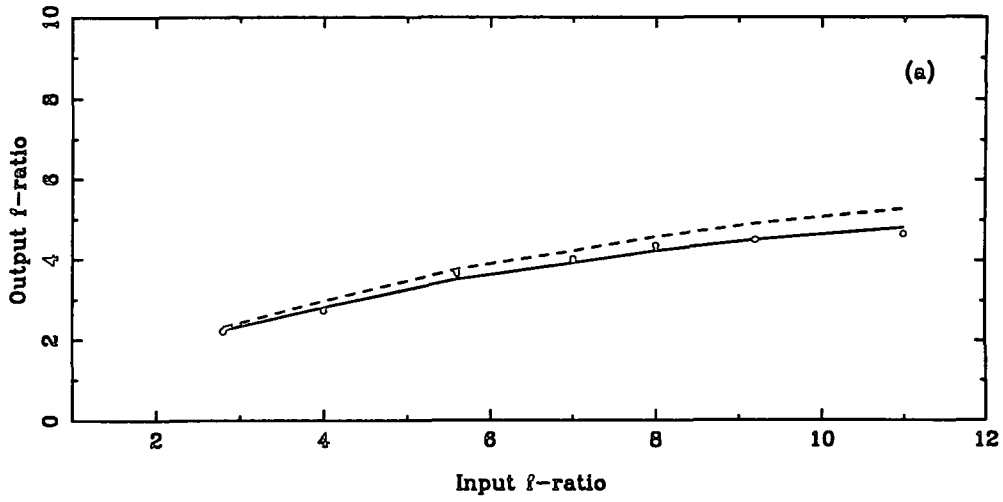

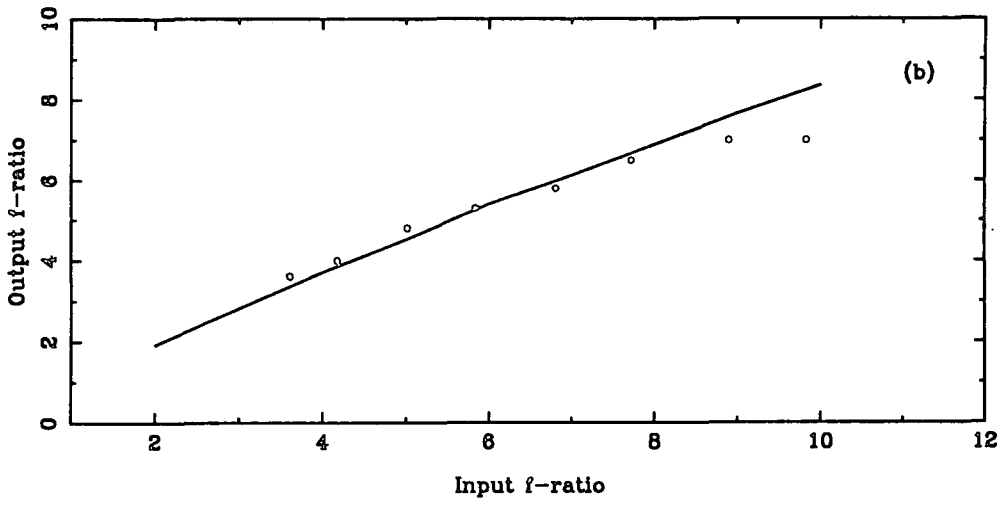

Figure 4.20. a)The FRD curve for the test fibre. The solid circles are the experimental results and the curve is the prediction by the model for a fibre with $L = 2$m and $D = 15 \times 10^{-5}$ m^{-1} when the input function G is tilted by 1.1°. The dotted line corresponds to the predictions when G is untilted. b) The FRD curve of a very good fibre. The solid circles are data derived from the results reported by Barden (1987) for a fibre 31.7m long. The curve corresponds to the predictions by the model for a fibre with $L = 31.7$m and $D = 0.04 \times 10^{-5}$ m^{-1}.

4.6 Conclusions

The experiments described in this chapter illustrate several aspects of fibre evaluation techniques. The results obtained with the four methods are consistent which proves the reliability of these techniques. From the results presented in the previous sections the following procedure to measure the FRD of any fibre is proposed.

- First, the parameter D that characterises the fibre in terms of microbending, is determined using a simple laser experiment.

- Then, the FRD performance can be predicted from equation 3.30 using the value of D obtained via the laser experiment and the function G which describes the input beam.

The determination of D via a laser experiment is very straightforward and the experimental setup is much simpler than in the case of the image experiment described in section 4.2. In the latter case there are many potential sources of errors such as alignment, calibration of the iris, stability of the light source and the detector, among others. Consider for example the case of the results shown in figure 4.2. It was attempted to have a fairly uniform input beam using a diffuser, however from the pinhole profile shown in the figure it is clear that it is not a step function. Also the perpendicularity of the fibre end with respect to the optical axis is critical as any tilt gives an overestimation of the FRD. Although some of these errors can be analysed by the reduction software, it takes time to obtain the results and then to correct the misalignments. Furthermore the complexity of the experiment requires a complicated data reduction package to analyse the results.

The good agreement between model and experiment confirms the validity of the proposed method. Nevertheless, it is apparent that the model must be tested against more experimental data. Furthermore, microbending induced beamspreading is only one physical mechanism which gives rise to FRD. End preparation and individual stress points

are other possible sources of FRD and the model should account for these as well. A full physical theory for all FRD sources could therefore be developed. Alternatively, a simple empirical model could be used to parameterise the FRD performance. Finally, it is important to remark that according to equation 3.25 the parameter D depends on the wavelength of the incident light. The extent of this dependence must be investigated in fibres for which microbending is the dominant cause of FRD.

In summary, it is proposed that the complete performance of any fibre can be modelled by using theory and the appropriate value of a parameter determined by a very simple experiment. Such modelling can include complicated phenomena such as tilted input beams and central obstructions and will produce reliable predictions without the need to set up experiments for specific cases. The use of a simple parameter to characterise FRD performance will allow different workers in the field to compare results much more easily. Furthermore it will make the fibre throughput measurements practical for an instrument with hundreds of fibres.

5 THE LABORATORY EVALUATION OF THE AUTOFIB-1.5 FIBRE BUNDLE

5.1 Introduction

Autofib-1.5 was built as a prototype for Autofib-2 and it incorporates many new ideas relevant to new instrumentation. One such idea is a multiway connector incorporated into the Autofib-1.5 fibre bundle. This chapter describes the laboratory evaluation of this bundle with the emphasis being placed on the performance of the connector.

The new generation of multiobject instruments will use hundreds of fibres, which will have to feed different spectrographs. Therefore it is an important practical requirement to have a reliable and safe way to route the fibres between the telescope and the spectrographs during the observations and to keep the fibres in a safe place at all other times. The exposure of the fibre bundle to unnecessary stress or possible breakdown will degrade the long-term performance of a multifibre system. A good example of an instrument which requires an efficient optical fibre connector is Autofib-2 for the WHT. Autofib-2's fibres have to feed light from the prime focus to a spectrograph permanently mounted at Nasmyth. Since Autofib-2 has to be removed to use other instruments a connector in the 25m fibre bundle greatly eases instrument changes.

The main difficulties with joining fibres together arise from the small core diameters, of approximately 100μm, that must be accurately aligned. The commonest method involves holding the ends in mechanical contact. An efficient connector requires that the

ends of the fibres be prepared in such a way that, with suitable index matching, the propagating light beam will not be deflected or scattered at the fibre interface and that the two ends to be connected can be brought into close proximity. In practice this means that the ends must be flat, perpendicular to the fibre axis and fairly smooth.

The communication industry has developed connectors (*e.g.* ST-II connectors) that can achieve median transmission losses as low as 0.13 dB (97% transmission). Unfortunately such connectors are only available for standard fibre sizes and not in a multifibre format. The need for a multifibre connector suitable for astronomical applications, where the fibre's size depends of the plate scale at the focal plane of the telescope led to the design of a 64-way connector prototype to be incorporated into the automated multifibre system Autofib-1.5. This instrument has been described in some detail by Parry and Lewis (1990). Briefly, it is an automated fibre system in which all the fibres are moved individually by the same robot positioner, then held in place on a steel field plate by small permanent magnets. The main part of the instrument consists of two subsystems stacked one of top of the other, one containing the robotic positioner and the other a fibre module containing the fibres and field plate.

This chapter describes the evaluation undertaken to measure the overall performance of the Autofib-1.5 fibre bundle and determine the contribution made by the connector. The geometry of the connector is described in section 5.2. Section 5.3 describes the alignment measurements. In section 5.4 the results of the throughput measurements of the fibre bundle are presented. Section 5.5 describes the results of the visual inspection of the four end faces of each fibre. In section 5.6 FRD measurements carried out with different experimental setups for a sample of fibres are presented. Finally, section 5.7 includes a summary of the results and the conclusions.

5.2 Connector description

Figure 5.1 shows a diagram of the 64-way connector prototype. One half of the connector is fixed underneath the fibre module while the other is mounted on the end of the fibre bundle's protective flexible conduit. The connection is made quickly and simply by aligning the dowels and tightening the threaded locking ring by hand.

A detailed description of the connector manufacture process is given by Lewis (1991). Briefly, to achieve good alignment between the two halves of the connector the matching faces were originally a single aluminum disk. 64 1.1mm holes were drilled through the disk in an 8×8 array on 2mm centres. In addition near the edge of the disk two 3.0mm holes were drilled and reamed to take the alignment dowels. Once drilled, the disk was cleaned, and two concentric stainless steel tubes were epoxied into each of the 64 holes, to reduce the bore to 320μm and match the 315μm outside diameter of the fibres.

Subsequently, the whole disk was sliced into two halves perpendicular to the tubes and cleaned in an ultrasonic bath. The fibres were then epoxied into the tubes using a low viscosity epoxy (TRA-BOND BA-F1135C) with a curing time of approximately 24 hours. The low viscosity was required to ensure that sufficient epoxy penetrated inside the close-fitting tubing.

The connector shell was assembled around the aluminum disk to protect the fibres and the projecting fibres were trimmed to within 0.5mm of the face of the connector using a sapphire cleaving tool. Then the whole connector face was polished, using aluminum oxide papers of different grades (30, 9, 3, 1 & 0.3 μm) supported on a piece of float glass. The polishing process was carefully performed by hand. Extreme care was taken to ensure that the axis of the connector remanded perpendicular to the polishing surfaces. Figure 5.2 shows one half of the completed and assembled connector.

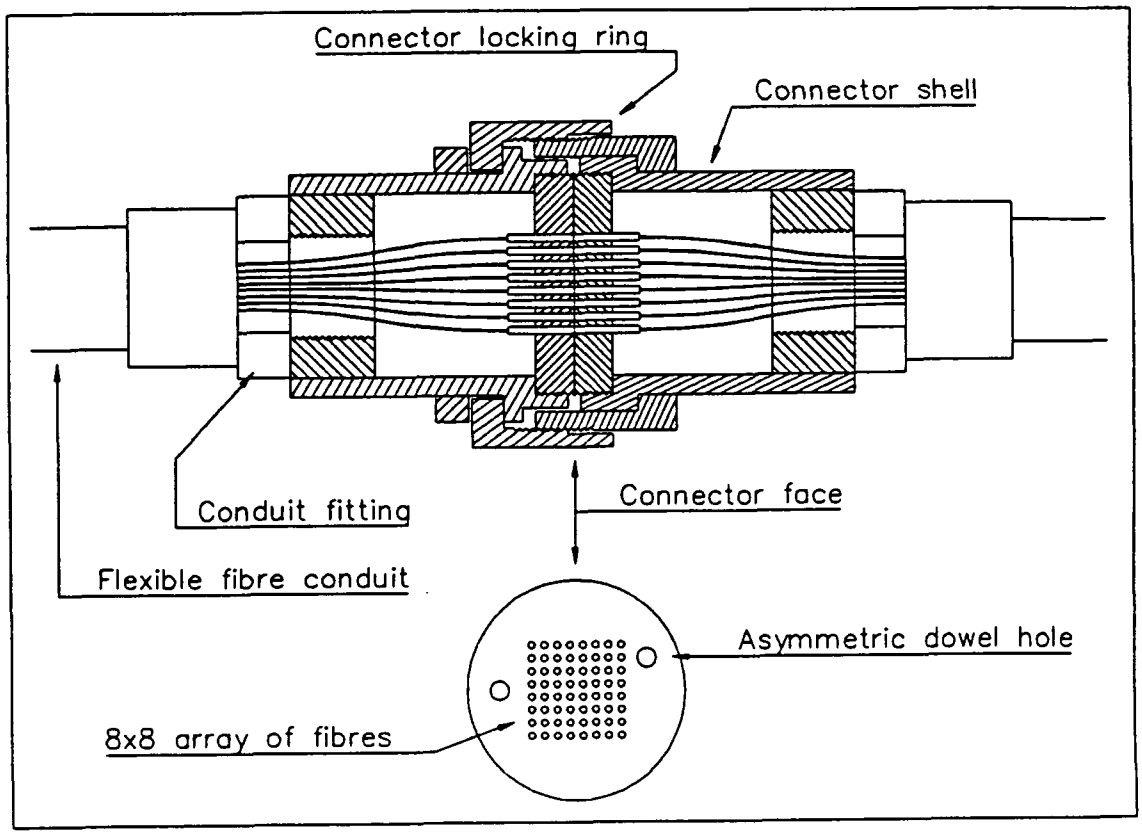

Figure 5.1. Diagram of the 64-way connector prototype.

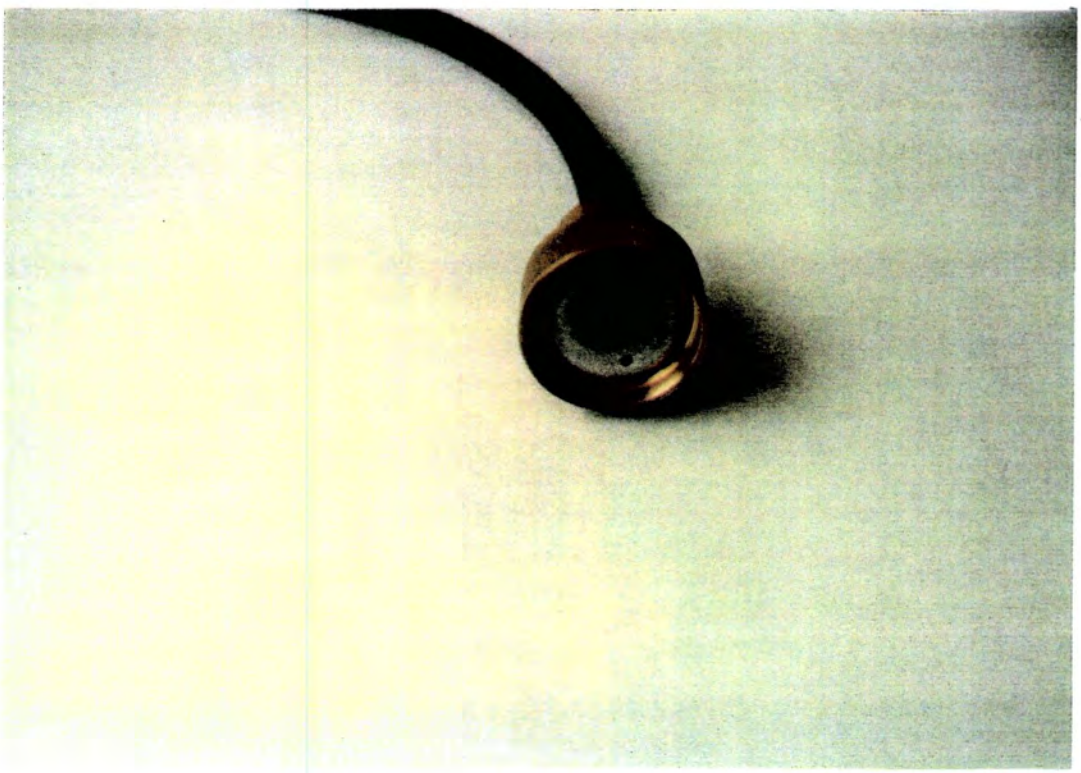

Figure 5.2. Photograph showing one half of the completed and assembled connector.

5.3 The alignment between the two faces of the connector

To investigate the alignment between the two connector faces the positions of all the fibres have to be measured using a suitable XY measuring machine. However, because the two sets of measurements for each face have different zero points, are mirror images of each other and may be rotated with respect to each other it is necessary to apply a coordinate transformation to one set of the measurements before individual fibre misalignments can be assessed. A least squares transformation minimises the misalignments and gives a good estimate of the misalignments that occur in practice.

Consider a grid of points defined in a coordinate system XY. Let $X'Y'$ be another coordinate system rotated by an angle $-\alpha$ with respect to the system XY. Let δx and δy be the translation between the coordinate systems $X'Y'$ and XY in the x and y-directions respectively. δx and δy are measured in the system $X'Y'$. The coordinates (x,y) of a given point in the system XY are related to its coordinates (x', y') in the system $X'Y'$ as follows,

$$x' = x\cos\alpha + y\sin\alpha + \delta x \tag{5.1}$$

$$y' = -x\sin\alpha + y\cos\alpha + \delta y \tag{5.2}$$

If the two faces of the connector match each other and the experimental measurements are in the same coordinate system then $\alpha = 0$ and $\delta x = \delta y = 0$. In practice, however this is not the case and we must find $\alpha, \delta x$ and δy by minimizing the rms errors Δ^2 between one face and the transformation of the second one, where

$$\Delta^2 = \Sigma\Big[(x_i' - x_i\cos\alpha - y_i\sin\alpha - \delta x)^2 + (y_i' + x_i\sin\alpha - y_i\cos\alpha - \delta y)^2\Big] \tag{5.3}$$

From the conditions $(\partial\Delta^2/\partial x) = 0$, $(\partial\Delta^2/\partial y) = 0$ and $(\partial\Delta^2/\partial\alpha) = 0$ the following relationships are obtained,

$$\tan\alpha = \frac{< x_i' y_i > - < x_i' >< y_i > - < x_i y_i' > + < x_i >< y_i' >}{< x_i' x_i > - < x_i' >< x_i > + < y_i' y_i > - < y_i' >< y_i >} \tag{5.4}$$

$$\delta x =< x_i' > - < x_i > \cos\alpha - < y_i > \sin\alpha \tag{5.5}$$

$$\delta y =< y_i' > - < y_i > \cos\alpha + < x_i > \sin\alpha \tag{5.6}$$

Therefore the shift and rotation between the two sets of measurements for the two faces of the connector can be estimated from equations 5.4 to 5.6.

The accuracy of the drilling process was estimated from measurements of the position of 16 holes on the front and back faces of a trial disk before it was sliced in two. The thickness of the disk was 15mm. For each face a particular hole was chosen as a reference and all the measurements were made relative to it. The centre position of the reference hole defined the origin of the coordinates systems XY and $X'Y'$. A measuring machine with a resolution of $\pm 5\mu$m was used.

When compared with a theoretical set of perfect holes, the holes on the face where the drill entered showed small errors $< 10\mu$m. However on the face where the drill exited the material, the errors were significantly worse (57μm). This value is the median of $\sqrt{x^2 + y^2}$, where x and y are the residuals after the transformation was applied. In an attempt to diminish this effect the disk used in the Autofib-1.5 connector had a reduced thickness of 10mm in the area of drilling. The amount of drill 'wander' does not affect a connector in which the two halves of the connector are made by slicing a single disk

in two. However, if we require a connector that can be efficiently coupled to many other similar connectors then the accuracy of the drilling process is crucial and it was with this in mind that the drilling errors were investigated.

5.3.1 Connector alignment measurements

Once the connector was finished and assembled the positions of the fibres in each face were measured to find out the magnitude of the lateral misalignments. An optical system consisting of a microscope and a CCD camera, mounted on an x-y micrometer stage was used to measure the position of the fibres in the half of the connector in the fibre module. A similar system was used to measure the position of the fibres in the other face of the connector. The measurement accuracy was $\pm 10\mu$m.

An appropriate least squares transformation to the results of each face was applied using equations 5.4 to 5.6 to ensure that the individual hole positions to be compared were defined in the same coordinates system. The results for the individual fibres are shown in figure 5.3 (a). The shift was calculated from the x and y misalignments as $\sqrt{x^2 + y^2}$. The median error is 50μm. The distribution of the shifts is shown in figure 5.3 (b). Figure 5.3 (c) shows the square of the shifts because in the ideal case of random errors the distribution of $x^2 + y^2$ should be an exponential (χ^2 with two degrees of freedom). The distribution found follows an exponential as a crude approximation, however it should be noticed that there are not enough points to fit a curve to this distribution. On the other hand the distribution of the x-values do follow a gaussian —as expected in the ideal case of pure random errors, while that of the y-values departs from a gaussian distribution implying that the relative shifts are not purely random.

Although the shift between fibre ends gives an indication of the losses, a quantitative estimation of the transmission losses is more useful. The transmission losses due to

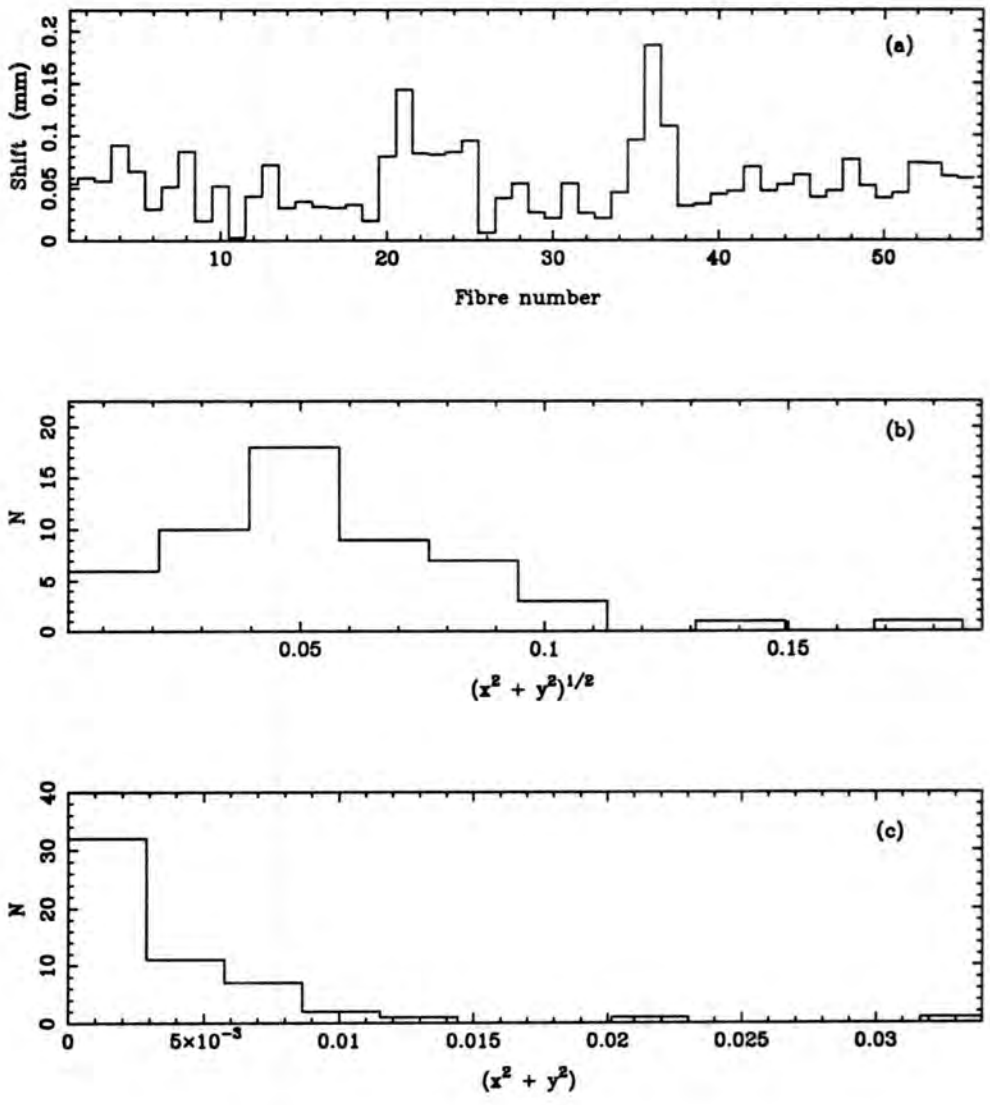

Figure 5.3. a) Lateral misalignment errors between the positions of the individual fibres in each face of the connector. The values were calculated from the x and y misalignment as $\sqrt{x^2 + y^2}$. b) Error distribution of $\sqrt{x^2 + y^2}$. c) Error distribution of $x^2 + y^2$.

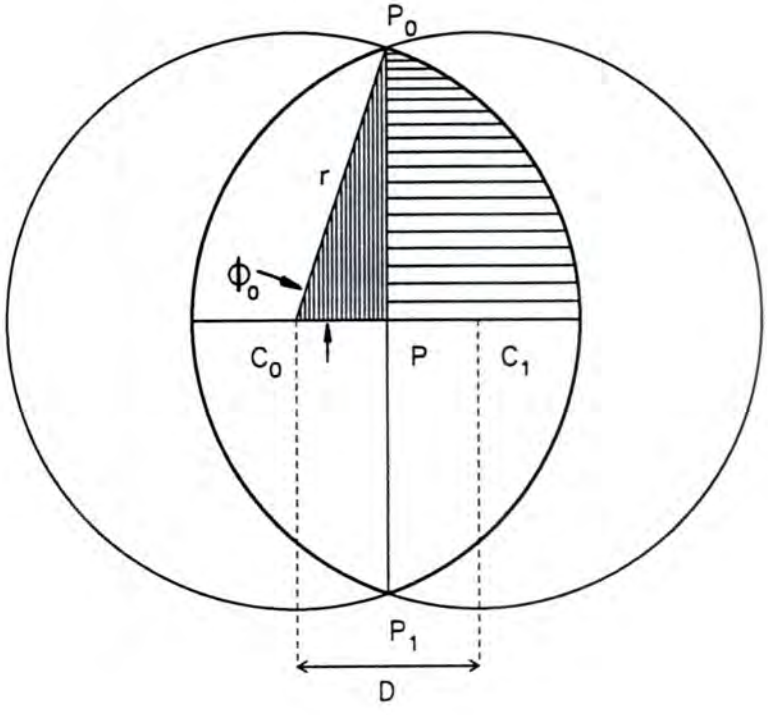

Figure 5.4. Sketch to calculate the misalignment losses between two fibre cores of radius r, shifted by a distance D. The transmission efficiency is the ratio of the area of intersection of the two circles to the area of a single circle.

misalignments depend on a knowledge of the power distribution across the fibre faces. It is possible to obtain an approximation assuming that the radiation is evenly distributed across the core cross-section. Consider the situation shown in figure 5.4, a fibre end of core radius r is shifted, by a distance D, with respect to another fibre end. The problem is to find the area of intersection between the surfaces. As indicated in the figure, this area can be divided in four equal parts by tracing a line P_0P_1 that bisects the area and another line through the centres of the circles C_0 and C_1, perpendicular to P_0P_1. Thus, it is enough to calculate the area of one section shown hatched with horizontal lines and then multiply by four.

The distance between point C_0 and P_0 is equal to the radius r. The distance between C_0 and P_0P_1 is $D/2$. Let $\phi_0 = \cos^{-1}(D/2r)$ the angle subtended by the arc formed by $P_0C_0C_1$. The area of a sector of angle ϕ_0 is given by:

$$S_1 = \int_0^{\phi_0} \int_0^r RdRd\phi = \frac{r^2}{2}\cos^{-1}(D/2r) \tag{5.7}$$

The area S_0 of the triangle PC_0P_0, shown hatched with vertical lines, is simply:

$$S_0 = \frac{D}{4}\sqrt{r^2 - D^2/4} \tag{5.8}$$

The total intersection area will be $A_i = 4(S_1 - S_0)$, *i.e.*

$$A_i = 2r^2\cos^{-1}(D/2r) - rD\sqrt{1-(D/2r)^2} \tag{5.9}$$

For comparison purposes it is convenient to divide A_i by the area of the core $A_t = \pi r^2$, thus

$$\frac{A_i}{A_t} = \frac{2}{\pi}(\cos^{-1}\delta - \delta\sqrt{1-\delta^2}) \tag{5.10}$$

where $\delta = D/2r$. This expression gives us the ratio of the intersection area and the total area as a function of the offset misalignment parameter δ. The transmission, defined as the power P_i of the intersection area divided by the total power P_t across the fibre core, assuming that the power distribution is uniform across the fibre core, is then given by:

$$T = \frac{P_i}{P_t} = \frac{A_i}{A_t} \tag{5.11}$$

Figure 5.5 shows a plot of the transmission as a function of δ. Consider now the mean misalignment between the connector faces described previously. An average shift of 50μm, divided by the fibre core diameter 260μm gives $\delta = 0.192$ and the transmission will be $T = 75\%$.

5.4 The throughput measurements

Ideally, to measure the losses in a multifibre connector, the fibre efficiency should be measured before and after the connector is introduced into the system. However, in this particular case the connector was incorporated as part of Autofib-1.5 before the efficiency of the fibres was measured. Thus, the performance of the connector was estimated by measuring the throughput of the 14m long fibres from the connector interface to the slit (the conduit section) and then by repeating the measurements for all the fibres, with the connector attached to Autofib-1.5, from the prism to the slit as shown in figure 5.6. The results do not provide a number for the losses due to the connector in absolute terms but

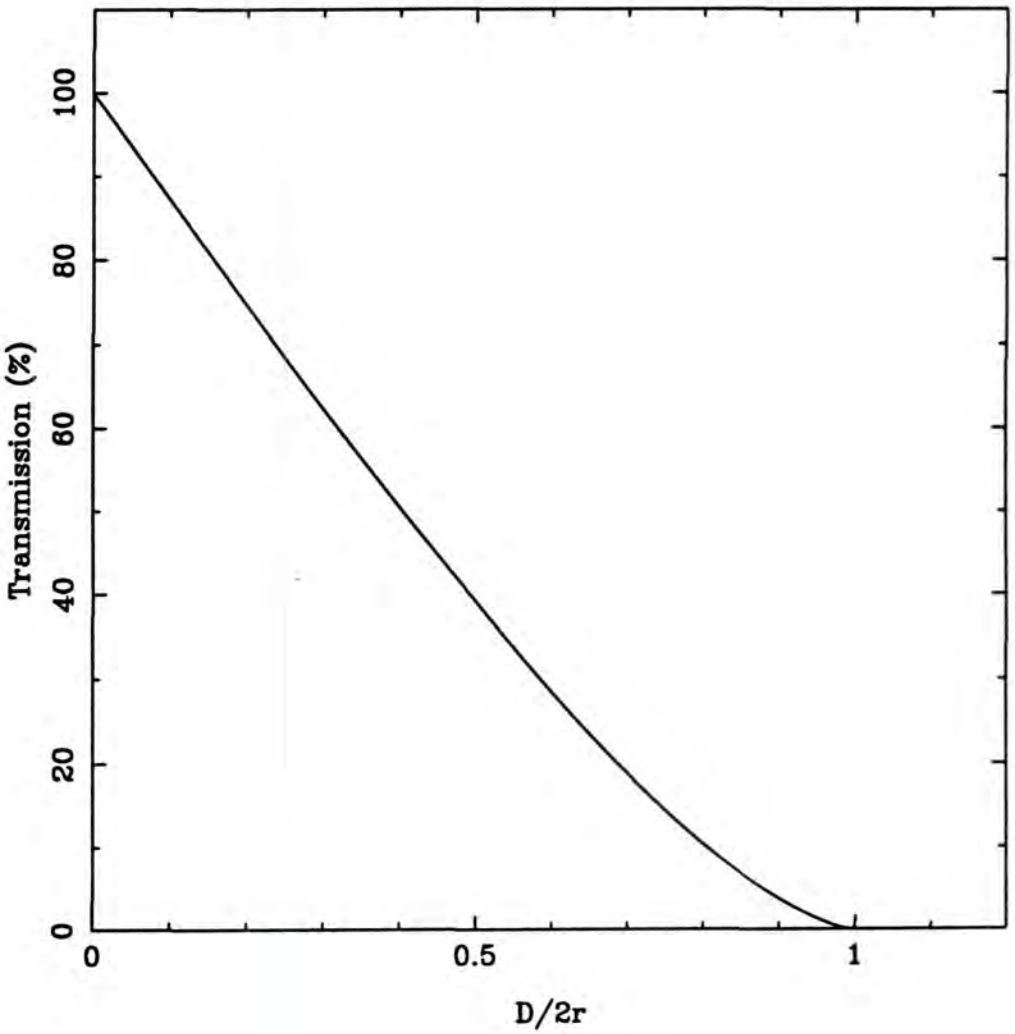

Figure 5.5. Transmission as a function of the misalignment parameter $\delta = D/2r$, where r is the radius of the fibre core and D is the lateral offset between the two fibre cores to be coupled.

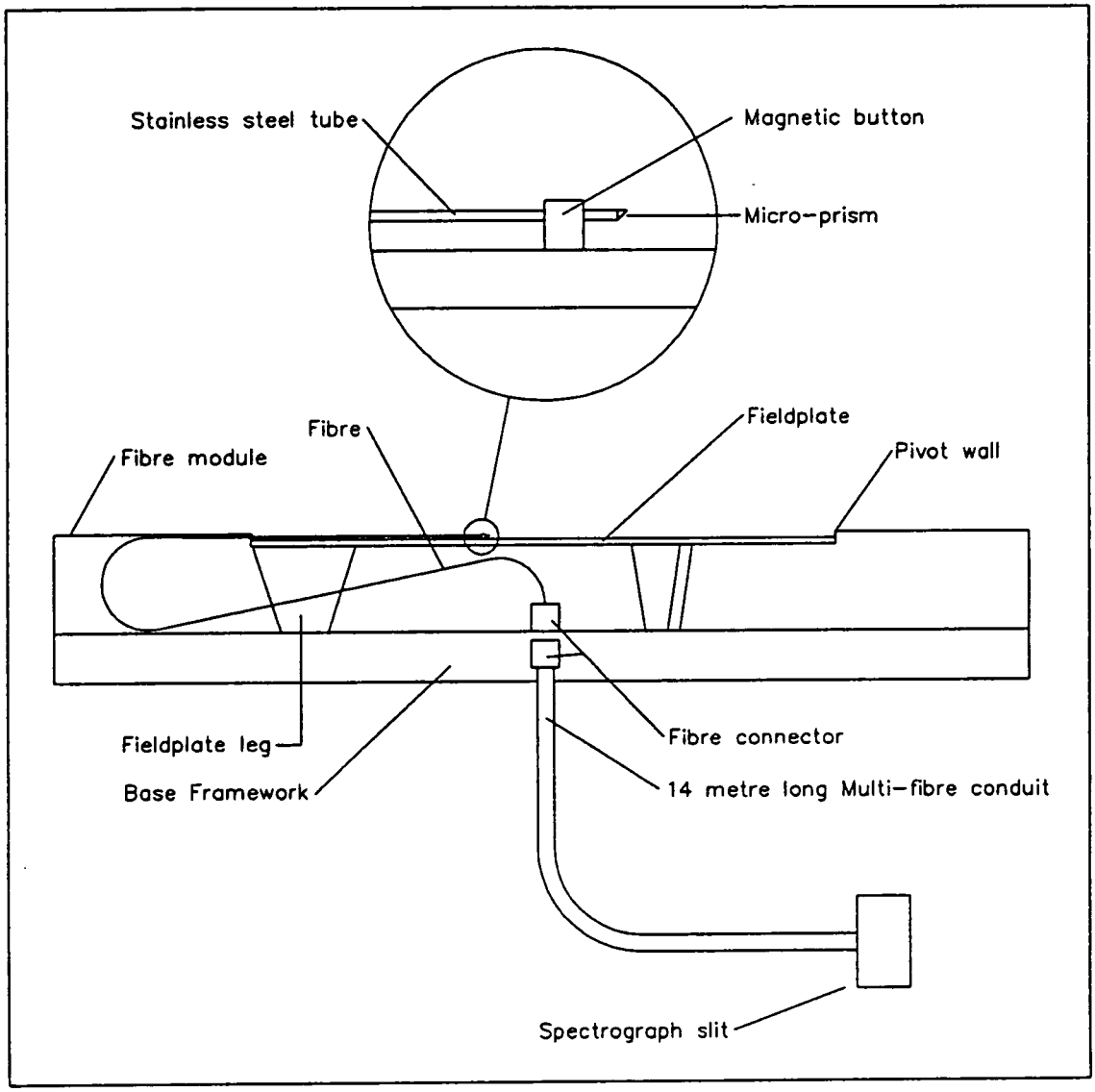

Figure 5.6. Schematic of the fibre bundle. The performance of the connector was estimated by measuring the throughput of the fibres from the connector interface to the slit and then by repeating the measurements with the connector attached to Autofib-1.5, from the prism to the slit.

do provide useful information of the relative fibre performance in the system in terms of throughput and FRD.

The experimental setup, called the photodiode experiment was described in detail in chapter 4 (§4.3) and is shown in figure 4.10. Briefly, light from a tungsten lamp is transferred to the input of the optical system via an auxiliary fibre. An image of the fibre is formed by a system of two lenses and an aperture stop that defines an f/11 input beam such as for the Cassegrain focus of the WHT. The output optical setup is formed by another system of two lenses that focus the fibre output end onto a photodiode. The output focal ratio is defined by an iris positioned between the two lenses. No filter was used in this experiment.

5.4.1 The throughput of the fibres in the conduit

The connector was mounted on an x-y micrometer stage so that each fibre in the connector could be aligned in turn with the input beam. The output optical arrangement was fixed directly to the optical table. Figure 5.7 shows photographs of the experimental setup used in this series of measurements. For the throughput evaluation for each fibre two measurements were made —one of the Autofib-1.5 fibre and the other of the reference fibre. The purpose of the latter measurement was to monitor any drifts in the illumination.

To avoid introducing errors by changing the output iris aperture, a set of measurements was made for the complete array of 55 fibres at a given aperture. The output f-ratios chosen were f/4.7 and f/11.2, the former corresponded to the maximum iris aperture while f/11.2 was chosen to match the input f-ratio. The throughput was determined with an accuracy of about 3%.

Figure 5.8 (a) shows the absolute throughput at an f/4.7 output ratio for the complete set of fibres while in figure 5.8 (b) the results obtained at f/11.2 are shown. The

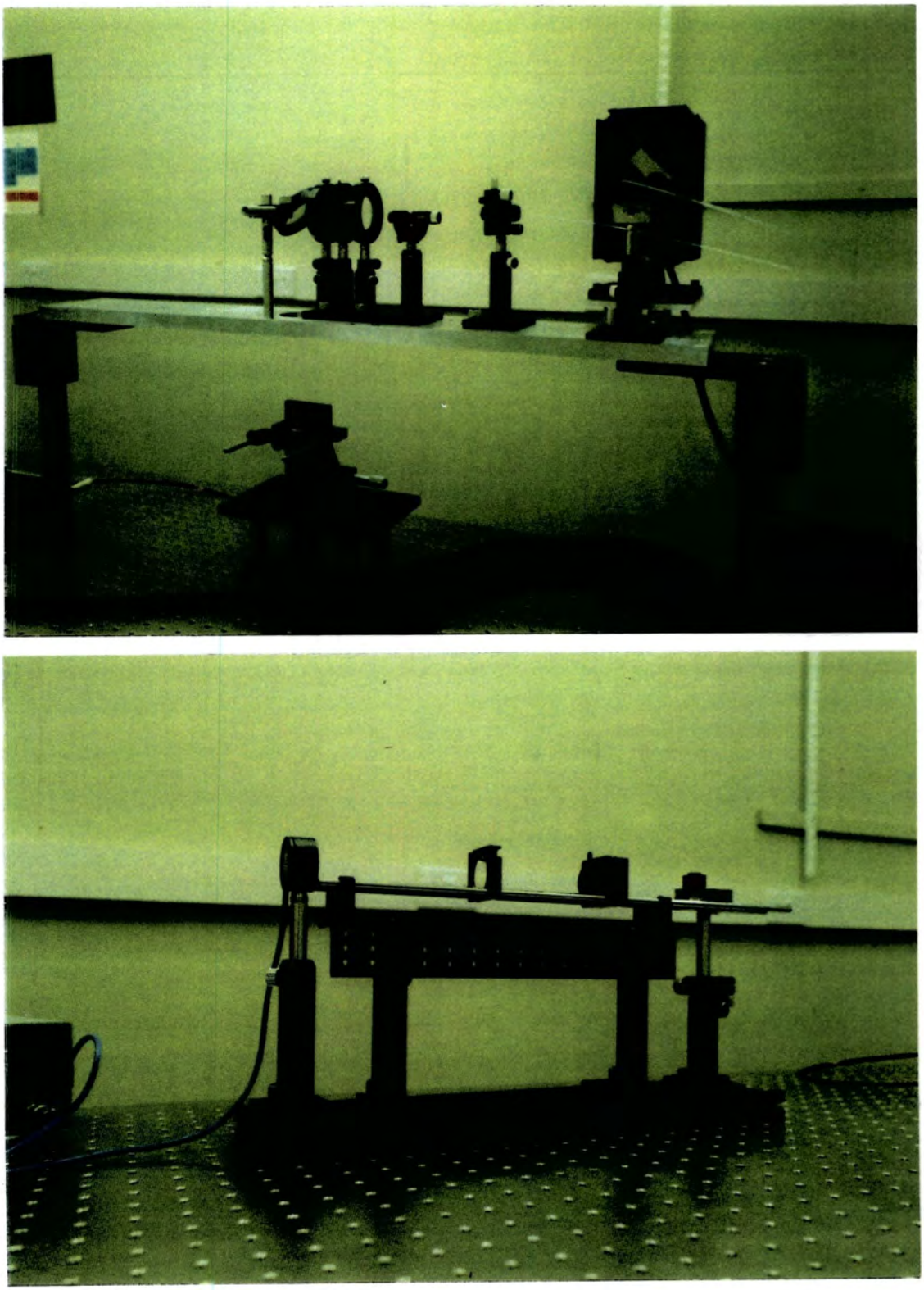

Figure 5.7. Photographs of the equipment used to measure the throughput of the fibres in the conduit. Top: the optical arrangement at the fibre input. Bottom: the optical arrangement at the fibre output.

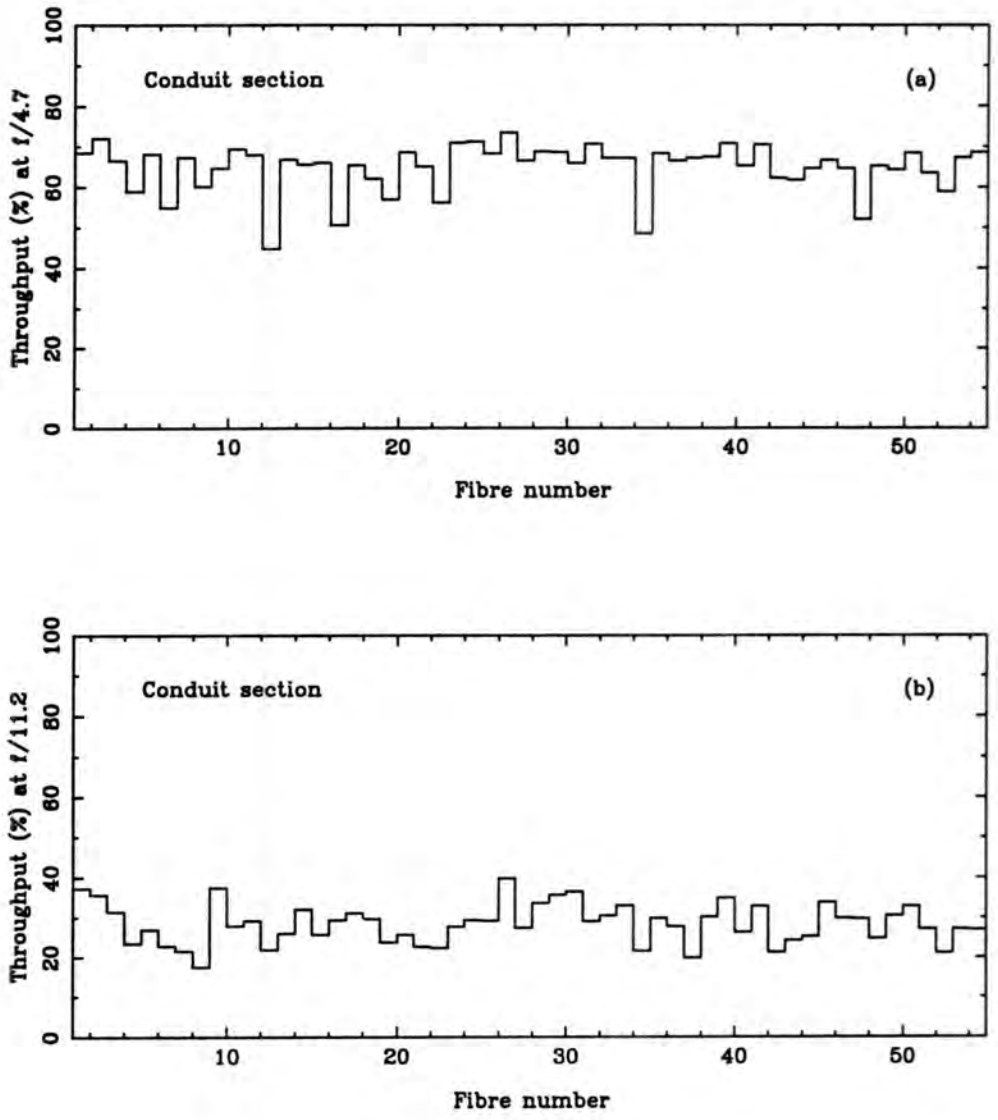

Figure 5.8. Absolute throughput of the fibres in the conduit obtained at an f/11 input beam. a) At an f/4.7 output f-ratio. The mean throughput is 65%. b) At an f/11.2 output f-ratio. The mean throughput is 28%.

mean throughput value in the former case is 65% ± 6% and in the latter one is 28% ± 5%. It should be noticed that these measurements are only for the fibre bundle from the connector interface to the slit, therefore losses due to the connection between the two faces of the connector are not included. The average performance is fairly poor considering the high transmission characteristics of this type of fibre. If the losses were exclusively due to Fresnel reflection (8%) and absorption (5%, see figure 4.6) an average throughput of about 87% would be expected. The results at f/11.2 show clearly that at slow input f-ratios such as f/11.2 the FRD is severe, as has been discussed in chapter 3 (§3.7.3). Nevertheless, in absolute terms the losses are very high in our case.

The dispersion in the results with respect to the mean value is dominated by the differences in the quality of the preparation of the fibre ends as a result of a poor polishing process. Also other factors, such as stress induced by the epoxy when the fibres are glued in the tubes, as discussed by Barden (1987), contribute to the increase in the losses at slow f-ratios.

5.4.2 The throughput of the complete Autofib-1.5 bundle

To measure the overall performance of the Autofib-1.5 fibres the conduit was connected to the fibre module of Autofib-1.5. An index matching gel was applied between the two faces of the connector. The input optical system bench was rigidly attached on top of Autofib-1.5 at the same height as it was from the connector's face in the first stage. Figure 5.9 shows photographs of the equipment used in this experiment.

For throughput measurements each fibre was moved to the centre of Autofib's field plate using the control software. Two measurements were obtained, one of the Autofib fibre and the other of the reference fibre. The purpose of the second measurement was to monitor any drifts in the illumination. A set of throughput measurements was made for

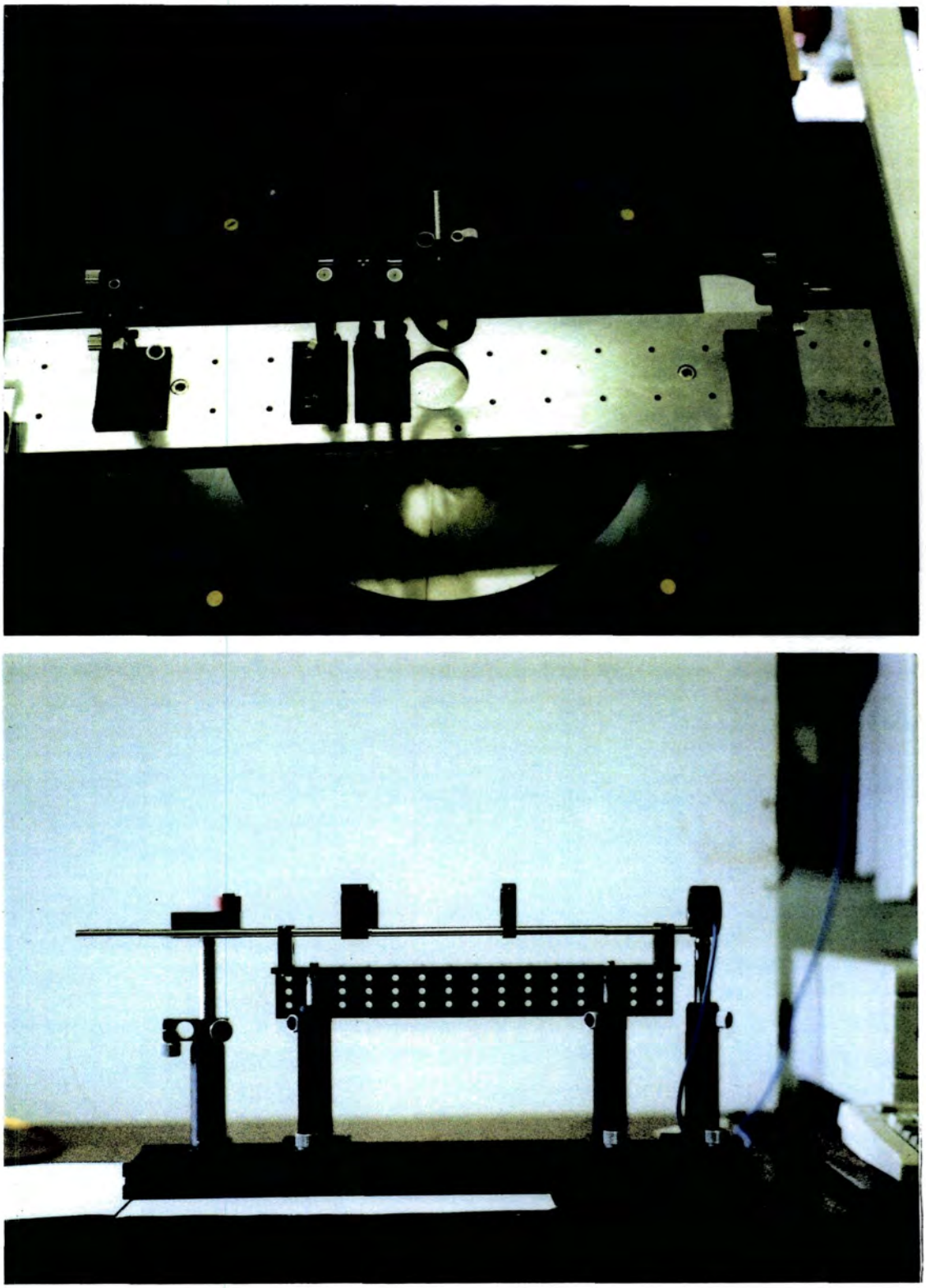

Figure 5.9. Photographs of the equipment used to measure the throughput of the complete Autofib-1.5 fibre bundle. Top: the optical arrangement at the fibre input. Bottom: The optical arrangement at the fibre output.

the complete set of 55 fibres at the same output f-ratios as before *i.e.* at f/4.7 and f/11.2. The effect of the index matching gel on the throughput results was tested by repeating a few measurements with the gel removed.

The stability of the whole experiment was estimated by repeating throughput measurements of fibre No. 2. Possible sources of non-repeatability include the Autofib-1.5 positioning errors and the errors in the position of the fibre output end in the V-groove. One repetition of the fibre 2 measurement was carried out for every 5 other fibres measured. The error, calculated as the standard deviation divided by the mean, was 3.4%. The variations of the tungsten lamp were calculated by measuring the reference fibre throughput as a function of time. The error introduced by these variations, defined as above, was 2.3%. The repeatability was better than 4%, which is about equal to the rms value of the two errors mentioned.

Figure 5.10 (a) shows the absolute throughput results at an f/4.7 output ratio for the complete set of fibres, where the mean value is 60% ± 12%. Figure 5.10 (b) shows the corresponding results at f/11.2, the throughput mean value in this case is 17.2% ± 6%. These results should be compared with those obtained for the conduit section on its own *i.e.* 65% at f/4.7 and 28% at f/11.2.

A mean throughput value of 60% at maximum aperture indicates high losses, however it should be noticed that some fibres present efficiencies better than 75%. If the output f-ratio is to be restricted to that of the input the light losses are very high. Nevertheless, Autofib-1.5 has been used in combination with the FLEX spectrograph designed for an f/8 input beam, therefore the losses on the telescope are smaller (see §5.4.4).

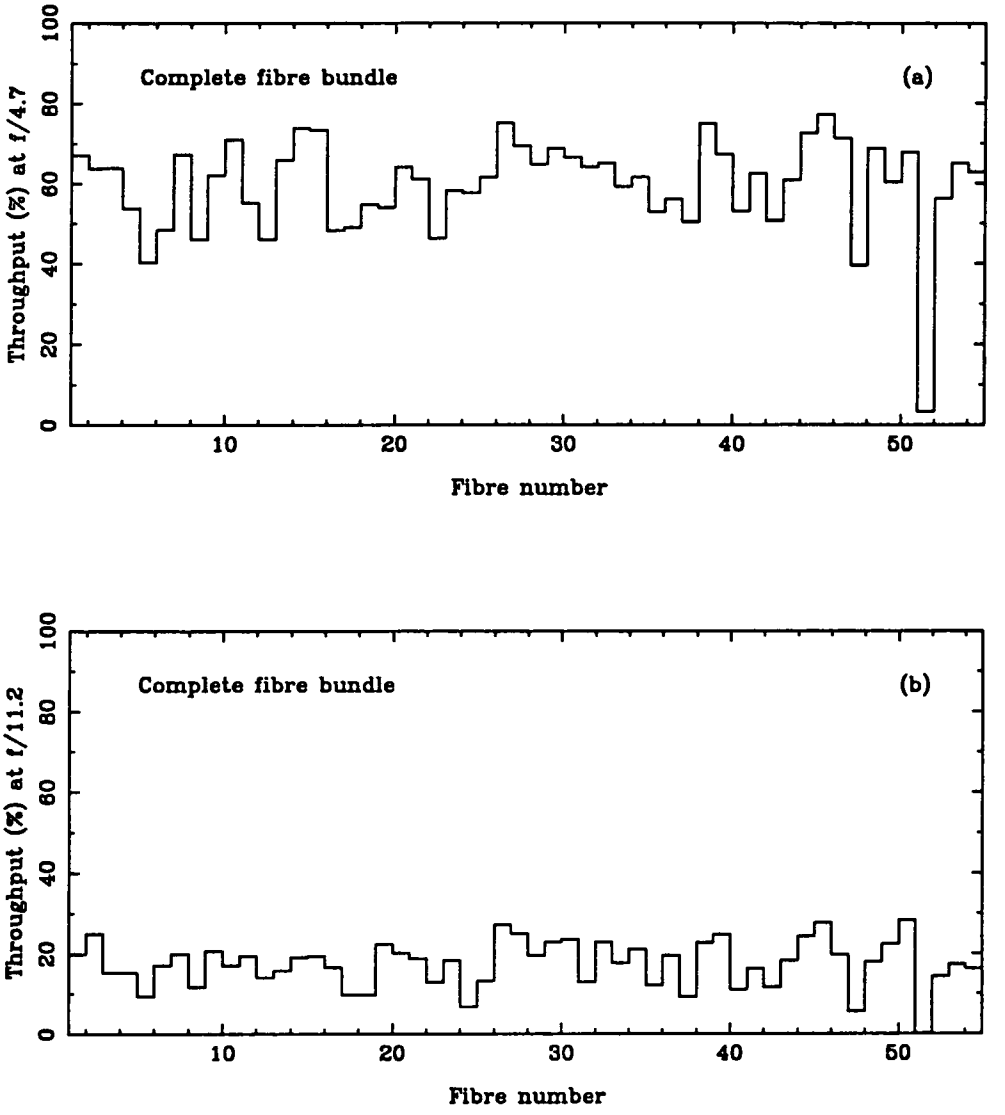

Figure 5.10. Absolute throughput of the complete Autofib-1.5 fibres, including the connector, for an f/11 input beam. a) At an output f-ratio of f/4.7. The mean throughput is 60%. b) At an output f-ratio of f/11.2. The mean throughput is 17%.

5.4.3 Discussion of the connector performance

To evaluate the performance of the connector, the results presented in the last two section must be compared. Consider the results obtained at an f/4.7 output f-ratio. The throughput losses when the complete fibre bundle is measured, as shown in figure 5.10 (a) are bigger on average than those obtained when only the conduit part is measured, figure 5.8 (a). Clearly, this is caused by the new elements introduced into the system. These elements are the two extra end faces, the prism, an extra 1m fibre and the alignment of the connection. The same is true for the results obtained at an f/11.2 output f-ratio.

The effects can be better appreciated from figure 5.11 where the ratio between the throughput results for the fibre conduit section and those obtained with the complete fibre bundle, are given. Figure 5.11 (a) shows the ratio of throughput at f/4.7. Assuming that the quality of the fibre ends is comparable, it would be expected to obtain better results for the fibres within the conduit than for the complete fibre bundle. Therefore the ratio values should be greater than unity. However for 13 fibres this is not the case.

One possible explanation is that the quality of the fibre end in the connector face of the conduit is worse than the fibre end that has the prism. If the connection between the two halves of the connector is good *i.e.* without significant misalignment, the inclusion of the index matching gel will compensate for the fibre end defects, thereby improving the fibre transmission. Furthermore, the input end of the fibre at the connector face, is replaced by the fibre end with the prism and if this end is better less light will be scattered.

The corresponding curve at an f/11 output f-ratio is shown in figure 5.11 (b) where it is true that the ratio of throughput is greater or equal to unity for all the fibres. This is probably because the addition of the fibre module introduces extra FRD which makes the overall losses worse even for those which improved at f/4.7. However it is worth noting

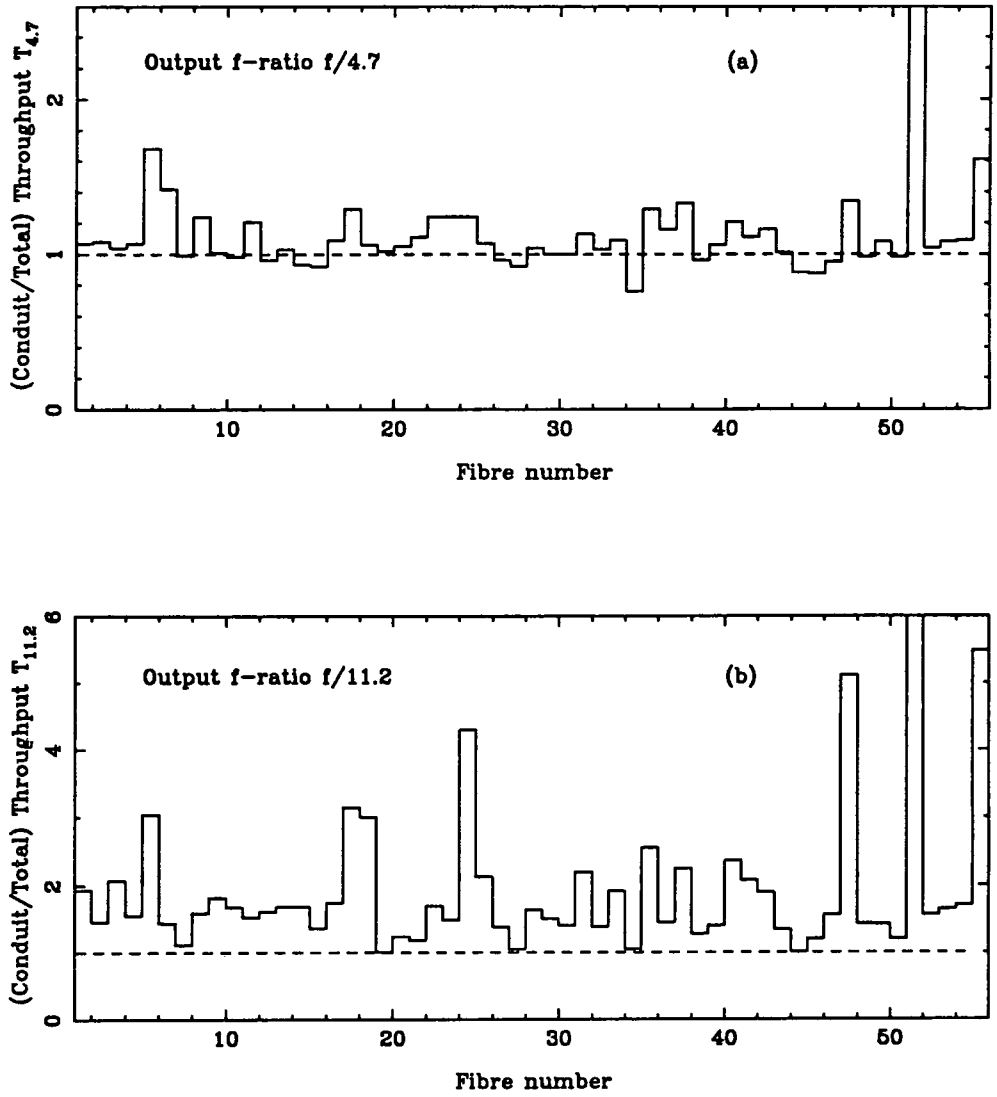

Figure 5.11. Ratio between the absolute throughput of the fibres within the conduit and that of the complete fibre bundle. a) At an f/4.7 output f-ratio. b) At an f/11.2 output f-ratio.

that for 5 of the 13 fibres mentioned in the last paragraph the throughput ratio is, in this case, equal or very close to unity.

Unfortunately, it is practically impossible to measure accurately and independently the effect of the many factors involved in a good connection *i.e.* lateral and angular misalignment, index matching uniformity and surface optical quality. However a relation between them can be established knowing the misalignment between the fibre ends at the connector interface and the quality of the four end faces of each fibre (see §5.5.2).

5.4.4 Prediction of the throughput at f/8

Autofib-1.5 has been used at the f/11 Cassegrain focus of the WHT in combination with the FLEX spectrograph which accepts an f/8 input beam. Therefore to estimate the losses at the telescope it is required to know the throughput at an f/8 output f-ratio.

From the throughput measurements presented in the previous section it is possible to interpolate the values obtained at f/4.7 and f/11.2 to predict the throughput value at an intermediate output f-ratio such as f/8. Thus, a linear interpolation was applied to the results obtained at an output f-ratio of f/4.7 and f/11.2 for the whole fibre set. Figure 5.12 (a) shows the predicted values for the fibres in the conduit, where the mean value is 47% $\pm$ 4.7%. Figure 5.12 (b) shows the corresponding results for the complete fibre system where the throughput mean value is 39% $\pm$ 8.5%. In summary, for an f/11 input beam about 40% of the light emerges still within an f/8 cone. This is the average predicted efficiency for Autofib-1.5 as used on the WHT.

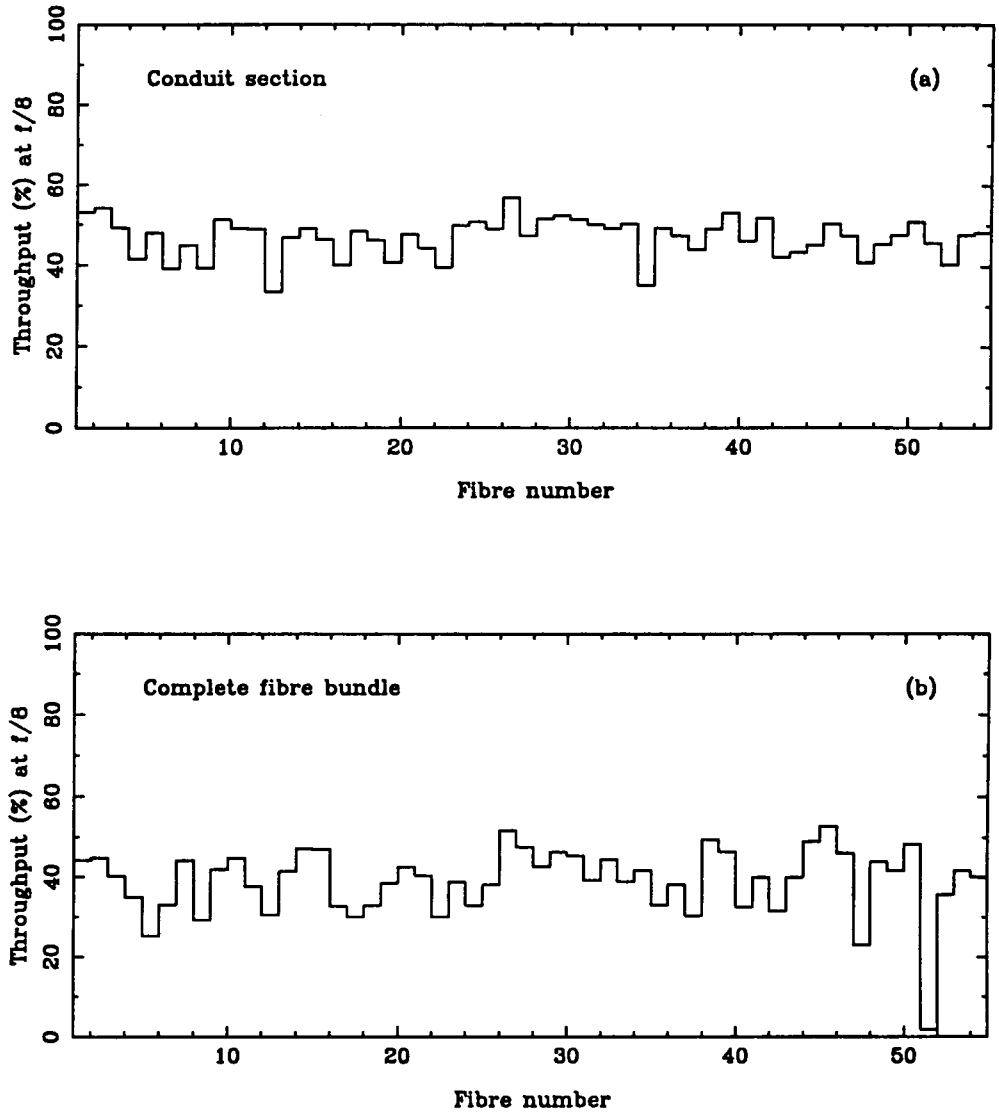

Figure 5.12. Absolute throughput values predicted at an f/8 output f-ratio. The values were estimated by applying a linear interpolation to the throughput values at f/4.7 and at f/11.2 shown in figures 5.8 and 5.10. a) Results for the fibres in the conduit. The mean throughput is 47%. b) Results for the complete fibre system as used on the WHT. The mean throughput is 39%.

5.5 Visual inspection of the end faces

The optical quality of the fibre ends is a fundamental parameter in terms of throughput and FRD performance. The better the quality of the fibre ends, the better the throughput, although a high quality end preparation does not always guarantee low FRD.

A quantitative determination of the optical quality of the fibre ends, applying interferometric techniques, would have been desirable. A common method consists of specifying the surface accuracy in terms of the number and regularity of Newton's rings which will be seen when the surface under test is combined with an optical flat reference. The equipment required for this kind of evaluation was not available in our Optics Laboratory, therefore a visual inspection was chosen as an alternative method.

The visual inspection of the four end faces of each fibre was carried out with the intention of finding a relationship between the quality of the fibre ends and the throughput results discussed in the last section. The experimental setup consisted of a microscope objective, with a holder that allowed focussing adjustments, attached to a CCD camera. Some images were recorded via a PC-based frame grabber.

The inspection was done in four stages. First, the fibre ends with prisms were analysed and the inspection camera was fixed to the centre of Autofib's field plate, using a magnetic clamp. For visual inspection each fibre was moved manually to the centre of the field plate and aligned with the experimental device. Second, to examine the fibre end faces in the connector underneath the field plate, the Autofib fibre module was inverted. The inspection camera was moved about the array of fibres in the connector via an x-y micrometer stage. Third, the fibre end faces in the other half of the connector were inspected. In this case the inspection camera was fixed to the optical table and the

connector surface was mounted on an x-y micrometer stage. Finally, the slit end of each fibre was analysed with a similar arrangement.

Four categories (A-D) of end preparation were defined and a number was associated with each one in order to manipulate the results. **A:** a smooth surface without scratches (1.0), **B:** a smooth surface with one or two narrow scratches (0.75), **C:** three or four scratches with a small smooth area (0.50) and **D:** a surface full of scratches (0.25). A typical example of each quality is shown in figures 5.13 to 5.16. The actual fibre diameter is 260μm while in the figures the magnification factor is 490. It can be appreciated that there is a wide range of surface qualities. The differences are mainly due to a poor polishing process.

5.5.1 The visual inspection results

As mentioned before the main factors that contribute to losses when joining fibres together are: Fresnel losses, caused by back reflection at the glass/air interfaces and end alignment losses. Fresnel losses are practically eliminated by filling the gap between the fibres with a gel that matches the refractive index of the fibre core. Extreme care should be taken to avoid dirt being picked up in the index matching gel because this may nullify the potential advantage of having it.

The throughput results obtained for the fibres in the conduit section and those obtained for the complete system can be related with the results of the visual inspection by considering the following experimental conditions. When the throughput of each fibre in the conduit section was measured the input was the fibre end at the connector face while the output was the slit end. When the throughput of the complete system was measured (*i.e.* the conduit section was attached to Autofib-1.5 fibre module) the input

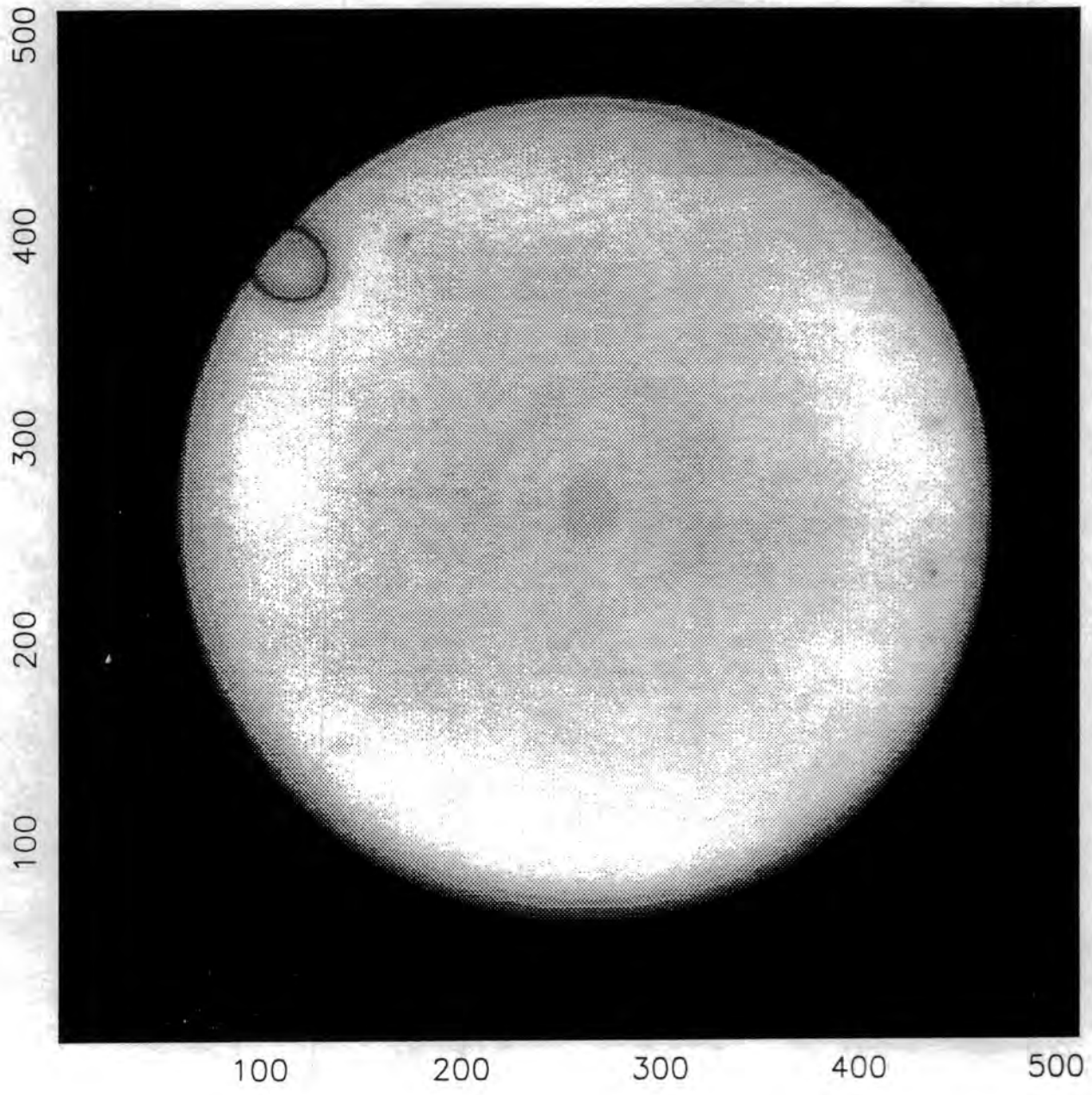

Figure 5.13. An example of the fibre quality classification A.

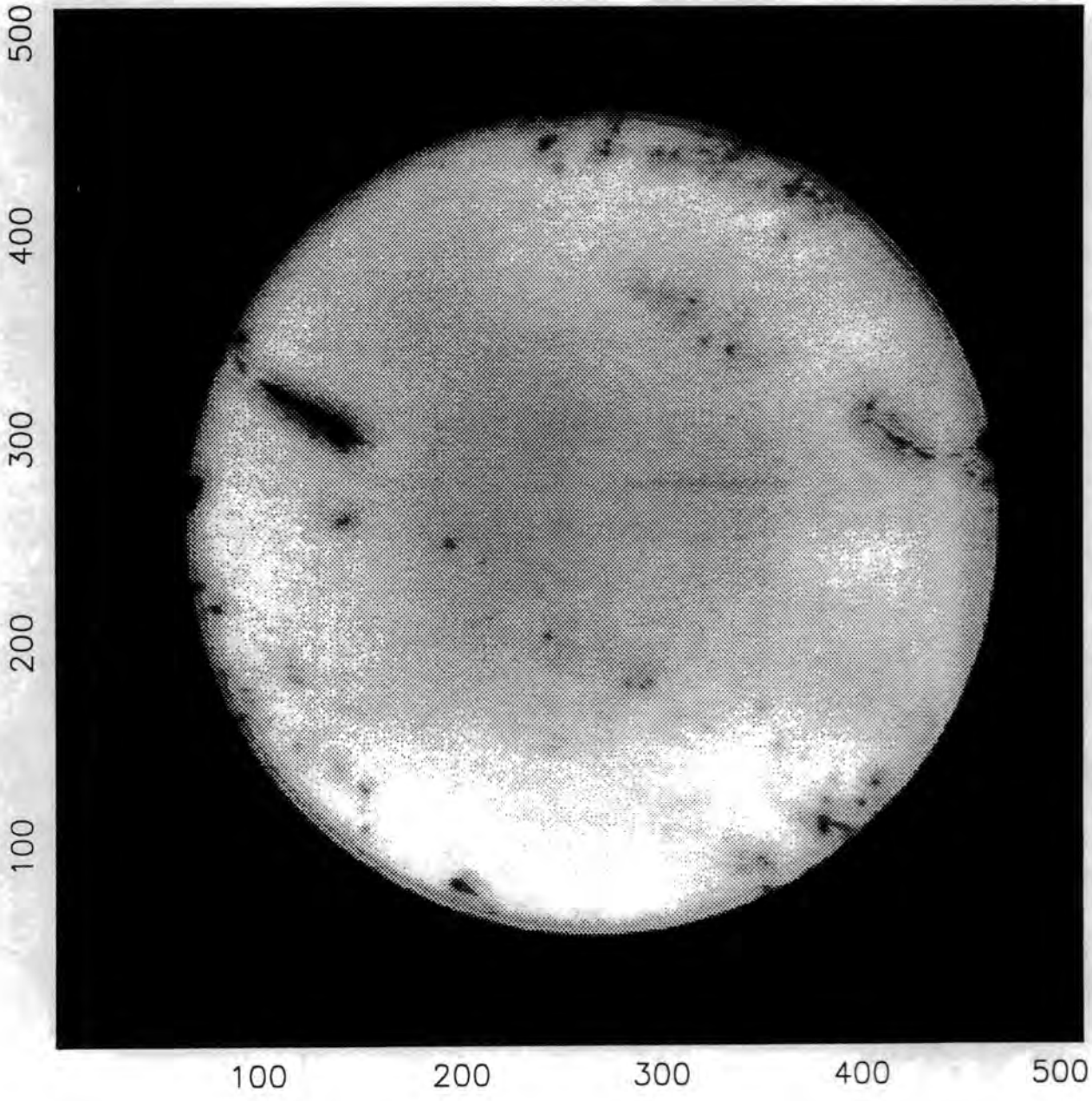

Figure 5.14. An example of the fibre quality classification B.

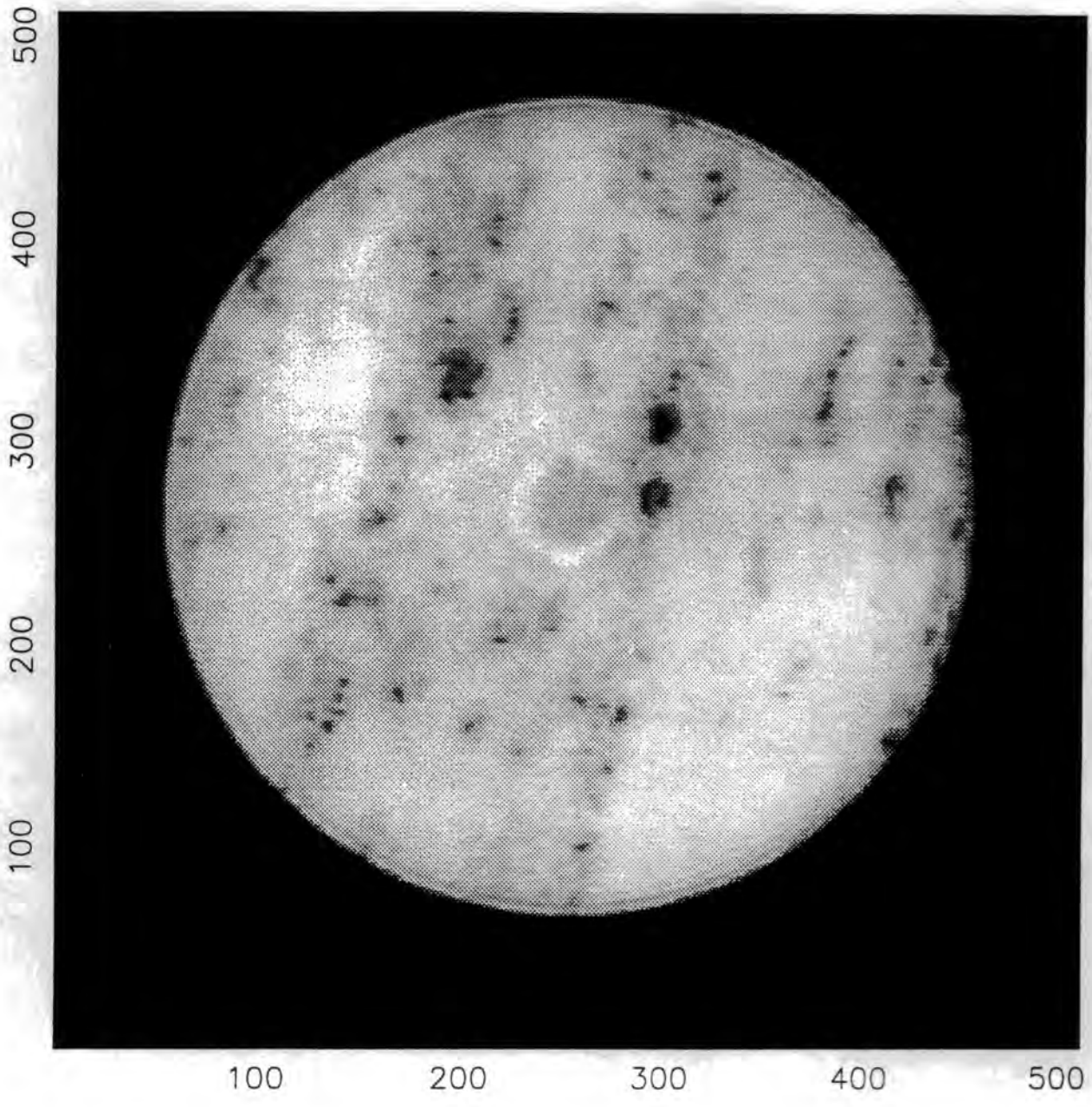

Figure 5.15. An example of the fibre quality classification C.

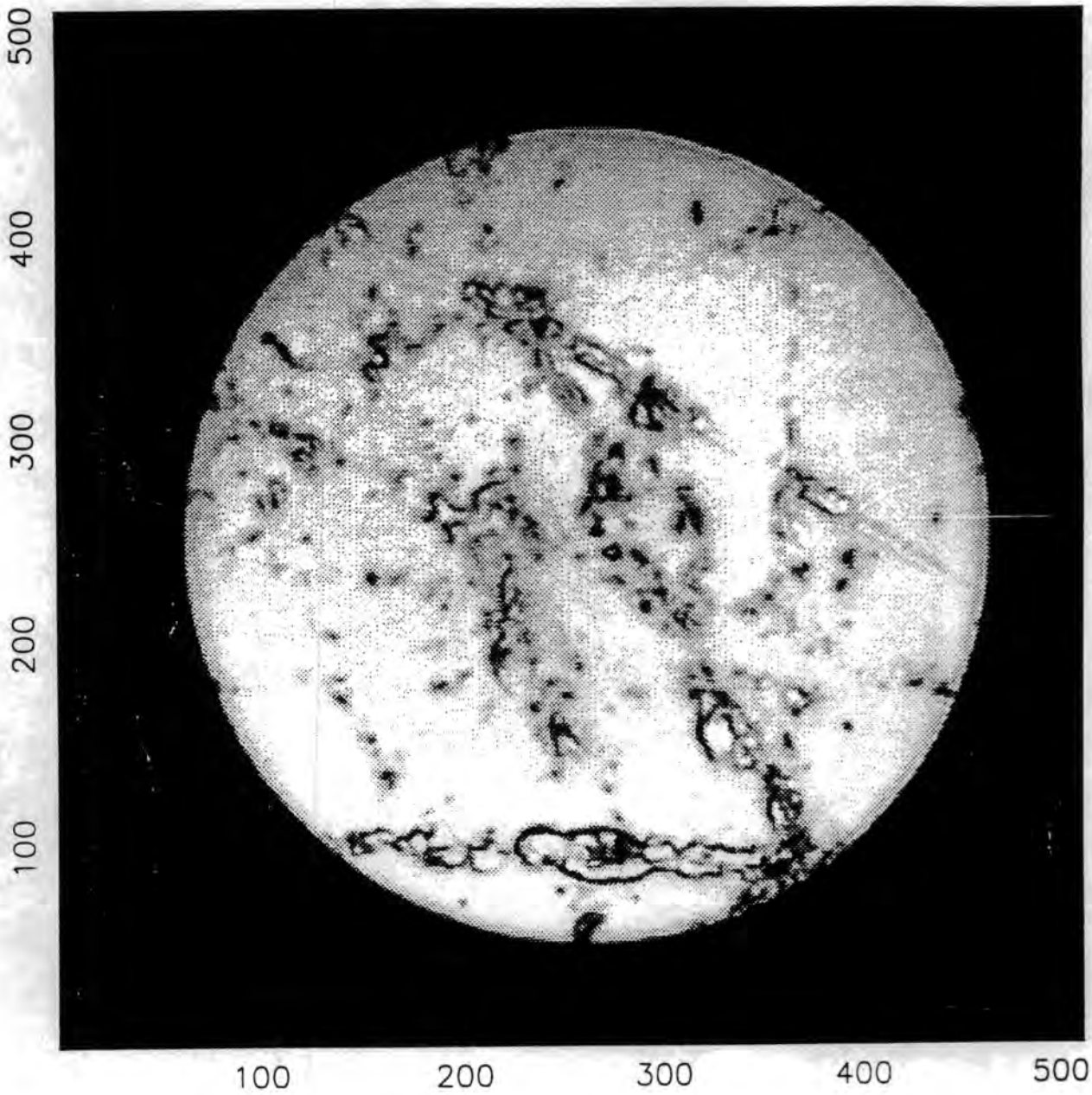

Figure 5.16. An example of the fibre quality classification D.

was the prism end, the two faces of the connector were joined using an index matching gel and the output end was the slit end.

If we assume that the index matching gel helps to fill-in the imperfections of the fibre surfaces in the connector, then the quality of these two ends is not particularly significant when considering the complete system. Also the output end is the same for both the conduit section on its own and for the complete system. Therefore, for comparison purposes the ends of most interest are the prism end and the connector end in the conduit section.

Table 5.1 summarises the results of the visual inspection for the four end faces of each fibre. The first column has the fibre number, the second the quality of the prism end (P_{end}), the third the quality of the fibre end at the connector face in Autofib-1.5 (CA_{end}). The fourth has the quality of the end in the connector face of the conduit section (CC_{end}) and the fifth the quality of the slit end (S_{end}). The ratio $T_{4.7}$ of the throughput of the conduit section and the throughput of the complete system at an output ratio of 4.7 is given in the sixth column. In the seventh column is a similar ratio $T_{11.2}$ obtained at f/11. Finally, in the eight column the shift (δr) between the fibres ends at the connector interface, as described in section 5.3, is presented.

In general the fibre ends which have prisms attached to them, have better quality than the other three ends. It is possible that the epoxy used to attach the prisms to the fibres helps, to some extent, to fill irregularities in the surfaces.

Table 5.1 (a) lists those fibres for which the throughput of the complete system is better than the throughput of the conduit section *i.e.* $T_{4.7}$ is less than unity. For most of them the prism end quality is better than the end quality in the connector face of the conduit section. Having a better prism end implies that less light is scattered at the input end and therefore more light is going into the fibre. The results suggest that for

Table 5.1 (a). Visual inspection Results. Surface quality

#	P_{end}	CA_{end}	CB_{end}	S_{end}	$T_{4.7}$	$T_{11.2}$	$\delta r(\mu m)$
10	0.75	0.50	0.50	0.75	0.98	1.64	52
12	1.00	0.50	0.25	0.25	0.97	1.57	42
14	1.00	0.50	0.25	0.75	0.89	1.68	31
15	1.00	0.75	0.50	0.50	0.90	1.34	37
26	1.00	0.75	0.50	1.00	0.98	1.46	7
27	1.00	0.25	0.25	0.75	0.96	1.10	40
30	0.50	0.50	0.50	0.50	0.99	1.55	21
34	0.25	0.50	0.25	0.25	0.79	1.02	46
38	0.75	0.75	0.75	0.50	0.90	1.33	33
44	1.00	0.50	0.25	1.00	0.89	1.03	53
45	1.00	0.50	0.50	1.00	0.86	1.23	62
46	1.00	0.75	0.25	0.75	0.91	1.52	41
48	1.00	0.50	0.50	1.00	0.95	1.39	77

Table 5.1 (b). Visual Inspection Results. Surface quality

#	P_{end}	CA_{end}	CB_{end}	S_{end}	$T_{4.7}$	$T_{11.2}$	$\delta r(\mu m)$
1	0.25	0.50	0.50	0.75	1.02	1.88	54
5	0.25	0.25	0.50	0.75	1.69	2.89	66
8	0.25	0.50	0.50	0.25	1.31	1.51	85
11	0.25	0.50	0.50	1.00	1.23	1.52	3
17	0.25	0.50	0.50	0.75	1.33	3.19	31
22	0.25	0.25	0.75	0.25	1.21	1.75	83
23	0.25	0.50	0.50	1.00	1.22	1.52	82

Table 5.1 (c). Visual Inspection Results. Surface quality

#	P_{end}	CA_{end}	CB_{end}	S_{end}	$T_{4.7}$	$T_{11.2}$	$\delta r(\mu m)$
2	1.00	0.25	0.75	0.75	1.13	1.43	60
3	0.50	0.25	0.25	1.00	1.04	2.07	57
4	1.00	0.50	0.25	0.50	1.09	1.55	91
6	1.00	0.50	0.25	0.25	1.13	1.35	30
7	1.00	0.25	0.50	0.75	1.00	1.08	51
9	1.00	0.50	0.25	1.00	1.04	1.81	19
13	0.75	0.25	0.50	0.50	1.01	1.66	72
16	1.00	0.50	0.50	0.25	1.05	1.79	32
18	0.75	0.50	0.75	0.50	1.14	3.04	34
19	0.25	0.75	0.25	0.25	1.06	1.06	19
20	0.50	0.25	0.50	1.00	1.07	1.28	80
21	1.00	0.25	0.50	0.75	1.07	1.22	144
24	0.50	0.50	0.50	1.00	1.24	4.39	84
25	0.75	0.50	0.50	0.75	1.11	2.22	95
28	1.00	0.50	0.25	0.75	1.06	1.73	54
29	0.50	0.75	0.50	0.50	1.00	1.56	27
31	1.00	0.50	0.50	0.75	1.10	2.27	54
32	0.75	0.50	0.50	1.00	1.03	1.33	26
33	0.75	0.50	0.50	1.00	1.13	1.87	21
35	0.25	0.50	0.25	1.00	1.29	2.49	96
36	0.25	0.50	0.25	1.00	1.19	1.43	186
37	0.25	0.50	0.25	0.75	1.33	2.18	109
39	0.75	0.25	0.50	1.00	1.05	1.41	35
40	0.25	0.50	0.25	0.75	1.23	2.41	44
41	0.75	0.50	0.25	1.00	1.13	2.03	47
42	0.50	0.50	0.50	0.50	1.23	1.84	70
43	0.50	0.25	0.25	0.50	1.01	1.33	47
47	0.50	0.50	0.50	0.25	1.32	5.41	47
50	0.50	0.25	0.50	0.75	1.01	1.17	40
51	0.50	0.50	0.50	0.25	19.56	34.00	45
52	0.50	0.50	0.25	0.25	1.05	1.49	74
53	0.50	0.50	0.25	0.75	1.04	1.58	73
54	0.50	0.25	0.50	0.50	1.09	1.66	61
55	1.00	0.25	0.50	0.75	1.62	5.34	59

these fibres the connector coupling is efficient and the increase in throughput is due to the replacement of a poor input end with a better one, in good agreement with the values of δr. For those fibres for which the quality of the two alternative input ends is comparable we expect $T_{4.7}$ to be close to unity. However for fibres 34 and 38 the throughput of the complete system is definitely better than that for the conduit section. It should be noticed that there is also an error associated to the assigning fibre end quality and it is possible that the prism end has a better quality than that of the connector input end.

Table 5.1 (b) presents the results of the fibres for which the prism end quality is worse than that in the connector face of the conduit section. Following the previous reasoning, if the prism end has a poorer quality more light will be lost at its surface and therefore $T_{4.7}$ should to be greater than unity. Indeed we find $T_{4.7}$ to be significantly greater than unity for all the fibres in table 5.1 (b). Clearly, the losses are dominated by the quality of the fibre ends.

The results for the fibres for which the prism end quality is no worse than that in the connector face of the conduit section but for which $T_{4.7}$ is greater than unity are shown in table 5.1 (c). For these fibres $T_{4.7}$ must be greater than unity because of misalignment at the connector. For fibres No. 3, 7, 9, 13, 29, 32, 43 and 53, $T_{4.7}$ is very close to unity and given the errors in the throughput measurements ($\sim 4\%$) the alignment may still be quite good. The results are consistent with the values of δr for these fibres, in particular for fibres No. 9, 29, 32 and 43. However for the rest of fibres included in this table, $T_{4.7}$ is significantly greater than one and the losses for the complete system are probably dominated by misalignments at the connector.

At f/11.2 it is clear that the dominating loss mechanism is FRD, as can be appreciated from the fact that $T_{11.2}$ is greater than unity for all the fibres. Given the experimental errors $T_{11.2}$ is very close to unity only for fibres 27, 34 and 44 (Table 5.1 (a)). In agreement

with the results obtained for $T_{4.7}$, the alignment at the connector is good and the replacement of a poor input end with a better one improves the throughput for the complete system. However for the rest of the fibres there is not a clear pattern associated to the values of $T_{11.2}$ and the quality of the fibre ends. For those fibres for which the losses for the complete fibre bundle are dominated by misalignment at the connector at f/4.7, the losses at f/11.2 are more pronounced.

5.5.2 End quality *vs.* throughput

In an attempt to relate the optical quality of the surfaces of each fibre with its corresponding throughput results, the optical performance V was defined as the product of the quality of the ends. For the conduit section the performance will be the product of the slit end quality and the end quality at the connector face *i.e.* $V = (S_{end})(CC_{end})$. While for the complete system the performance will be the product of the quality of the slit end and the prism end *i.e.* $V = (P_{end})(S_{end})$, since the connector qualities are masked by the gel.

Figure 5.17 (a) shows the optical performance as a function of the throughput results obtained at f/4.7 for the 55 fibres in the conduit section. Although it is a qualitative evaluation it is apparent that there is a definite trend to obtain a better throughput as the quality of the fibre end surfaces improves. An equivalent graph for the performance of the complete fibre bundle at f/4.7 is shown in figure 5.17 (b) where a less pronounced trend is also observed. This is probably because there are more factors contributing to the losses for the complete fibre bundle than for the conduit section on its own. These extra factors include the prism, two extra ferrules (FRD) and the connector misalignments.

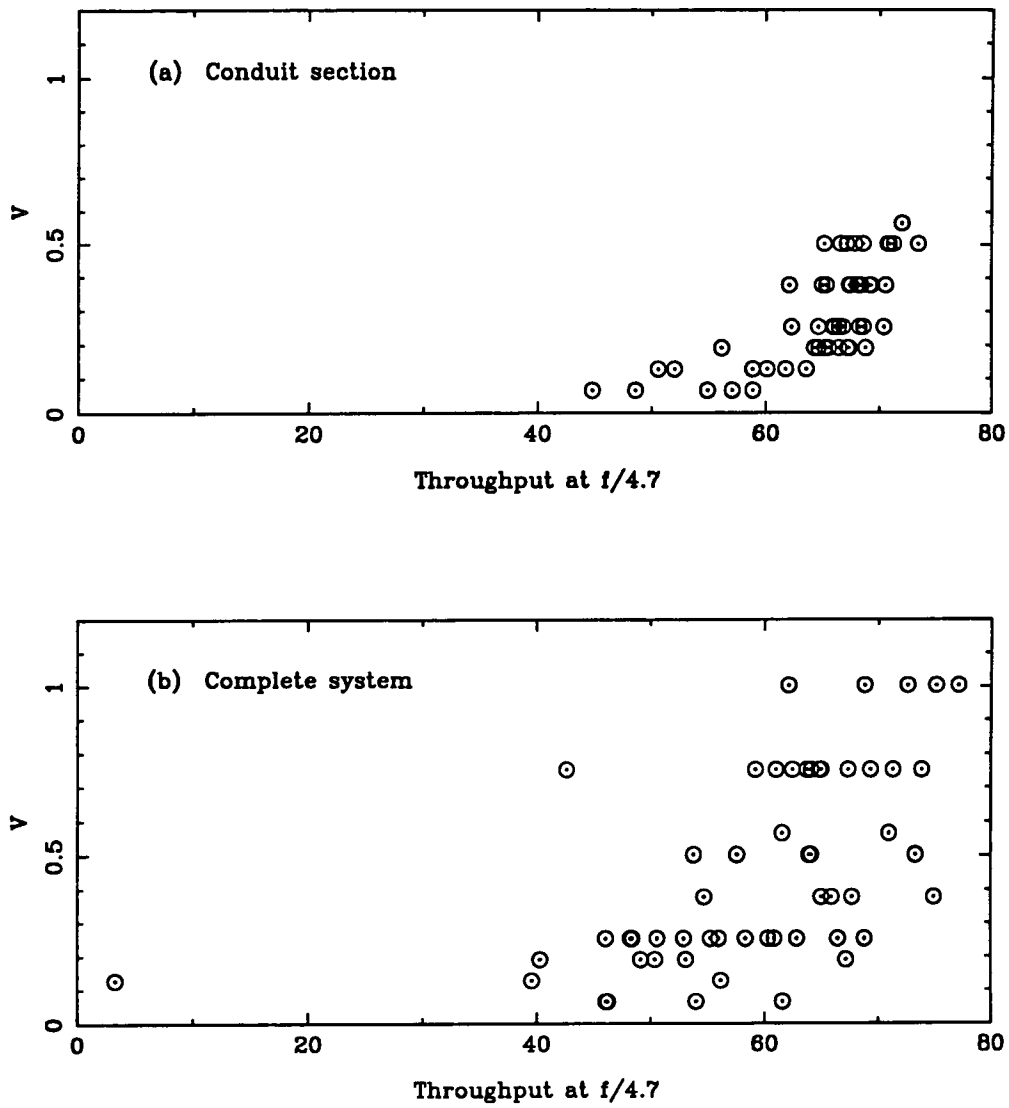

Figure 5.17. Throughput values *vs.* performance results. For each fibre channel the performance V, is defined as the product of the surfaces quality of its ends. a) For the fibre the conduit section of the fibre bundle, $V = (S_{end})(CC_{end})$. b) For the complete system, $V = (P_{end})(S_{end})$.

5.6 FRD measurements

5.6.1 FRD measurements with the photodiode experiment

The results presented in the previous sections are indicative of the average FRD of the fibres. However it is useful to have more than two points to complete any FRD curve and so the throughput at 4 different output f-ratios was measured for a few fibres. The FRD measurements were carried out with the same photodiode experiment presented in section 5.4. The measurements for the fibres in the conduit section were obtained as described in section 5.4.1 while the FRD measurements for the complete fibre bundle were obtained following the process described in section 5.4.2. The output f-ratios chosen for these experiments were: f/5, f/6.2, f/8 and f/11.2.

The final results are shown in figure 5.18. The crosses correspond to the values obtained for the complete fibres while the open circles correspond to those obtained for the fibres in the conduit section. The fibres used for measurements are indicated.

The results for the four fibres are consistent with the throughput measurements reported in sections 5.4.2 and 5.4.3. Consider, for instance fibre 26, which is the best of all the fibres in the bundle. The complete fibre has a very similar throughput to the fibre within the conduit at all the different output f-ratios measured. In the other three cases the throughput is better for the conduit section than for the complete bundle. The throughput results at an f/8 output f-ratio are slightly lower than those predicted in section 5.4.4 showing that the linear interpolation applied to derive the vignetting function at an f/8 output f-ratio, probably overestimates the throughput by a few percent.

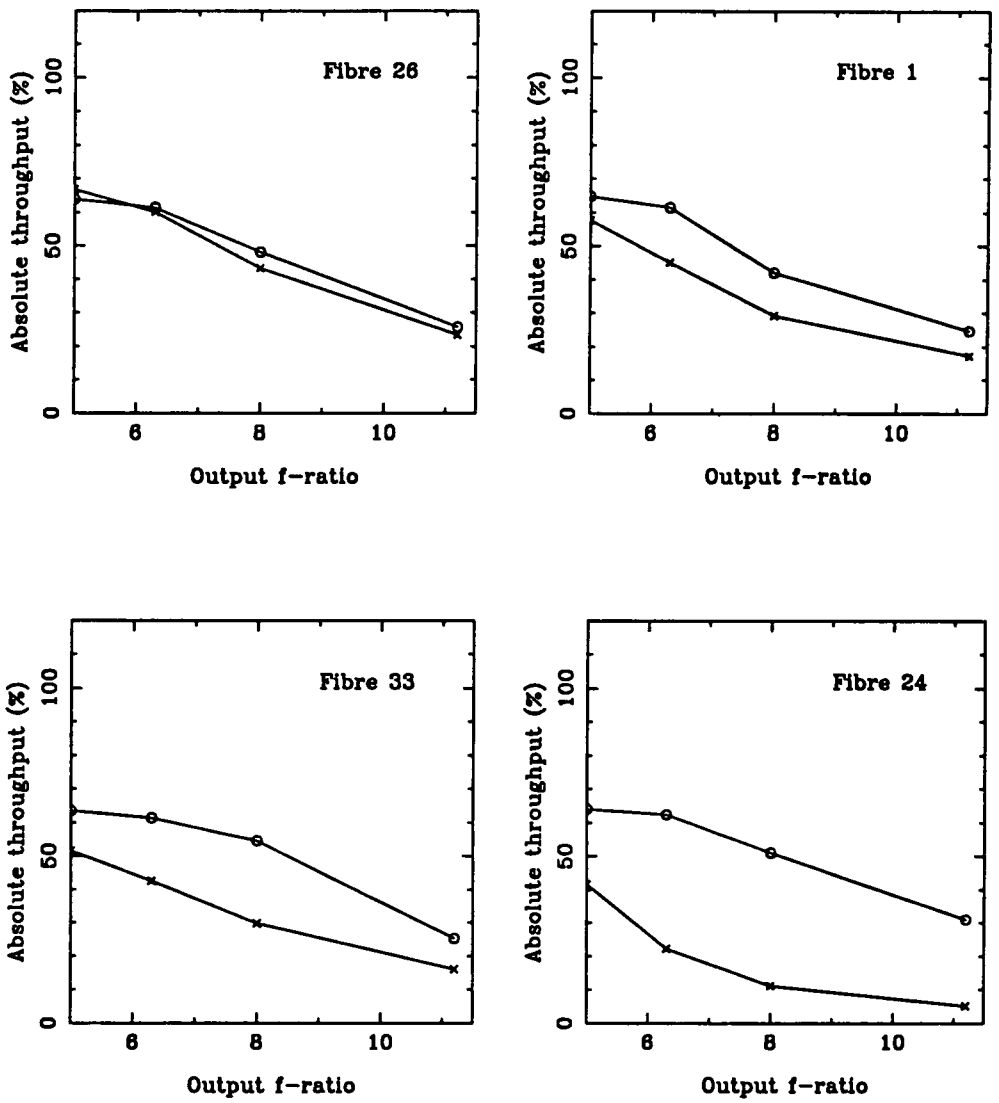

Figure 5.18. Focal ratio degradation curves. The open circles correspond to the results obtained for the conduit section. The crosses are the results obtained for the complete fibre. The fibre numbers are indicated. Both measurements were made with the photodiode experiment described in section 5.4.

5.6.2 FRD measurements via the CCD experiment

An alternative method to that previously described to measure the degree of FRD is to take an image of the far-field output of the fibre and to measure the amount of light within circles of different radii. Knowing the distance between the fibre output end and the detector, the output focal ratio corresponding to a given radius is inferred. The main advantage of this method is that all the information is obtained in a single exposure, so errors due to variations in the light source or in the detector stability are eliminated. However this method requires an image reduction process and it is not possible to obtain results in real-time.

For comparison purposes a sample of fibres of the conduit section were chosen to measure their FRD using this alternative method. The setup was the CCD experiment described in detail in chapter 4 (§4.4.). In this experiment a cryogenically cooled CCD is used as the main detector. The resultant images from the CCD were stored on the PC and afterwards they were transferred to the local starlink VAX cluster. The reduction software integrates the light falling within annuli of varying radii to obtain a measurement of the output throughput. It finds the image centre by calculating the weighted average of all the pixel positions. It associates a radius to each pixel. The radii are converted to output focal ratio by taking their reciprocal and multiplying them by the appropriate constant. This constant is the distance between the fibre output end and the detector corrected by taking into account the diameter of the fibre.

To compare the two methods a suitable normalization value was the throughput obtained at an f/5 output f-ratio. The FRD results reported for the fibres in the conduit section were normalised with their respective throughput values obtained at an f/5 output f-ratio. Figure 5.19 shows the results obtained for the indicated fibres in the conduit. The dotted lines correspond to the CCD measurements and the solid lines are the results

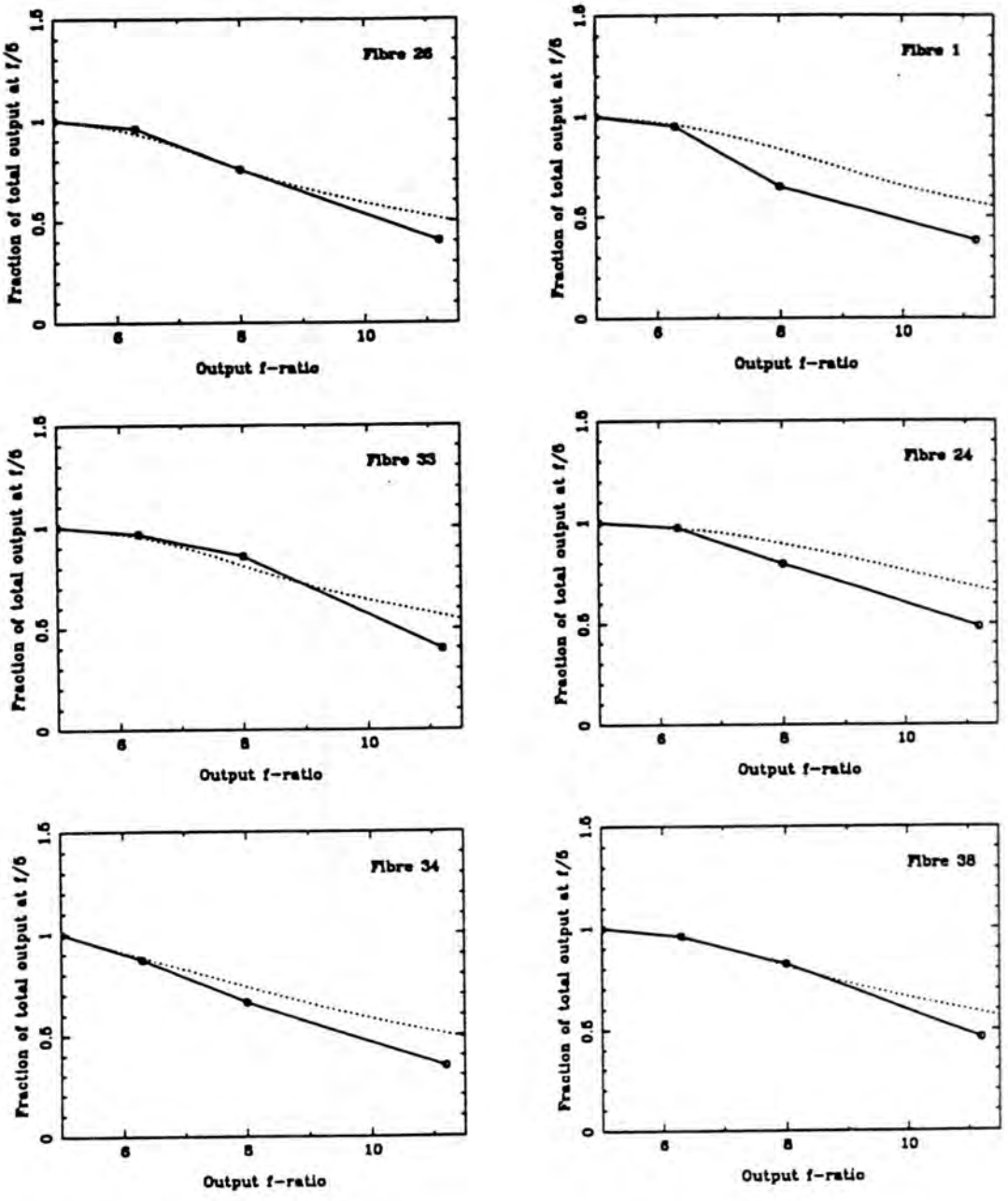

Figure 5.19. Focal ratio degradation curves for different fibres in the conduit as indicated. The dotted lines correspond to the results from the CCD experiment and the solid lines are the results obtained via the photodiode experiment.

obtained with the photodiode experiment. The FRD curves obtained with the CCD are slightly higher than those obtained with the photodiode, in particular at slow output f-ratios where the average difference is 10%. As discussed in chapter 4 (§4.4), in the CCD experiment the positioning of the fibre output end at the required distance from the detector was very critical. An error in the positioning can lead to an underestimation of the FRD as in the cases shown in the figure. Another possible explanation is a difference in the normalization point.

5.7 Summary and Conclusions

The laboratory evaluation of the Autofib-1.5 fibre bundle has included several aspects:

- For an f/11 input beam, such as for the Cassegrain focus of the WHT, the efficiency in terms of throughput and FRD for the fibre bundle and for the conduit section was measured for the complete set of 55 fibres.

- The alignment between the two halves of the connector was estimated from measurements of the position of each fibre in both faces of the connector. A simple model was developed to estimate the losses due to misalignment at the connector interface.

- A visual inspection of the quality of the four end faces of each fibre was carried out with the purpose of finding a relationship between the quality of the fibre ends and the throughput results.

- The throughput at different output f-ratios was measured to obtain FRD curves for a subset of fibres, both for the complete fibre bundle and the conduit section.

• The FRD was also measured for a few fibres of the conduit section with an alternative method, the CCD experiment.

A summary of all the results is given in table 5.2. The first column has the fibre number. The following four columns present the results of the visual inspection: the quality of the prism end (P_{end}), quality of the fibre end at the connector face in Autofib-1.5 (CA_{end}), the quality of the end in the connector face of the conduit section (CC_{end}) and the quality of the slit end (S_{end}). In the sixth column the absolute throughput measured for the complete fibre bundle at an f/4.7 output f-ratio $(E_{ff})_{4.7}$ (%) is given. The predicted absolute throughput at an f/8 output f-ratio $(E_{ff})_8$ is presented in the seventh column. The absolute throughput measured at an f/11 output f-ratio $(E_{ff})_{11.2}$ is given in the eighth column. The ratio $T_{4.7}$ of the throughput of the conduit section and the throughput of the complete system at an output ratio of 4.7 is given in the ninth column. In the tenth column is a similar ratio $T_{11.2}$ obtained at f/11. Finally, in the eleventh column the shift δr between the fibres ends at the connector interface is presented.

The mean throughput of the complete fibre bundle measured at an f/4.7 output f-ratio is 65%. If the losses were exclusively due to Fresnel reflection and absorption it would be expected to obtain an average throughput of about 87%. The average misalignment between the two halves of the connector is 50μm. The transmission losses predicted by the model for this misalignment is 17.4% (20% of 87%). Therefore the expected throughput would be about 70%. The difference between the two values can be explained by the poor quality of the fibre ends. The effect of FRD is very severe as can be seen from the fibre bundle results at an f/11.2 output f-ratio for which the mean throughput value is only 17%.

It should be noticed that the values given above are only average values but in the case of multifibre systems, each fibre represents a particular case and the throughput values can vary significantly between fibres. The quality of the fibre ends vary widely amongst the fibre bundle, due to a poor polishing process. The results show clearly that the polishing techniques which were used for these fibres have to be improved. Also, the mechanisms that increase the effect of FRD such as stress induced by the fibre end ferrules have to be eliminated.

From the throughput results obtained at an output f-ratio of f/4.7 and f/11.2 it is predicted that the efficiency of Autofib-1.5 fibre bundle on the WHT working in combination with the FLEX spectrograph is on average 40%.

Table 5.2 Results of the Autofib-1.5 fibre bundle evaluation

#	P_{end}	CA_{end}	CB_{end}	S_{end}	$(E_{ff})_{4.7}$	$(E_{ff})_{8}$	$(E_{ff})_{11.2}$	$T_{4.7}$	$T_{11.2}$	$\delta r(\mu m)$
1	0.25	0.50	0.50	0.75	67.14	44.07	19.87	1.02	1.88	54
2	1.00	0.25	0.75	0.75	63.71	44.72	24.94	1.13	1.43	60
3	0.50	0.25	0.25	1.00	63.89	40.17	15.21	1.04	2.07	57
4	1.00	0.50	0.25	0.50	53.79	34.96	15.21	1.09	1.55	91
5	0.25	0.25	0.50	0.75	40.25	25.18	9.33	1.69	2.89	66
6	1.00	0.50	0.25	0.25	48.37	33.05	17.03	1.13	1.35	30
7	1.00	0.25	0.50	0.75	67.32	44.16	19.87	1.00	1.08	51
8	0.25	0.50	0.50	0.25	46.02	29.22	11.56	1.31	1.51	85
9	1.00	0.50	0.25	1.00	62.09	41.85	20.68	1.04	1.81	19
10	0.75	0.50	0.50	0.75	70.93	44.67	17.03	0.98	1.64	52
11	0.25	0.50	0.50	1.00	55.23	37.64	19.26	1.23	1.52	3
12	1.00	0.50	0.25	0.25	46.02	30.39	13.99	0.97	1.57	42
13	0.75	0.25	0.50	0.50	65.88	41.39	15.61	1.01	1.66	72
14	1.00	0.50	0.25	0.75	73.82	47.12	19.06	0.89	1.68	31
15	1.00	0.75	0.50	0.50	73.28	46.94	19.26	0.90	1.34	37
16	1.00	0.50	0.50	0.25	48.19	32.66	16.42	1.05	1.79	32
17	0.25	0.50	0.50	0.75	49.09	29.93	9.73	1.33	3.19	31
18	0.75	0.50	0.75	0.50	54.69	32.82	9.73	1.14	3.04	34
19	0.25	0.75	0.25	0.25	53.97	38.44	22.30	1.06	1.06	19
20	0.50	0.25	0.50	1.00	64.07	42.59	20.07	1.07	1.28	80

Table 5.2 (*cont.*) Results of the Autofib-1.5 fibre bundle evaluation

#	P_{end}	CA_{end}	CB_{end}	S_{end}	$(E_{ff})_{4.7}$	$(E_{ff})_{8}$	$(E_{ff})_{11.2}$	$T_{4.7}$	$T_{11.2}$	$\delta r(\mu m)$
21	1.00	0.25	0.50	0.75	61.00	40.33	18.65	1.07	1.22	144
22	0.25	0.25	0.75	0.25	46.20	29.90	12.77	1.21	1.75	83
23	0.25	0.50	0.50	1.00	58.30	38.74	18.25	1.22	1.52	82
24	0.50	0.50	0.50	1.00	57.58	32.85	6.69	1.24	4.39	84
25	0.75	0.50	0.50	0.75	61.55	37.99	13.18	1.11	2.22	95
26	1.00	0.75	0.50	1.00	75.08	51.64	27.17	0.98	1.46	7
27	1.00	0.25	0.25	0.75	69.31	47.60	24.94	0.96	1.10	40
28	1.00	0.50	0.25	0.75	64.80	42.67	19.46	1.06	1.73	54
29	0.50	0.75	0.50	0.50	68.77	46.36	22.91	1.00	1.56	27
30	0.50	0.50	0.50	0.50	66.42	45.44	23.52	0.99	1.55	21
31	1.00	0.50	0.50	0.75	64.07	39.10	12.77	1.10	2.27	54
32	0.75	0.50	0.50	1.00	64.98	44.41	22.91	1.03	1.33	26
33	0.75	0.50	0.50	1.00	59.20	38.91	17.64	1.13	1.87	21
34	0.25	0.50	0.25	0.25	61.55	41.77	21.08	0.79	1.02	46
35	0.25	0.50	0.25	1.00	52.88	32.95	11.96	1.29	2.49	96
36	0.25	0.50	0.25	1.00	55.95	38.11	19.46	1.19	1.43	186
37	0.25	0.50	0.25	0.75	50.36	30.29	9.12	1.33	2.18	109
38	0.75	0.75	0.75	0.50	74.90	49.42	22.71	0.90	1.33	33
39	0.75	0.25	0.50	1.00	67.32	46.49	24.73	1.05	1.41	35
40	0.25	0.50	0.25	0.75	53.06	32.56	10.95	1.23	2.41	44

Table 5.2 (*cont.*) Results of the Autofib-1.5 fibre bundle evaluation

#	P_{end}	CA_{end}	CB_{end}	S_{end}	$(E_{ff})_{4.7}$	$(E_{ff})_{8}$	$(E_{ff})_{11.2}$	$T_{4.7}$	$T_{11.2}$	$\delta r(\mu m)$
41	0.75	0.50	0.25	1.00	62.45	39.91	16.22	1.13	2.03	47
42	0.50	0.50	0.50	0.50	50.54	31.55	11.56	1.23	1.84	70
43	0.50	0.25	0.25	0.50	60.82	40.04	18.25	1.01	1.33	47
44	1.00	0.50	0.25	1.00	72.56	48.99	24.33	0.89	1.03	53
45	1.00	0.50	0.50	1.00	77.07	52.86	27.57	0.86	1.23	62
46	1.00	0.75	0.25	0.75	71.29	46.11	19.67	0.91	1.52	41
47	0.50	0.50	0.50	0.25	39.53	22.97	5.47	1.32	5.41	47
48	1.00	0.50	0.50	1.00	68.77	43.94	17.84	0.95	1.39	77
49	1.00	0.50	0.75	0.25	60.28	41.70	22.30	1.07	1.36	52
50	0.50	0.25	0.50	0.75	67.68	48.32	28.18	1.01	1.17	40
51	0.50	0.50	0.50	0.25	3.25	1.77	0.20	19.5	134	45
52	0.50	0.50	0.25	0.25	56.13	35.69	14.19	1.05	1.49	74
53	0.50	0.50	0.25	0.75	64.98	41.70	17.23	1.04	1.58	73
54	0.50	0.25	0.50	0.50	62.81	40.10	16.22	1.09	1.66	61
55	1.00	0.25	0.50	0.75	42.60	24.75	5.88	1.62	5.34	59

6 Infrared Fibres Tests

6.1 Introduction

The recent availability of infrared spectrographs with long slit capabilities and two dimensional detectors has opened the possibility of extending multifibre techniques to infrared wavelengths. Other uses of fibres in the infrared include image slicing and multiobject photometry (Parry *et al.* 1988). The latter might be more useful in the IR than in the optical because there is presently no large area detector in the IR equivalent to the photographic plate. The fibres can be coupled to spectrographs which for reasons of weight or stability might not be mounted on the telescope.

For any of the emerging astronomical applications the first step is to evaluate in the laboratory the properties of commercially available IR fibres. The important quantities are the transmission losses as a function of wavelength, focal ratio degradation and mechanical properties such as robustness. As discussed in chapter 4, the complex evaluation techniques in the visible are still in a developing process. Nevertheless, the development work in the visible has produced alternative techniques some of which are also suitable for fibres that transmit in the infrared region.

Virtually all optical astronomical applications make use of step index, multimode fused silica fibres, in which the core and cladding glasses are composed of vitreous silica (SiO_2) often doped with a small amount of germanium, boron or phosphorus compounds to produce the appropriate refractive index difference. Silica optical fibres are limited in the wavelength they can transmit to approximately 2μm and therefore infrared fibre optics that transmit beyond this, from 2 to 14μm require entirely different materials for their fabrication. The fundamental principles that describe the operation of silica optical fibres in terms of attenuation and propagation are not changed when considering IR optical fibres.

The optical energy of any electromagnetic radiation traversing a fibre suffers a reduction in intensity because some of it is absorbed by the material and some is scattered. These two sources of attenuation are the result of a variety of intrinsic and extrinsic factors. Extrinsic factors include absorption due to impurities and contaminants in the material such as hydroxyl (OH) groups and water, improper processing or fabrication such as non-uniformities in fibre radius or cladding thickness with length, core/cladding interface defects and localized deviations from the desired refractive index profile. Intrinsic losses are inherent in the material and hence unavoidable.

As discussed in chapter 2 (§2.4), the intrinsic attenuation spectrum is the result of three independent loss mechanisms in the material: ultraviolet or electronic absorption, Rayleigh scattering and absorption at the infrared vibrational edge. The exponential decay of electronic absorption intensity with wavelength makes it a negligible contribution factor to the overall attenuation beyond about 1μm. The scattering of light takes place because a glass is not perfectly uniform *i.e.* there exist small localized fluctuations in the refractive index of the material caused by variations in density or composition. This small scale granularity results in Rayleigh scattering of light and its intensity varies as λ^{-4} . At long wavelengths the transparency of an optical material is limited by the existence of an

infrared vibrational edge. Photons whose frequency matches the fundamental vibrational frequency of the glass components are strongly absorbed. As a result of this process fused silica glass SiO_2 only transmit light to 2.5μm beyond which strong absorption sets in.

The ability to prepare very high purity silica fibres is the result of a fabrication process which, at present, is unique to glasses that contain oxides. Silica based fibres whose attenuation spectrum closely approximates the theoretical intrinsic curve have been prepared and they exhibit transmission as high as T=95% per km or T=99% per m at 1.5μm. Nevertheless, even these highly transparent fibres contain small extrinsic peaks caused by OH impurities —see for instance figure 4.6.

At infrared wavelengths beyond 1.5μm it is desirable to take advantage of reduced Rayleigh scattering and the decreased absorption due to electronic transitions. The materials known as fluoride glasses are a subset of a much larger family of vitreous halides. These materials which incorporate the halogen and fluorine in place of oxygen, are suitable for use in the infrared. Because they have lower energy vibrational modes they provide access to the optically interesting 1–5μm region, although the loss levels attained in the best fluoride fibres to date are still far above the intrinsic limit. Some of the extrinsic loss mechanisms are the result of light scattering and attenuation caused by impurities. While significant improvements have been made in the purity of glass melting chemicals, extrinsic or non-Rayleigh scattering continues to be a difficult problem (Drexhage, 1990). Nonetheless for short fibres ($\sim$ 1m) the transmission is better than 97% between 1 and 4μm.

Another large family of IR transparent glasses may be formed from metals such as arsenic, germanium and antimony combined with the heavier elements in the oxygen family which includes sulphur, selenium or tellurium. The vitreous materials derived from such compounds are commonly known as chalcogenide glasses. They provide access to

the window between 5 and 11μm. Among the most common extrinsic sources of loss in chalcogenide fibres are hydrogen and oxygen-related impurities. Their transmission is about T=75% for a 1m long fibre.

Figure 6.1 (a) shows the transmission characteristics of three types of 1m long fibres. The losses for a silica-based fibre as a function of wavelength are presented in solid circles. The curve was derived from data given by Polymicro Technologies (FW series) for a fibre with extremely low OH^- content. The transmission of a fluoride glass fibre is presented in solid squares and that corresponding to a chalcogenide glass fibre is shown in solid triangles. The last two curves were derived from the data of Infrared Fibre Systems Inc. Figure 6.1 (b) shows the atmospheric transmission at Manua Kea, Hawaii in the near-infrared. It can be seen that the J and H windows can be exploited with silica fibres but the astrophysically interesting K band is best tackled with zirconium fluoride fibres. Another difficult challenge in the K band is the rapid onset of the thermal background with increasing λ.

As a first approach to the study of IR fibres the focal ratio degradation of a silica fibre was measured in the optical and in the infrared regions of the spectrum. The high transmission characteristics of a silica fibre up to 2μm, combined with its mechanical properties makes it ideal for such tests. The experiments carried out and the results obtained are described in the following section.

6.2 FRD Experiments

The test fibre used in the laboratory experiments was a 2m long, 600μm core diameter all silica fibre manufactured by Polymicro Technologies (FWP600720820). This fibre has

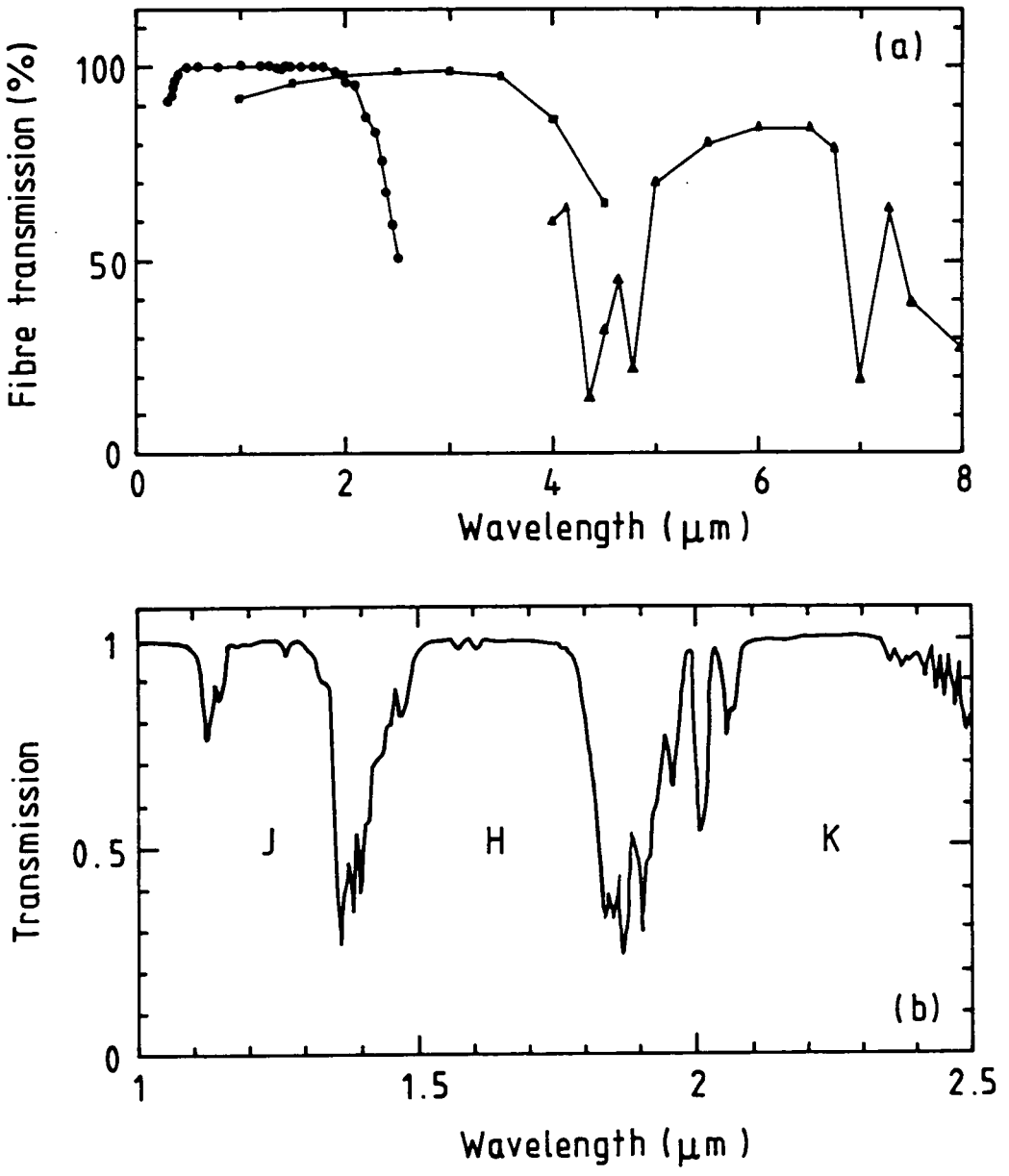

Figure 6.1. a) Transmission characteristics as a function of wavelength for 1m long fibres. The properties of an IR optimised silica fibre are shown in solid circles, the curve was derived using data from Polymicro Technologies (FW series). The transmission of a fluoride glass fibre is presented in solid squares and that corresponding to a chalcogenide glass fibre is shown in solid triangles. The last two curves were derived from data given by Infrared Fibre Systems Inc. b) The atmospheric transmission at Manua Kea, Hawaii in the near-infrared.

an ultra-low OH content specifically for IR applications. The diameter was chosen to match the f/35 image scale of the United Kingdom Infrared Telescope (UKIRT), which is equivalent to 625μm per arc sec. The fibre ends were cleaved and epoxied into brass ferrules for mounting and alignment. The ends were polished by hand with different grades of aluminum oxide papers (30, 9, 3, 1 & 0.3μm).

In order to provide a check on the accuracy of the measurements and a comparison with existing data on conventional fibres, the FRD properties of the fibre were determined at both optical and infrared wavelengths. The experimental setup in the optical is shown in figure 6.2. It consisted of a tungsten lamp from which light was transferred via a 1mm light guide to the input. An image of the light guide was projected onto the test fibre input end by means of two singlet 150F/50D lenses; an aperture stop located between them defined the input f-ratio. At the output end, the fibre image was projected onto a photodiode via a singlet 200F/50D and an achromat 300F/50D, with the output f-ratio defined by an iris. In this configuration the position of either iris along the optical axis is not critical as the light is collimated.

For the infrared measurements, an image of a pinhole illuminated by a stabilised blackbody source was projected onto the fibre input with a CaF_2 100F/25.4D lens. The input f-ratio was defined by an iris located as close as possible to the lens, and the input beam modulated by a stabilised chopper. At the output end a second iris fixed the emergent f-ratio and the image of the fibre end was projected with another 100F/25.4D lens onto the Fabry lens of the PbS detector, as shown in figure 6.3. The detector signal was measured using the lock-in amplifier which was phase-locked to a reference signal from the chopper. This configuration has the effect of subtracting the background radiation from the blackbody signal. A B2 filter was used to select a bandpass from 1.5–2.5μm.

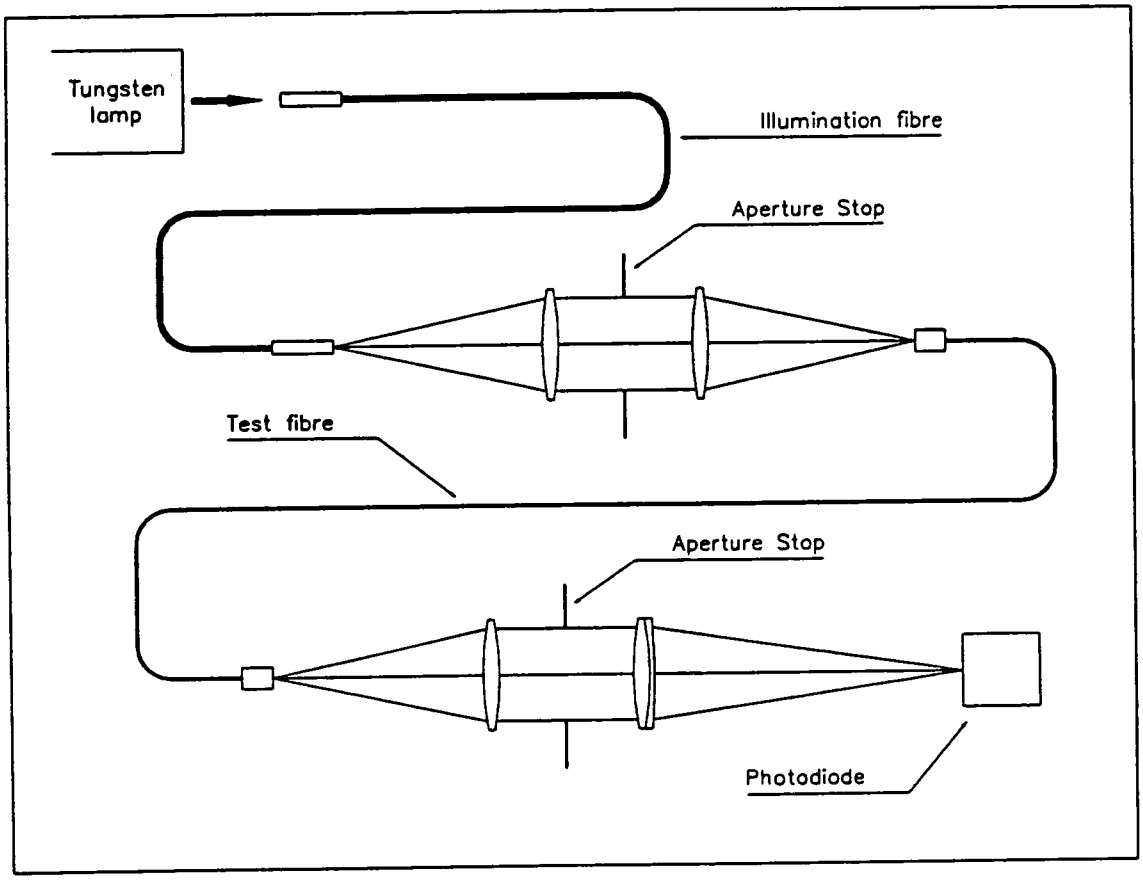

Figure 6.2. Schematic setup of the facility for the optical measurements. Light from a tungsten lamp is transferred to the input of the optical system via a 1mm core diameter fibre. An image of the light guide is projected onto the test fibre input end by two singlet lenses. The aperture stop defines the input f-ratio. At the output end the fibre image was projected onto a photodiode by means of a singlet and an achromat. The output f-ratio is defined by an iris.

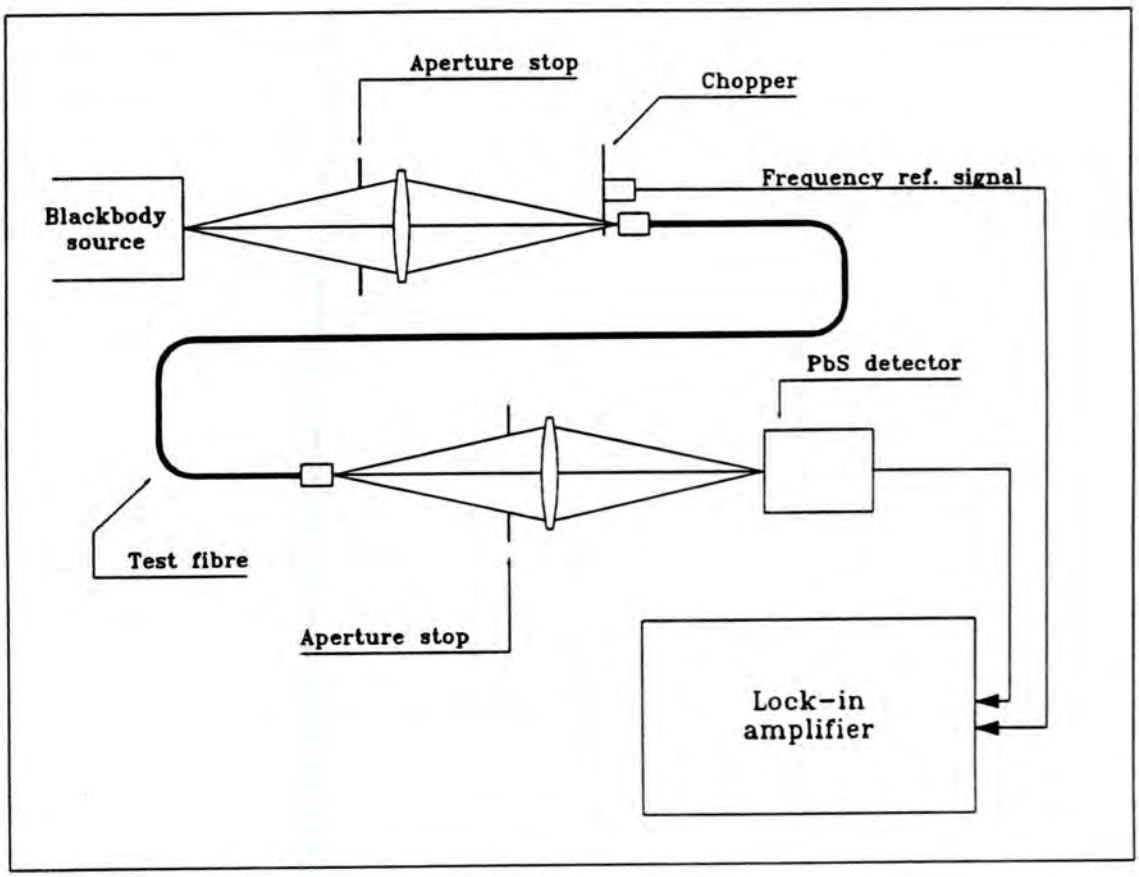

Figure 6.3. Schematic diagram for the infrared experiment. Light from a blackbody source is filtered and fed into the fibre input end via a CaF_2 lens. The input f-ratio is defined by an iris. At the output end a second iris defines the emergent f-ratio, the image of the fibre end is projected via another CaF_2 lens onto the Fabry lens of the PbS detector. To reduce the background the detector output and the chopper phase feed the lock-in amplifier. The lock-in then separates the signal from the unchopped background.

The temperature of the blackbody source was $T = 773°K$ so the peak of the intensity distribution was at $3.7\mu m$ ($\lambda T = 0.289cm\ K$). The measurements were made at the following input f-ratios: f/8, f/11, f/15 and f/35. The first three were chosen in order to compare the optical results with those previously reported for similar fibres while f/35 is characteristic of infrared chopping secondaries (*e.g.* UKIRT). For each input beam the throughput was measured for 10 different output apertures. The results were normalised to the throughput value obtained at an f/4 output f-ratio, therefore absorption or end losses are not included.

The throughput results as a function of the output f-ratio at optical and infrared wavelengths are shown in figures 6.4 and 6.5. In the former figure the results for an f/8 and an f/11 input f-ratio are presented while in the latter the corresponding results for an f/15 and an f/35 input beam are shown. The open circles correspond to the results in the optical and the solid circles to those obtained in the IR. The ideal case is plotted, in dotted lines, for comparison.

The FRD performance is very poor ($\sim 15\%$) at the slow f/35 input. This does not seem to be a property of the particular FWP fibre in use, since the optical performance at faster f-ratios is similar to other all-silica fibres used in existing instruments. As discussed in chapter 3, the FRD effect is more pronounced at slow input f-ratios and the results obtained here for an f/35 input beam confirm the severity of such effects at both optical and infrared wavelengths.

The results are generally somewhat better in the IR than in the optical. However it is difficult to state unequivocally that the FRD is less at infrared wavelengths. More work is required to study the FRD wavelength dependence. There are several sources of errors. The tungsten lamp stability (2.2%) was estimated from a previous experiment described in section 4.3, while the blackbody source stability was not monitored. The results at optical

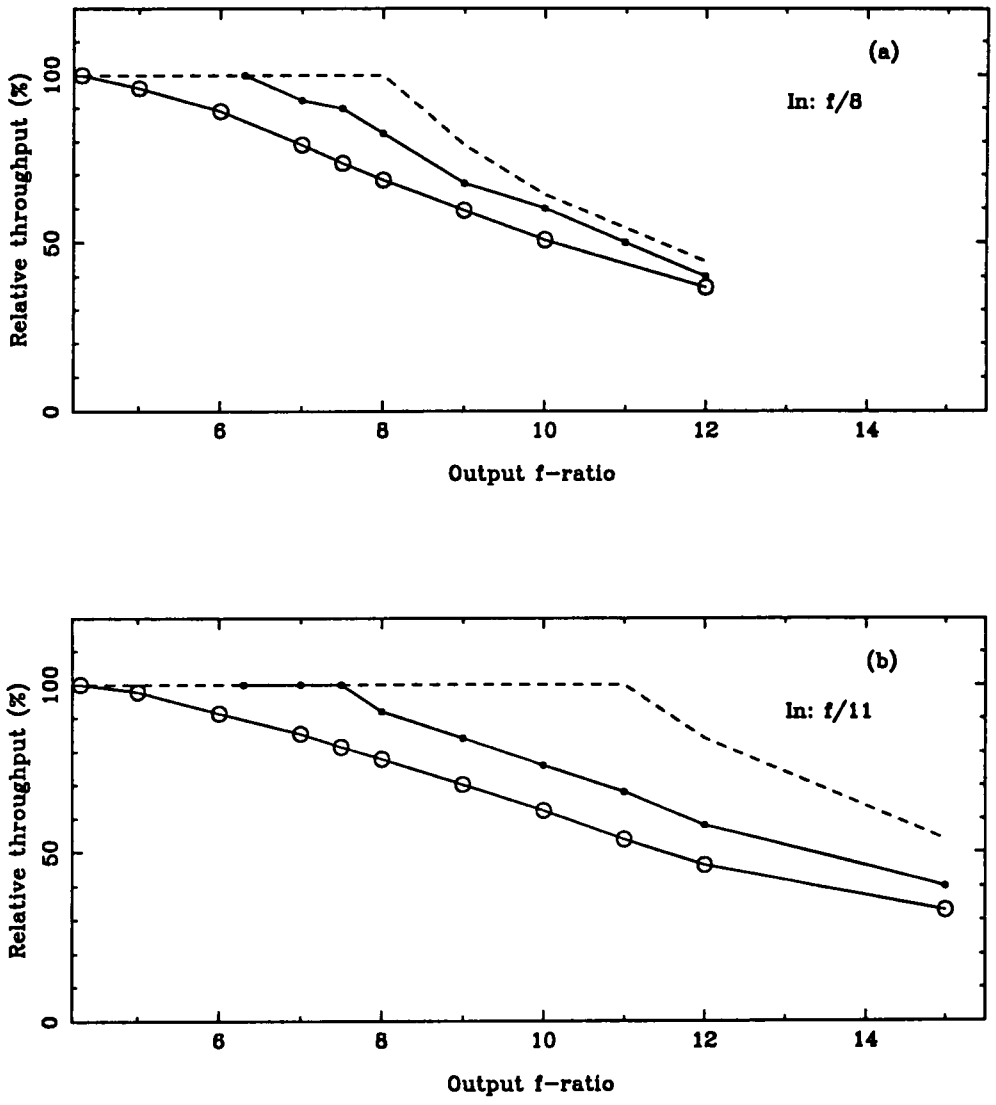

Figure 6.4. Relative throughput as a function of the output f-ratio for an all silica 600μm core diameter fibre. The solid circles are the results obtained at infrared wavelengths, the open circles are the results obtained at optical wavelengths and the dotted lines correspond to the ideal case. a) For an f/8 input beam. b) For an f/11 input beam.

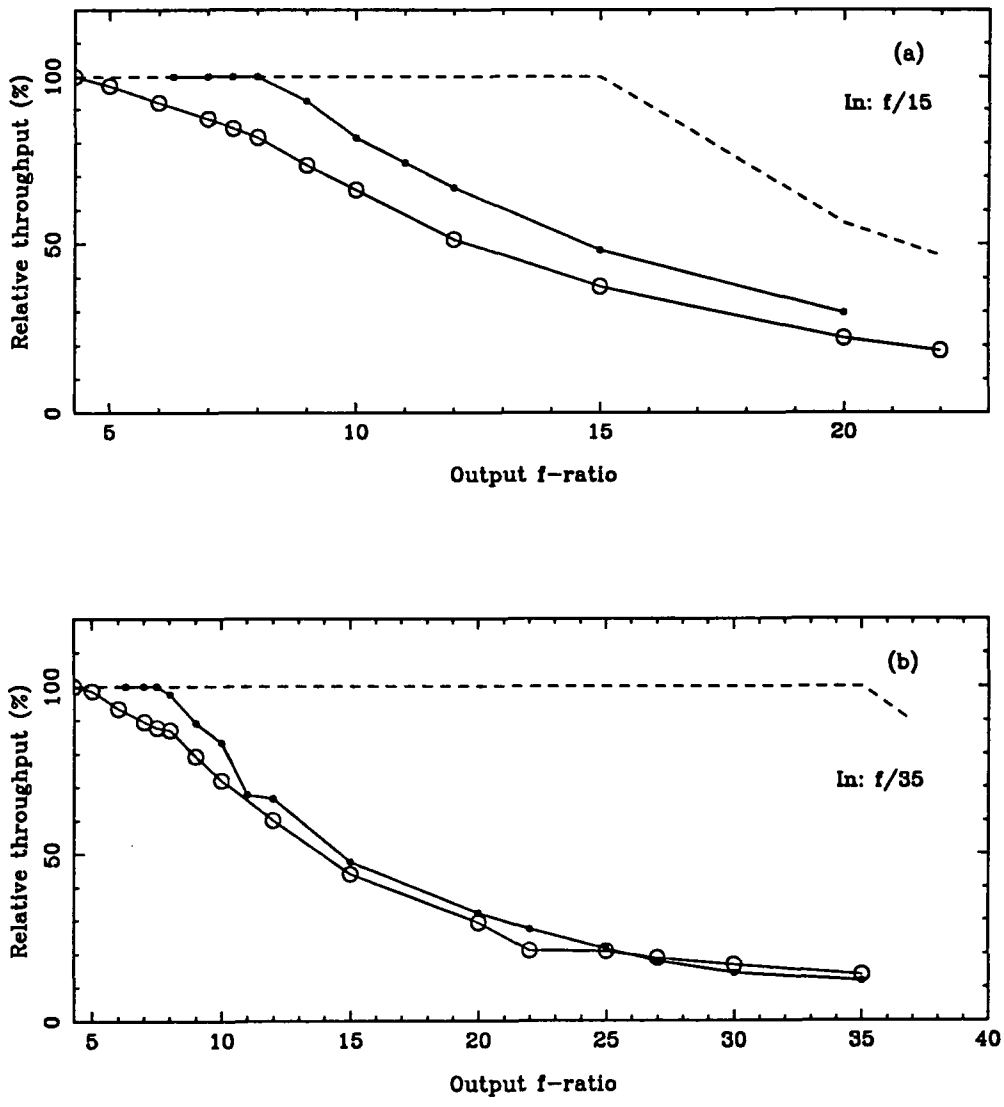

Figure 6.5. Relative throughput as a function of the output f-ratio for an all silica 600μm core diameter fibre. The solid circles are the results obtained at infrared wavelengths, the open circles are the results obtained at optical wavelengths and the dotted lines correspond to the ideal case. a) For an f/15 input beam. b) For an f/35 input beam.

wavelengths were obtained without any filter while in the IR experiments a bandpass was selected. The clear aperture of the CaF_2 lens available for this experiment was only 25mm, which clearly reduced the accuracy when trying to define a range of apertures from f/8 to f/35.

The results obtained in the visible for an f/11 input beam are consistent, within the experimental errors, with those obtained for the same fibre via the image experiment, described in chapter 4 (§4.2). For comparison purposes in figure 6.6 the FRD curves obtained via the three methods are presented. The solid circles are the results obtained in the IR with the setup shown in figure 6.3. The other two curves are the results obtained in the visible: the open circles are those obtained with the setup presented in figure 6.2 and the dashed line corresponds to those obtained via the image experiment shown in figure 4.1.

The results in the optical are therefore, similar to those previously reported but in the infrared there are not yet any results reported in the literature. Because there are no other results it is crucial to find a reliable and efficient fibre evaluation technique in order to be able to investigate the properties and performance of different types of fibres - particularly since there are many parameters involved in the measurements. For example, the total throughput measurement is sensitive to the finishing of the fibre ends and to both input and output alignment errors. Such precise alignment is difficult to achieve in the visible and can be expected to be even more difficult in the IR and one cannot confidently rule out the possibility of systematic errors in the results. Moreover for very slow input beams such as f/35, small misalignments lead to large errors in the throughput determination.

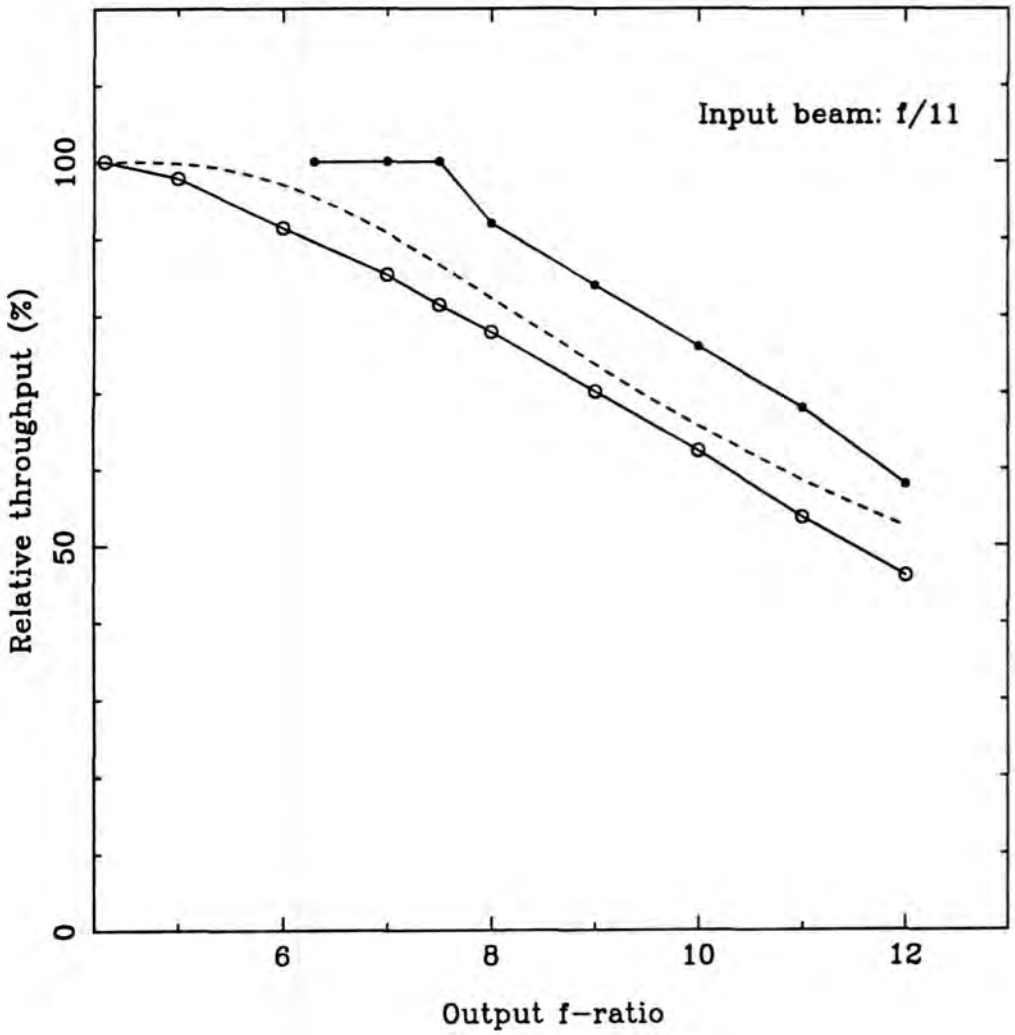

Figure 6.6. FRD curves for an all silica fibre 600μm core diameter for an f/11 input beam. The results obtained in the IR are shown in solid circles. Those obtained in the visible with the experimental setup presented in figure 6.2 are shown in open circles while the dashed curve corresponds to the results obtained via the image experiment with the setup shown in figure 4.1 also in the visible.

6.3 Future developments

The first step in a feasibility study of IR fibres should be the development of a reliable and efficient fibre evaluation method. This will allow the study of IR fibre properties relevant to astronomical applications such as FRD in a systematic way. In chapter 4 (§4.5) a new technique for determining the focal ratio degradation performance of optical fibres was described in which collimated light is launched into the fibre at various input angles and the projected ring of light at the output observed. From the width of the ring the output beam for any input beam can be accurately modelled.

In the optical a laser is used to provide the collimated input beam and a CCD TV camera can be used to examine the output rings. Imaging detectors —and to some extent lasers— are not so readily obtainable in the IR and it may be necessary to scan the output beam with a single element detector on a rotary table.

The FRD properties of optical fibres are strongly dependent on input f-ratio and the results shown in figure 6.4 and 6.5 clearly show this tendency. For an f/8 input beam the amount of light within an f/8 output beam is about 80% while for an f/35 input beam the corresponding quantity is only 15%. The poor throughput at f/35 could be significantly improved by using microlenses to convert the input (and output) beam. This also has the advantage of allowing the use of smaller fibre core sizes. Because IR telescope foci are generally very slow to reduce emissivity the use of microlenses is particularly attractive in the IR.

The way in which microlenses will improve the fibre FRD performance is illustrated in figure 4.17 (a). The plot shows the FWHM of the output profile as a function of the angle of incidence, with respect to the fibre axis for a collimated input beam. The FWHM is a measure of the degree of beamspreading and a good fibre will give a very narrow width. According to the model described in chapter 3 (§3.7), the width profile is

approximately constant for any angle of incidence. Assuming that the collimated input beam is an extreme ray of a conical input beam we can directly relate the angle of incidence and the FWHM to the input and output f-ratios according to the relationships given by equations 4.2 and 4.3.

At the fibre input end a microlens will change the f-ratio of the input beam to a faster f-ratio, *i.e.* it will increase the angle of incidence. However the beamspreading will be unchanged, therefore at the output end the size of the beamspreading in terms of the output f-ratio (*i.e.* the FRD) is less. Another microlens at the output end can be used to increase the f-ratio —but the FRD will be unchanged— without altering the FRD which will remain lower than for a fibre without a microlens at the input. Of course, there will be some losses due to reflections and coupling of the microlenses to the fibre ends but anti-reflection coatings can be used to reduce the additional surface losses incurred to a few percent. The losses due to the lens coupling can be minimised by using an appropriate index matching gel between the microlens and the fibre end. Suitable materials for microlenses are Schott LaSF9 and sapphire.

Another parameter that has to be considered is the core diameter size. Large-core fibres are most suitable for multiobject spectroscopy applications in terms of matching the f/35 image scale. Alternatively smaller core diameter fibres of about 200μm are suitable for image-slicer applications and multi-object spectroscopy applications when using microlenses. In the case of the 600μm core diameter silica fibre used in the experiments described in the last section, the Polymide buffer makes it very rigid and as a result there is a lower limit of about 20cm to the bending radius of curvature before stress-induced fractures appear.

Spectroscopy with fibres longward of 2.5μm will require cold fibres to reduce the emission from fibres themselves. Therefore it is important to investigate how the prop-

erties of IR fibres change as they are cooled to extremely low temperatures. As shown in figure 6.1 the all-silica fibres absorb strongly beyond 2.2μm. For fibre spectroscopy throughout the K band, zirconium fluoride fibres seem to be the most promising. The infrared measurements reported here are confined to a single broadband 1.5–2.5μm window. To improve the wavelength resolution of the investigations broadband JHK filters or preferably a monochromator should be used. Of the above aspects of the IR fibres that should be investigated, microlenses are the most important.

This chapter is only an introduction to the study of infrared fibres and the results obtained are very encouraging for the future. Clearly their use in IR astronomical spectroscopy presents a considerable challenge and much work has still to be done to study and evaluate the relevant parameters.

ACKNOWLEDGMENTS

I would like to thank my supervisor Ian Parry, for his support and guidance. Many thanks to all the people in the Physics Department, in particular to Mike Breare, Ray Sharples, Jeremy Allington-Smith and Alan Lotts. I would also like to thank John Webster and Pauline Russell for their technical help. Thanks to my fellow students and friends, specially to Alfonso, Nial, Ian, Mike, Gordon and Michael. Finally, I would like to acknowledge the CONACYT and UNAM in Mexico and the University of Durham for the financial support I received during this work.

BIBLIOGRAPHY

Allan, W.B., 1973. *Fibre Optics. Theory and Practice*, Plenum Press.

Angel, J.R.P., Adams, M.T., Boroson, T.A., & Moore, R.L., 1977. *Astrophys. J.*, **218**, 776.

Barden, S.C., 1987. *KPNO Fiber Optics Lab. Report No.1*, Tucson, Arizona.

Barden, S.C. & Massey, P., 1988. in *Fibre Optics in Astronomy, A.S.P. Conference Series, Vol. 3*, p. 140, Ed. Barden, S.C.

Barden, S.C., Armandroff, T., Massey, P., Groves, L., Rudeen, A.C., Vaughnn, D. & Muller, G., 1992a. in *Fibre Optics in Astronomy II*, Ed. Gray, P.M. *in press*.

Barden, S.C., Elston, R., Armandroff, T. & Pryor, C.P., 1992b. in *Fibre Optics in Astronomy II*, Ed. Gray, P.M. *in press*.

Brodie, J.P., Bixler, J.V., Craig, W.W., Donelly, R.H., Hailey Ch.J. & Seppala, L.G., 1990. *Proc. SPIE*, **1235**, 772.

Carter, D., 1988. *Proposal for new instrumentation for the Issac Newton Group WHT. WYFFOS a dedicated fibre feed spectrograph*, Royal Greenwich Observatory.

Chamberlain, J.W., 1961. *Physics of the Aurora and Airglow*, Academic Press.

Drexhage, M.G., 1990. in *Fluoride Glass Optical Fibres*, p. 1, Ed. France, P.W., Blackie.

Ellis, R.S. & Parry, I.R., 1988. in *Instrumentation for Ground based Astronomy: Present and Future*, p. 192, Ed. Robinson, L.B., Springer-Verlag.

Gambling, W.A., Payne, D.N. & Matsumura, H., 1975. *Appl. Opt.*, **14**, 1538.

Gloge, D., 1972. *Bell Syst. Tech. J*, **51**, 1767.

Gray, P.M., 1983. *Proc. SPIE*, **445**, 57.

Gray, P.M., 1988. in *Fibre Optics in Astronomy, A.S.P. Conference Series, Vol. 3, p. 285*, Ed. Barden, S.C.

Heacox, W.D., 1986. *Astron. J.*, **92**, 219.

Hill, J.M., Angel, J.R.P., Scott, J.S., Lindey, D., & Hintzen, P., 1980. *Astrophys. J.Letters*, **242**, L69.

Hill, J.M. & Lesser, M.P., 1986. *Proc. SPIE*, **627**, 303.

Keck, D.B., 1981. in *Fundamentals of Optical Fiber Communications*, p .1, Ed. Barnoski, M.K., Academic Press.

Lesser, M.P. & Hill, J.M. , 1987. in *Instrumentation for Ground based Astronomy: Present and Future*, p. 233, Ed. Robinson, L.B., Springer-Verlag.

Lewis, I.J., 1991. *Ph.D. thesis*, University of Durham.

Love, J.D. & Winkler, C., 1978. *Electron. Lett.*, **14**, 32.

Lund, G. & Enard, D., 1984. *Proc. SPIE*, **445**, 65.

Midwinter, J.E., 1979. in *Optical Fibers for Transmission*, John Wiley & Sons.

Parry, I.R., 1986. *Ph.D. Thesis*, University of Durham.

Parry, I.R. & Gray, P.M., 1986. *Proc. SPIE* , **627**, 118.

Parry, I.R. & Sharples, R.M., 1988. in *Fibre Optics in Astronomy, A.S.P. Conference Series, Vol. 3*, p. 93, Ed. Barden, S.C..

Parry, I.R., Ellis, R.S., Breare, J.M. & Lewis, I.J., 1988. in *Letter of intent to participate in the UKIRT Instrumentation Programme*, Durham University.

Parry, I.R. & Lewis, I.J., 1990. *Proc. SPIE*, **1235**, 681.

Parry, I.R. & Carrasco, B.E., 1990. *Proc. SPIE*, **1235**, 702.

Parry, I.R., 1992. in *Proc. ESO Conference on Progress in Telescope and Instrumentation Technologies*, Garching, Germany. *in press*.

Powell, J.R. , 1983. *Proceedings SPIE*, **445**, 77.

Ramsey, L.W., 1988. in *Fibre Optics in Astronomy, A.S.P. Conference Series, Vol. 3, p. 28*, Ed. Barden, S.C.

Snyder, A.W. & Mitchell, D.J., 1974. *Optik*, **40**, 438.

Taylor, K., 1988. *The Wide-Field Prime-Focus Adaption to the AAT. Scientific case and functional specifications*, Anglo-Australian Observatory.

Taylor, K., 1989. *2dF Design Report*, Anglo-Australian Observatory .

Watson, F. G., 1986. *Proc. SPIE*, **627**, 787.

Watson, F. G., 1988. in *Fibre Optics in Astronomy, A.S.P. Conference Series, Vol. 3*, p. 125, Ed. Barden, S.C.

Watson, F. G., Oates, A.P. & Gray, P.M., 1990. *Proc. SPIE*, **1235**, 736.

White, S.D.M., 1987. in *Instrumentation for Cosmology*, p. 41, Ed. Davies R.L., Tucson, Arizona.

Wilson, J. & Hawkes, J.F.B., 1983. *Optoelectronics: An Introduction*, Prentice-Hall International Series.

Wyse, R.F.G. & Gilmore, G., 1992. *Mon. Not. R. astr. Soc.*, **257**, 1.